

Co-laminar flow cells for electrochemical energy conversion

by

Marc-Antoni Goulet

M.Sc. (Physics), McMaster University, 2008
B.Sc., McGill University, 2006

Dissertation Submitted in Partial Fulfillment of the
Requirements for the Degree of
Doctor of Philosophy

in the

School of Engineering Science
Faculty of Applied Sciences

© Marc-Antoni Goulet 2016

SIMON FRASER UNIVERSITY

Summer 2016

All rights reserved.

However, in accordance with the *Copyright Act of Canada*, this work may be reproduced, without authorization, under the conditions for Fair Dealing. Therefore, limited reproduction of this work for the purposes of private study, research, education, satire, parody, criticism, review and news reporting is likely to be in accordance with the law, particularly if cited appropriately.

Approval

Name: Marc-Antoni Goulet
Degree: Doctor of Philosophy
Title: *Co-laminar flow cells for electrochemical energy conversion*
Examining Committee: **Chair:** Amr Marzouk
Lecturer

Erik Kjeang

Senior Supervisor
Associate Professor

Michael Eikerling

Supervisor
Professor

Gary Wang

Supervisor
Professor

Edward Park

Internal Examiner
Professor

Matthew Mench

External Examiner
Professor
Department of Mechanical, Aerospace
and Biomedical Engineering
University of Tennessee, Knoxville

Date Defended/Approved: May 2nd, 2016

Abstract

A recently developed class of electrochemical cell based on co-laminar flow of reactants through porous electrodes is investigated. New architectures are designed and assessed for fuel recirculation and rechargeable battery operation. Extensive characterization of cells is performed to determine most sources of voltage loss during operation. To this end, a specialized flow cell technique is developed to mitigate mass transport limitations and measure kinetic rates of reaction on flow-through porous electrodes. This technique is used in conjunction with cyclic voltammetry and electrochemical impedance spectroscopy to evaluate different treatments for enhancing the rates of vanadium redox reactions on carbon paper electrodes. It is determined that surface area enhancements are the most effective way for increasing redox reaction rates and thus a novel *in situ* flowing deposition method is conceived to achieve this objective at minimal cost. It is demonstrated that flowing deposition of carbon nanotubes can increase the electrochemical surface area of carbon paper by over an order of magnitude. It is also demonstrated that flowing deposition can be achieved dynamically during cell operation, leading to considerably improved kinetics and mass transport properties. To take full advantage of this deposition method, the total ohmic resistance of the cell is considerably reduced through design optimization with reduced channel width, integration of current collectors and reduction of reactant concentration. With electrodes enhanced by dynamic flowing deposition the cell presented in this study demonstrates nearly a fourfold improvement in power density over the baseline design. Producing more than twice the power density of the leading co-laminar flow cell without the use of catalysts or elevated temperatures and pressures, this cell provides a low-cost standard for further research into system scale-up and implementation of co-laminar flow cell technology. More generally, the experimental technique and deposition method developed in this work are expected to find broader use in other fields of electrochemical energy conversion.

Keywords: fuel cell; flow battery; laminar flow; microfluidic; flow-through porous electrodes; vanadium

Dedication

I would like to dedicate this thesis to all the natural wonders which have been sacrificed for the sake of human endeavors such as this. It is hoped that the minor results contained within will eventually help to alleviate our collective environmental burden. Et ma mère. Merci maman.

Acknowledgements

First and foremost, I would like to thank my supervisor Erik Kjeang for giving me this opportunity and helping me along the way. His gentle supervision and unwavering faith in my abilities allowed me the necessary freedom to explore the new ideas that have been essential to the success of this project. On a more personal level, I would like to thank him for setting such a good example of dedication and persistence.

I would also like to express my sincere gratitude to my co-supervisor Michael Eikerling who took the time to see me and patiently answer my infinite questions. Without his reliable intellectual support, my research could easily have become mired in endless confusion and pointless digressions. I would similarly like to acknowledge Gary Wang for his sympathetic ear and judicious advice. In addition, I would like to express my appreciation to Prof. Em. Maria Skyllas-Kazacos for her general kindness, and for sharing some of her extensive experience with me during many pleasant discussions throughout my internship at UNSW. In relation to this, I would like to acknowledge the sponsorship provided by the Australia Endeavour program which made it possible for me to broaden my experience and the perspective of my research. Similarly, I would like to acknowledge the Natural Sciences and Engineering Research Council of Canada (NSERC) for their generous support during my degree.

I'd also like to thank my predecessor Jin who kindly got me started on this project and helped me to avoid unnecessary pitfalls. Of course this project would never have been completed without the hard work and assistance of all the co-op students passing through the lab in the past four years, namely: Jeffrey To, Chris de Torres, Stephen Rayner, Spencer Arbour, Aronne Habisch and Will Kim. Being able to share the frustrations of experimental work with them made it all the more enjoyable. Likewise, I am also very grateful to my graduate colleagues at SFU and friends in FCRel, with a special mention to Omar in particular, for all the pleasant conversations and good times. I wish there had been more.

Last but not least, I'd like to acknowledge all the family and friends I was unable to spend quality time with due to this work. I look forward to seeing you all again.

Table of Contents

Approval.....	ii
Abstract.....	iii
Dedication.....	iv
Acknowledgements.....	v
Table of Contents.....	vi
List of Tables.....	viii
List of Figures.....	ix
List of Acronyms.....	x
 Chapter 1. Introduction	 1
1.1. Background	1
1.2. Review of co-laminar flow cells.....	3
1.3. Research perspectives	8
1.4. Motivation and objective	10
 Chapter 2. Theory	 12
2.1. Electrochemical cells	12
2.1.1. Kinetics.....	15
2.1.2. Ohmic resistance.....	17
2.1.3. Mass transport.....	18
2.1.4. Reactant crossover.....	19
2.2. Co-laminar flow cells	20
 Chapter 3. Summary of contributions	 23
3.1. Microfluidic redox battery.....	23
3.2. Reactant recirculation in electrochemical co-laminar flow cells.....	25
3.3. Direct measurement of electrochemical reaction kinetics in flow-through porous electrodes	27
3.4. The importance of wetting in carbon paper electrodes for vanadium redox reactions.....	29
3.5. <i>In situ</i> enhancement of flow-through porous electrodes with carbon nanotubes via flowing deposition	31
3.6. Approaching the power density limits of aqueous electrochemical flow cells	34
 Chapter 4. Conclusions.....	 37
4.1. Present work	37
4.2. Future work	40
4.3. Technological outlook.....	41
 References	 42
Appendix A. Microfluidic redox battery	58

Appendix B.	Reactant recirculation in electrochemical co-laminar flow cells	63
Appendix C.	Direct measurement of electrochemical reaction kinetics in flow-through porous electrodes.....	72
Appendix D.	The importance of wetting in carbon paper electrodes for vanadium redox reactions.....	77
Appendix E.	In situ enhancement of flow-through porous electrodes with carbon nanotubes via flowing deposition	87
Appendix F.	Approaching the power density limits of aqueous electrochemical flow cells	97

List of Tables

Table 1. Major co-laminar flow cell performance developments	7
--	---

List of Figures

Figure 1. Major developments in early CLFC research: a) on-chip fabrication with flow over electrodes, b) multilayer fabrication with flow-by electrodes, c) air-breathing electrodes and d) flow through porous electrodes [39].	5
Figure 2. Schematic of all-vanadium redox flow battery where solid arrows indicate charging, and dashed arrows indicate discharging operation [160].	13
Figure 3. Typical electrochemical cell polarization curve demonstrating various sources of voltage loss: kinetic (I), ohmic (II), concentration (III), crossover (IV) and thermodynamic (V). Figure taken from Mench [14].	15
Figure 4. Schematic of CLFC operation.....	22
Figure 5. Novel dual-pass architecture [39].	24

List of Acronyms

CLFC	Co-laminar Flow Cell
CNT	Carbon Nanotube
CV	Cyclic Voltammogram
DMFC	Direct Methanol Fuel Cell
EIS	Electrochemical Impedance Spectroscopy
ESA	Electrochemical Surface Area
FTPE	Flow-through Porous Electrode
GDL	Gas Diffusion Layer
LFFC	Laminar Flow Fuel Cell
MEA	Membrane Electrode Assembly
MFC	Microfluidic Fuel Cell
MRB	Microfluidic Redox Battery
OCP	Open Circuit Potential
PEM	Polymer Electrolyte Membrane
PDMS	Poly(dimethylsiloxane)
RFB	Redox Flow Battery
VRB	Vanadium Redox Battery

Chapter 1.

Introduction

1.1. Background

On several scales, energy is one of the most critical and limiting factors behind human economic and population growth. On a global scale, the transition towards renewable energy systems cannot be achieved without energy storage solutions which can adequately address fluctuations in energy demand [1]. Whether for backup power, load-leveling, peak-shaving, some form of energy storage is required to address the intermittent nature of both wind and solar energy production [2]. Although there are several energy storage options available today, each of these options has advantages and drawbacks. Among these, subterranean compressed air and pumped hydro currently have the lowest capital cost per kWh and are the most attractive options for MW and GW scale energy storage due to their durability and safety, however both of these options are constrained to locations with suitable geographical features or topography [3], [4]. For utility-scale storage on the order of kW to MW where this geography is not available, storage in the form of electrochemical reactants becomes an attractive option due to its versatility and scalability [5]. In the case of thermodynamically open cells like fuel cells and flow batteries, the reactants are stored separately and pumped into the electrochemical cell. This decoupling of power and energy provides a certain flexibility for cost-effective application matching [1]. Several pilot projects have been demonstrated for vanadium redox batteries (VRB) in particular and commercialization of this technology is currently expanding [2], [3]. Moving further down the kW scale to household level utility or transportation applications such as electric cars, conventional closed cell batteries, such as lithium ion, become a competitive option for their higher specific energy and energy density [6]. For the same reasons, the lower power (< 100 W) market which is driven by portable consumer electronics, is currently

dominated by closed cell lithium ion batteries in particular [7]. As these batteries reach their limits and fail to keep up with the energy requirements of modern electronics, micro fuel cells with passively pumped higher energy density liquid reactants such as methanol have been suggested as a potential replacement [8].

Regardless of the technology, all electrochemical cells must maintain an ionically conductive path between electrodes for the circulation of current [9]. Most cells achieve this through the use of porous separators or solid state ionomer membranes. For example, polymer electrolyte membranes (PEM) are designed to allow hydrogen ions to pass while preventing the crossover of reactant gases in the case of low temperature hydrogen fuel cells and dissolved vanadium species in the case of vanadium redox batteries [10]. Continued development of these ionomer membranes has led to significant reductions in thickness, with 25-50 μm being a typical thickness used in current hydrogen fuel cells [11] and 125 μm in vanadium redox batteries [12]. Although this trend has contributed to significant performance gains due to reduced ionic resistance, it has also engendered certain technical challenges. In hydrogen fuel cells, thinner membranes tend to degrade and rupture more quickly leading to cell failure [13]. In the case of direct methanol fuel cells (DMFC), typical membranes still allow considerable crossover of methanol fuel due to diffusion and electro-osmotic drag [14]. Similarly, it has also been observed that rates of crossover will differ between vanadium redox species leading to an imbalance in the concentration of reactants and an associated capacity loss in the battery [15]. In addition to durability and crossover issues, expensive polymer electrolyte membranes increase the cost of electrochemical cells, particularly for alkaline fuel cells which require more expensive hydroxide-permeable anion exchange membranes [16]. Although less expensive hydrocarbon based membranes exist, these tend to have lower ionic conductivity [17]. Another added challenge inherent to membrane electrode assembly (MEA) design is the integration of reactant manifolds and planar stack components into miniaturized devices [18].

For all of the above reasons, many researchers have sought to circumvent the use of physical membranes or separators entirely. One such strategy is the use of selective catalysts at each electrode which enables the mixing of reactants without the typical performance loss [19]. Unfortunately, few examples of such a strategy have

garnered much success, though this idea has recently seen a resurgence in biofuel cells due to the highly selective nature of enzymes [20]–[27]. Rather than a solid physical barrier, the use of a flowing liquid electrolyte has also been used to keep gaseous hydrogen and oxygen reactants separate in early alkaline fuel cells used for the NASA space program [28]. With the advent of inexpensive microfabrication techniques such as soft lithography and 3D printing the field of microfluidics has become more accessible to the academic community, leading to more recent attempts to utilize flowing electrolytes [29]–[32]. At the micro scale, fluid dynamics are typically characterized by smooth laminar flow free of chaotic turbulence which permits two streams to flow side by side with mixing occurring exclusively by cross-stream diffusion. Several studies have exploited this phenomenon for DNA analysis [33], molecular positioning [34], microfluidic switches [35], and a wide range of other applications [36]. Rather than a flowing blank electrolyte separating gaseous reactants, it was first demonstrated by Ferrigno *et al.* in 2002 that co-laminar flow of two liquid streams could be utilized to prevent crossover of electrochemical reactants [37].

1.2. Review of co-laminar flow cells

The first co-laminar flow cell (CLFC) published by Ferrigno *et al.* was a simple Y-junction microfluidic channel with two inlets and a single outlet fabricated by soft-lithography of poly(dimethylsiloxane) (PDMS). The planar 'flow-over' gold and graphite electrodes were deposited on the bottom of the centre channel and therefore perpendicular to the co-laminar flow interface. The reactants used were those used in the original vanadium redox flow battery, namely V^{2+} fuel and VO_2^+ oxidant dissolved in 25% H_2SO_4 . This original concept was conceived and coined as a single-pass laminar flow fuel cell (LFFC) for discharge of vanadium reactants [37]. Around the same time, another design by Choban *et al.* [38] relied upon a multi-layer sandwich construction similar to the MEA used in conventional fuel cells. In place of the membrane, the cell which was alternately named as a microfluidic fuel cell (MFC) used a spacing layer to provide a microfluidic channel between the 'flow-by' electrodes which were parallel to the co-laminar interface. In this case, the co-laminar flow concept was demonstrated with formic acid fuel and either potassium permanganate or dissolved oxygen as oxidant

streams. Since these early studies, CLFCs have evolved to include many other architectures, materials and functions, such as rechargeable flow battery operation; and have been reviewed extensively [39]–[44].

Some of the first studies on CLFCs sought to explore the unique advantages inherent to the ‘membraneless design’ by investigating reactant combinations that had previously been impractical with membrane based cells. Both Choban *et al.* and Cohen *et al.* demonstrated the use of acidic/alkaline mixed media operation to increase the open circuit potential (OCP) of a hydrogen/oxygen fuel cell [45], [46]. Similarly, both Hasegawa *et al.* and Chen *et al.* used this method to investigate the possibility of using hydrogen peroxide as both fuel in alkaline electrolyte and oxidant in acidic electrolyte [47], [48]. Although mixed media operation was demonstrated in all cases, the exothermic consumption of the electrolyte at the co-laminar interface decreased the overall benefit of the method. Meanwhile, other studies attempted to improve the performance of CLFCs with the help of refinements to the original designs. A computational study by Bazylak *et al.* suggested that tapering of the electrodes away from the co-laminar interface would prevent unnecessary crossover and mixed potentials from occurring [49]. Unfortunately no experimental studies have thus far made use of this design suggestion. To similarly address crossover limitations, Sun *et al.* introduced an additional blank electrolyte stream between the two reactant streams, leading to reduced crossover as revealed by improved open-circuit potential [50]. From a practical perspective however, this strategy is unlikely to be adopted due to the added complexity of pumping an additional electrolyte and the associated contamination of all unused inputs. Another ambitious study by Yoon *et al.* demonstrated the effect of periodically placed sequential outlets and inlets on the depletion boundary layer of CLFCs with planar electrodes. Necessitating a higher device footprint, these strategies will likely only be implemented for analytical purposes. A more useful strategy suggested in this study is the use of herringbone ridges to promote convective replenishment of reactants at each individual electrode [51].

Among the more innovative concepts to be put forth in the initial stages of CLFC research was the adaptation of air-breathing capability seen in conventional polymer electrolyte fuel cells [52] and metal-air batteries [53] by Jayashree *et al.* [54] in 2005.

Using the multi-layer device layout, it was demonstrated that a hydrophobic gas diffusion layer (GDL) could be used as a cathode and protected from fuel crossover by a blank stream of electrolyte [54]. The system still requires two separate liquid streams to be used and thus has no net energy density advantage; however the added functionality has led to other benefits. Notably, the possibility of using gaseous reactants, whether air, pure oxygen, or other reactants such as hydrogen, has led to significantly greater performance over the dissolved gas designs previously published by other researchers. The architecture of this device was later optimized to produce up to $55 \text{ mW} \cdot \text{cm}^{-2}$ with a pure oxygen gas stream at the cathode and formic acid at the anode. This first use of a porous carbon paper electrode may have influenced other researchers to move towards three dimensional electrodes with higher electrochemical surface area (ESA) [55]–[57].

Overall, the power density performance of CLFCs remained relatively low compared to membrane based designs until 2008 when Kjeang *et al.* demonstrated that the vanadium reactant streams coming from the inlets could be forced through porous electrodes and still maintain a co-laminar interface until reaching the outlet [58]. These flow-through porous electrodes (FTPE) minimized reactant depletion issues and maximized the fuel utilization, enabling the cell to produce up to $131 \text{ mW} \cdot \text{cm}^{-2}$ when normalized by the projected area or 403 mW cm^{-2} when normalized by the cross-sectional area of one electrode. Using the same lithographic process as the original Y-junction cell to form the microfluidic channels, the porous electrodes were simply placed in their respective grooves and lightly compressed by the glass capping layer to retain the same low profile ‘on-chip’ fabrication style. At the time, this was the first case of a CLFC reaching power densities similar to conventional electrochemical cells.

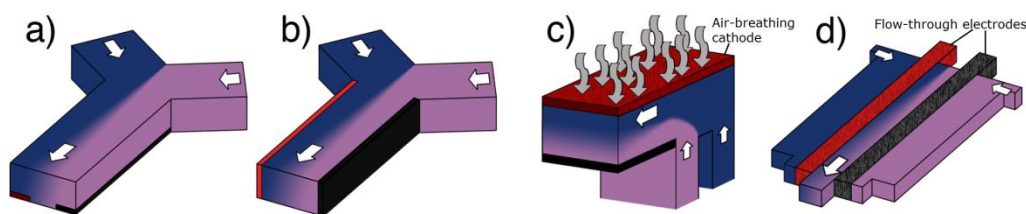


Figure 1. Major developments in early CLFC research: a) on-chip fabrication with flow over electrodes, b) multilayer fabrication with flow-by electrodes, c) air-breathing electrodes and d) flow through porous electrodes [39].

After the major developments represented in Fig. 1, CLFC research began to expand steadily, with the relative number of theoretical and computational studies increasing until 2012 [39]. Unfortunately, most of the computational studies published during this time failed to provide experimental validation for their recommendations [59]–[74]. In general, experimental efforts to improve the performance of individual co-laminar flow cells waned during this period, with researchers instead using the CLFC platform to focus on tangential goals such as fuel flexibility [75], the effect of gas bubbles [76], [77], and catalyst studies [78]–[81]. Other notable explorations that were made during this time include the investigations into microbial and enzymatic biofuel conversion by Li *et al.* [82] and Zebda *et al.* [83]–[85] respectively. Although these early biofuel studies generated only very low power output, they demonstrated that the original ‘on-chip’ co-laminar flow cell platform may be suitable as a biosensor. A few other ambitious studies were performed to attempt novel flow configurations such as radial [57], orthogonal [86], or counter flow [87]. In all cases however, the architectures resulted in only modest power densities and did not demonstrate any specific advantage over the original unidirectional parallel flow case. Another study by Hollinger *et al.* reintroduced the use of physical separators between reactants, in order to reduce diffusion of methanol across the co-laminar interface [88]. It is not clear whether the concept of co-laminar flow is compatible with the use of separators or other diffusion blocking features located at the interface, but this strategy has meanwhile been used by other researchers in the field [89]–[91].

Since the start of this research project in January 2012, more studies have been published which have significantly increased the performance of co-laminar flow cells [91]–[93]. The study by Da Mota *et al.* achieved $250 \text{ mW} \cdot \text{cm}^{-2}$ through the combined use of nanoporous separators and electrodes patterned with herringbone mixers [91]. My predecessor Jin Wook Lee also improved the original flow-through porous electrode design by Kjeang *et al.* through the use of gold current collectors. With a 30% reduction in ohmic resistance, the cell produced a cross-sectional power density of 620 mW cm^{-2} [92]. A year later in 2013, another study by our group, and the first study in this work, was published which demonstrated similar power density but also rechargeable battery operation with a new dual pass architecture [94]. Shortly thereafter Braff *et al.* released an innovative hydrogen bromine cell which exploits the fast reaction kinetics of both

reactants and the convenience of their common hydrobromic acid electrolyte to achieve a record setting maximum power density of $795 \text{ mW} \cdot \text{cm}^{-2}$ [93]. The data in Table 1 summarizes most of the important power density benchmarks set by CLFCs since their introduction until the present time.

Table 1. Major co-laminar flow cell performance developments

Author (Year)	Fuel	Oxidant	Peak Power (mW)	Peak Power Density (mW cm^{-2})	Volumetric Peak Power Density (mW cm^{-3})
Ferrigno (2002)	1M V^{2+}	1M VO_2^+	3	38	475
Choban (2005)	1M CH_3OH	Dissolved O_2	3	12	160
Kjeang (2008)	2M V^{2+}	2M VO_2^+	15	403	1344
Jayashree (2010)	1M HCOOH	Pure O_2	36	55	809
Lee (2012)	2M V^{2+}	2M VO_2^+	11	620	2067
Da Mota (2012)	0.15M NaBH_4	0.5M CAN	135	270	5190
Braff (2013)	Pure H_2	5M Br_2	199	795	6625

Meanwhile, flow-through porous electrodes have become more prevalent in both experimental [95]–[101] and computational studies [102]–[104], due to their higher surface area and better mass transport characteristics making them advantageous for achieving higher power densities [39]. In addition, a couple of new studies built upon the previous work by Salloum *et al.* [105] and Moore *et al.* [106], to assess the possibility for stacking of multiple cells [100], [107]. In all cases, stacks generally exhibited power output nearly proportional to the number of cells, with discrepancies likely due to the shunt current losses [99], [108]. More in depth experimental studies such as these focused on other aspects of CLFCs. The second study in this work characterized the crossover losses and reactant recirculation possibilities of both single and dual pass architectures [109]. Similarly, a study by Marschewski *et al.* provided a thorough analysis of microfluidic mixing demonstrating the utility of a raised neutral region in between turbulence promoting herringbone structures to preserve co-laminar flow [110]. Lastly, another major research area to have expanded in the past few years is the use of

CLFCs for enzymatic or microbial biofuel conversion which have generally improved upon the power density of earlier studies but remain in the $\mu\text{W}\cdot\text{cm}^{-2}$ regime [111]–[117].

1.3. Research perspectives

In the short time since their inception, research in co-laminar flow cells has branched into several directions. Although many variations have been attempted, it has been suggested in a recent review by our group that the two initially established fabrication styles are leading toward different research directions and potential applications, namely low profile ‘on chip’ fabrication for low power biomedical sensor applications and sandwich structure multilayer styles for higher power devices [39].

Typically the lithographic process is utilized for creating microfluidic channels with a low channel height which forces the reactants to flow closely over deposited electrodes. With the electrodes within the same layer as the microfluidic channels and manifolds, this strategy leads to low profile cells which can be easily integrated into ‘on-chip’ applications such as sensors, a feature which distinguishes them from conventional MEA based cells [118]. This has made this fabrication style particularly favoured by research groups investigating biofuels such as glucose for potential biological or point of care medical applications [82], [83], [85], [111], [113], [116], [119], [120]. In general, this single-layer device platform has spawned many derivative studies [48], [50], [55], [76], [77], [80]–[83], [85], [113], [119]–[123] due to its simplicity of construction and the possibility for direct visualization of the co-laminar interface quality and reactant conversion through the clear PDMS channel substrate. This unique feature has recently been utilized to visually track and quantify the effect of herringbone mixers on crossover of reactants via micro particle image velocimetry [110]. It has also been shown that parallel and series multiplexing of these cells within the same PDMS layer is possible but suffers from low overall device power density due to the added area required for separate manifolds [37], [105], [107]. As the power of the cell scales linearly with the area of the co-laminar interface, these low profile (low channel height) cells have also been restricted in their individual performance to low power operation (< 100 mW). If these challenges can be overcome it has been suggested that ‘on-chip’ power and

cooling of microprocessors may become an attractive option for this technology [124], [125].

Although multi-layer designs began with low profile channel height [38], [45], [46], [51], [79], [126]–[133], many of these cells now resemble the high aspect ratio of conventional MEA based cells [133]. The primary advantage behind this sandwich structure fabrication method is the use of standardized off the shelf planar components such as graphite and gaskets which are well known to researchers in the field of fuel cells and flow batteries and do not require any expensive lithography infrastructure. Although only one attempt has been published thus far by Moore *et al.* [106], these low cost cells also have greater potential to be efficiently stacked in the same manner as existing MEA technology. Moreover, with electrodes parallel to the co-laminar interface these cells can be more easily scaled for maximum power output such as the previous record holding cell by Braff *et al.* [93] at 199 mW, which is currently being investigated for commercialization. For these reasons, this cell fabrication style has been favoured by research groups already working in the field of electrochemical energy conversion.

Regardless of which style is used, CLFC fabrication methods typically relate to cost, device durability and system integration consideration, whereas cell performance is inextricably linked to device architecture and materials. Concerning these materials, it is interesting to note the sheer number of reactant combinations that have been attempted with CLFCs. Some of the liquid fuels used include dissolved hydrogen [45], methanol [46], [75], [78], [89], [126], [133], [134], formic acid [38], [54], [75], [79], [81], [123], [127], [129], [131], [135]–[139], hydrogen peroxide [48], [122], V^{2+} [37], [55], [56], [58], [87], [92], [94], [96], [105], [106], glucose [80], [83]–[85], [111], [112], [130], glycerol [128], acetate [114], sodium borohydride [75], [91], hydrazine and ethanol [75]. Moreover, it would seem that many CLFC studies focus on other aspects such as catalysis which are not necessarily related to the co-laminar technology [78]–[81], [128], [137], [139]. Both of these facts point to the accessibility of the technology as an inexpensive lab-scale analytical platform for evaluating electrochemical materials and processes. Lacking the membranes of conventional electrochemical cells, these simpler CLFCs have also been the subject of several numerical investigations [47], [49], [51], [59]–[74], [89], [102], [103], [132], [140]–[152], though few of the suggestions coming from these studies, such

as tapering of the centre channel, have been experimentally verified. Another unexpected but logical avenue for these simple and inexpensive devices is as educational materials for demonstrating microfluidic and electrochemical concepts, particularly for co-laminar flow cells with transparent 'on-chip' fabrication style and colourful reactants [153]. Overall, it is expected that CLFC technology will continue to diverge into other areas of electrochemistry indirectly related to energy conversion.

1.4. Motivation and objective

Although CLFC power density continues to increase and compares quite favourably with and even exceeds many existing fuel cells and flow batteries, it is not clear whether the technology will achieve commercial viability. As open cells depend on reactant flow, any commercial application involving CLFCs will inevitably require balance of plant items such as pumps and reactant storage. Even if future cells can eliminate such ancillary parts by relying on gravity induced flow, capillary action [118], [154], or even gaseous venting [155], [156]; the question of scale remains a significant barrier to commercialization as power sources. Since these cells are inherently limited in size by the co-laminar concept of reactant separation, it is crucial for these cells to be as effective as possible to achieve practical power outputs. As explained previously, fuel cells and flow batteries typically become cost-competitive with closed cell lithium-ion batteries above the kW scale which is unlikely to be achieved with CLFC technology. Realistically, co-laminar flow cell technology is more likely to become advantageous in niche applications where 'on-chip' integration, fuel flexibility, durable operation, or low cost disposable characteristics are essential. Whether the right application turns out to be power and cooling of microprocessors or glucose powered disposable medical devices, power density continues to be one of the most important metrics to maximize [125]. Doing so without compromising the low cost and durability benefits of the device is therefore the primary goal for this project. Consequently, maximizing the power density is likely to lead to other benefits such as increased energy efficiency and fuel utilization. Such improvements may eventually allow for additional functionality and extend the applicability of CLFC technology.

This research project began as an investigation to determine whether the existing baseline design for single pass discharge of vanadium redox reactants could be altered to act as a rechargeable flow battery. After the initial success of the novel dual-pass design developed in the first study and explained in chapter 3.1, a more in depth follow up study described in section 3.2, was performed to assess the limits of both the new and baseline design for fuel recirculation. The results from this study indicated that reactant crossover could not be entirely avoided and developing higher voltage efficiency and fuel utilization would be preferable to reduce the amount of recirculation required. The remainder of the project was therefore focused on enhancement and optimization of the baseline design first developed by Kjeang *et al.* [58], with the ultimate goal of designing the ideal CLFC architecture so that future researchers could move on towards device integration and scale-up of the technology. This was achieved by characterizing all sources of energy and power loss in the baseline cell and developing novel ways to mitigate and eliminate each of these losses. In line with this strategy, the third and fourth studies in this dissertation focus exclusively on characterizing the reaction kinetics of vanadium on flow-through porous electrodes, whereas the fifth study proposes an inexpensive way to enhance these reactions. The final extensive study includes both experimental and computational work to optimize the baseline architecture. With added electrode enhancement, this final design achieves the primary goal of maximizing the power density of a single co-laminar flow cell.

Chapter 2. Theory

2.1. Electrochemical cells

Electrochemistry is concerned with phenomena involving any type of conversion of chemical species with an accompanying electrical current, a process which typically occurs at the interface between an ionically conductive electrolyte phase and an electrically conductive phase. Electrochemical cells can be defined as a collection of these interfaces through which current can flow, either galvanically through spontaneous conversion of chemical reactants, or electrolytically through current supplied by an external power source [9]. Historically, the term fuel cell was applied to any galvanic electrochemical cells used for harvesting the electrical energy from the oxidation of fuels such as hydrogen or methanol [14]. Fuel cells, such as the alkaline electrolyte systems developed by NASA for long term space missions, have also been used for the reverse electrolytic process of regenerating the fuel and oxidant through the application of an external potential [157]. With reactants undergoing phase changes between liquid and gaseous states, such regenerative fuel cells typically suffer from low cycle efficiency due in part to the difficulty of optimizing the device structure for both directions of phase change [158]. More recently, the term redox flow battery (RFB) has become popular to describe electrochemical cells which utilize dissolved redox reactants as the fuel and oxidant [159]. With products and reactants which typically have faster kinetics and remain dissolved in liquid electrolytes, these flow batteries avoid phase change issues and achieve high cycle efficiencies up to 80% [3].

Both fuel cells and flow batteries operate by pumping fuel and oxidant separately between two electrodes which define a single electrochemical cell. During galvanic discharge operation the fuel undergoes oxidation at the anode and donates an electron to the external circuit while the oxidant is reduced and accepts an electron at the cathode from the external circuit. To preserve the electroneutrality of the contents of the

chamber, ions need to move from one compartment to the other. In vanadium flow batteries and most fuel cells, the sulfuric acid supporting electrolyte is acidic and therefore most of the ionic movement is due to hydrogen ions migrating through an ionomer membrane from the anode to the cathode during discharge of reactants as depicted in Fig. 2.

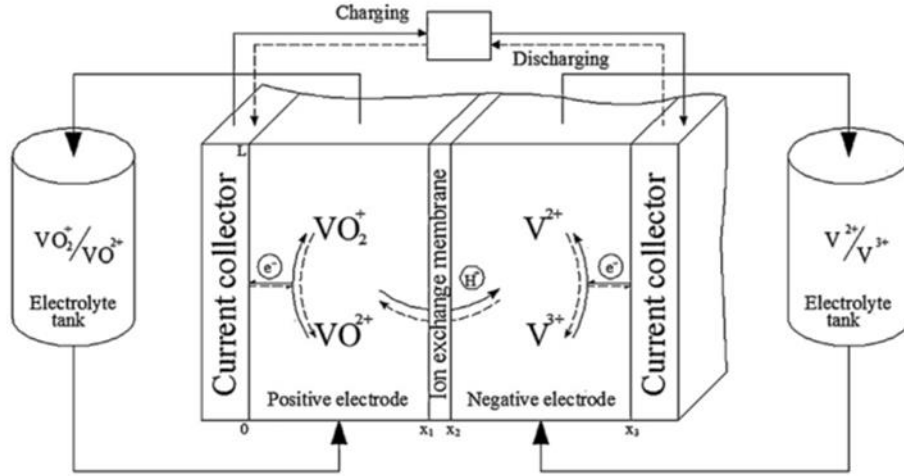
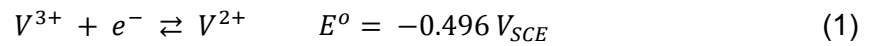


Figure 2. Schematic of all-vanadium redox flow battery where solid arrows indicate charging, and dashed arrows indicate discharging operation [160].

In this dissertation, all CLFC tests are performed with the same V^{2+}/V^{3+} and VO^{2+}/VO_2^+ reactants dissolved in a sulfuric acid supporting electrolyte as used in conventional vanadium redox flow batteries. These redox couples undergo the following reactions with corresponding standard potentials at 298 °K [161]:



As indicated in Fig. 1, V^{2+} fuel is oxidized to V^{3+} at the anode whereas the VO_2^+ oxidant is reduced to VO^{2+} at the cathode during discharge operation. Each of these reactions has a standard reduction potential E^0 relative to a reference, in the above case the saturated calomel reference. The equilibrium potential E_e of each reaction may

deviate significantly from these values depending on reactant concentrations C . The Nernst relations given in Eq. 3 & 4 define the concentration dependence of the thermodynamic equilibrium potentials for each reaction at standard temperature and pressure.

$$E_{e,a} = E_a^0 - \frac{RT}{nF} \ln \left(\frac{C_{V^{2+}}}{C_{V^{3+}}} \right) \quad (3)$$

$$E_{e,c} = E_c^0 - \frac{RT}{nF} \ln \left(\frac{C_{VO^{2+}}}{(C_{VO_2^+}) \cdot (C_{H^+})^2} \right) \quad (4)$$

where $R = 8.31 \text{ J} \cdot \text{K}^{-1} \cdot \text{mol}^{-1}$ is the gas constant, T is the temperature, n is the number of electrons transferred during the reaction and $F = 96485 \text{ C} \cdot \text{mol}^{-1}$ is Faraday's constant. When the fuel and oxidant are solely in contact with the anode and cathode respectively, the OCP of the cell is equal to the thermodynamic equilibrium potential given by:

$$OCP = E_{e,cell} = E_{e,c} - E_{e,a} \quad (5)$$

This open circuit potential is the maximum voltage which can be provided to an external circuit by the reactants in the cell. If an external voltage higher than this value is connected to the terminals of the cell, the reverse electrolytic or charging reactions will occur at each electrode. On the other hand, if a simple electrical load such as a resistor is connected to the cell, spontaneous galvanic reactions will occur at each electrode providing current to the external circuit, where the actual current provided will depend on the current-voltage relationship (or polarization behaviour) of the cell. The polarization curve seen in Fig. 2 provides a typical example of such behaviour.

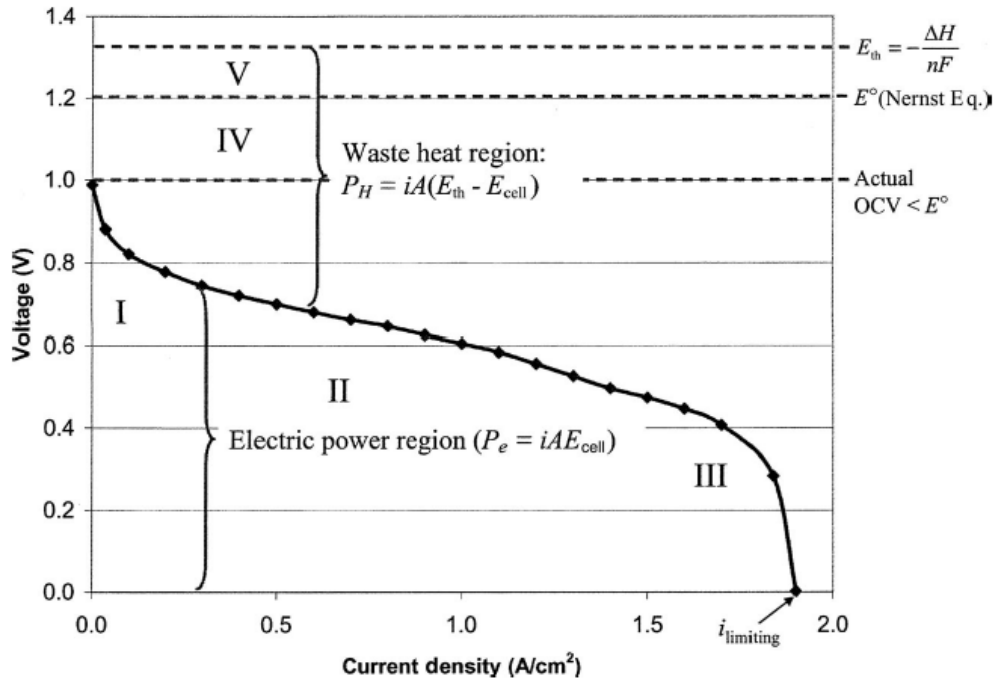


Figure 3. Typical electrochemical cell polarization curve demonstrating various sources of voltage loss: kinetic (I), ohmic (II), concentration (III), crossover (IV) and thermodynamic (V). Figure taken from Mench [14].

Although full polarization curves such as this are not often utilized for conventional flow batteries which typically operate only at low current densities, most CLFCs published in the literature are designed and operated as fuel cells for 'single-pass' discharge of reactants for which power density is often the metric of choice. As demonstrated in Fig. 2, the polarization of electrochemical cells is non-linear but can be understood in terms of various voltage losses. Besides the thermodynamic conditions already discussed which define the equilibrium potential of the cell through the Nernst relation, the other four sources of loss relate to: reaction kinetics, conductivity related ohmic loss, diffusion limited concentration effects and crossover of reactants.

2.1.1. Kinetics

When the potential of the electron conducting phase of the electrode interface is shifted away from the equilibrium potential of the reactants in the ionic conducting phase, electrochemical reactions will take place and current will flow between the two

phases in order to reach a new equilibrium between them. As with most chemical equilibria, the rates at which these electrochemical reactions occur are governed by exponential Arrhenius dynamics, where the difference in potential between phases is the driving force behind the reactions. This difference in potential is most conveniently defined as the overpotential η as in the following equation:

$$\eta = E - E_e \quad (6)$$

where E is the operating potential of the electrode and E_e is the previously defined equilibrium potential. The specific kinetic relationship which defines the amount of current being transferred between phases is the following current-overpotential equation [9]:

$$j = j_o \left[\frac{c_o^s}{c_o^b} \exp\left(\frac{-\alpha F \eta}{RT}\right) - \frac{c_r^s}{c_r^b} \exp\left(\frac{(1-\alpha) F \eta}{RT}\right) \right] \quad (7)$$

where j and j_o are the current and the exchange current density respectively [$\text{A}\cdot\text{cm}^{-2}$], α is the transfer coefficient of the reaction, the concentration subscripts (o, b) refer to the oxidized and reduced form of the chemical species, whereas the superscripts differentiate between the bulk and surface concentration (b, s). Both the transfer coefficient and exchange current density contribute to the overall kinetics of an electrochemical reaction which are often characterized by the heterogeneous rate constant k_o . These three kinetic parameters are related in the following way:

$$j_o = F k_o (c_o^b)^{(1-\alpha)} (c_r^b)^\alpha \quad (8)$$

When studying reaction kinetics it is generally preferable to avoid concentration gradients and therefore ensure that the surface concentration of reactants matches that of the bulk concentrations. In this case the above equation can be simplified to the more common Butler-Volmer or BV equation:

$$j = j_o \left[\exp\left(\frac{-\alpha F \eta}{RT}\right) - \exp\left(\frac{(1-\alpha) F \eta}{RT}\right) \right] \quad (8)$$

At large enough overpotentials ($> |100\text{mV}|$), one of the two terms in equation 8 becomes negligible so that it can be manipulated into the following Tafel equations in order to extract the kinetic parameters α and j_0 :

$$\log|j| = \log|j_{0,a}| - \frac{\alpha F}{2.3RT} \eta \quad \text{for } \eta < -0.1V \quad (9)$$

$$\log|j| = \log|j_{0,c}| + \frac{(1-\alpha)F}{2.3RT} \eta \quad \text{for } \eta > 0.1V \quad (10)$$

During discharge operation of a two electrode cell such as a fuel cell or flow battery, cathodic reduction current will flow through the cathode whereas an anodic oxidation current will flow through the anode. Due to conservation of current, these currents will be equal, but their associated overpotentials will depend on the exchange current density of their respective reactions. The sum of these overpotentials, otherwise known as the kinetic overpotential of the cell, represents the minimum voltage loss required to produce a given current from the two reactions.

2.1.2. Ohmic resistance

In addition to the limits imposed by the kinetics of each reaction, the conduction of current through the cell also engenders a voltage loss due to the finite conductivity of each cell component. Fortunately, whether these components are ionically conductive electrolytes or electronically conductive metals, they can typically be represented by a linear ohmic resistance. As the current passes through the anodic contact, the anode, the electrolyte, the cathode and finally the cathodic contact, it encounters a series of resistances associated with each phase which add up to a total cell resistance:

$$R_{cell} = R_{a,c} + R_a + R_{el} + R_c + R_{c,c} \quad (11)$$

Although these resistances are typically constant in simple electrochemical cells, they may vary with current in more complex cells. For cells with porous electrodes the electrolyte resistance in particular may depend on current due to the consumption of reactants in the electrode causing a shift in current distribution. This shift in current distribution will change the location of reactant conversion within the porous electrodes

and therefore change the distance and the associated electrolyte resistance between them. Regardless of these effects, when a steady state direct current I is drawn from this cell, the cell resistance produces an ohmic overpotential according to Ohm's law:

$$\eta_{ohmic} = IR_{cell} \quad (12)$$

When the resistance of a cell remains relatively constant throughout an experiment it is common practice to subtract this ohmic overpotential from polarization data for each measured current I , a method referred to as IR correction.

2.1.3. Mass transport

Although surface reactant concentrations are typically controlled during kinetic investigations, more generally these surface concentrations will tend to deviate from their bulk values during normal operation of an electrochemical cell. As reactants are converted or consumed, their surface concentration decreases according to the competition between the rate of mass transfer to the surface and the intrinsic kinetics of reaction. The rate of diffusional reactant transfer to the surface is proportional to the difference between bulk and surface concentration and often expressed in the following form:

$$N_j = K_m(c^b - c^s) \quad (13)$$

where N_j is the rate of mass transfer and K_m is a mass transfer coefficient determined by the fluid dynamics of the particular system. In phenomenological terms, this mass transfer coefficient represents the ratio between the diffusion coefficient D of the reactant species and the thickness of the stagnant diffusion boundary layer δ adjacent to the electrode surface:

$$K_m = \frac{D}{\delta} \quad (14)$$

In this way, the diffusion boundary layer thickness denotes a kind of mass transfer resistance which depends on the hydrodynamic conditions near the electrode. For instance, the diffusion layer thickness under quiescent electrolyte conditions will be

greater than under forced convection conditions. Expressions for the depletion boundary layer thickness or mass transfer coefficient can occasionally be solved analytically for simple hydrodynamic systems such as planar electrodes, but are more often determined empirically for more complex porous electrodes.

During any electrochemical reaction, the rate of mass transfer will necessarily be equal to the rate of reaction. Consequently, when either the mass transfer coefficient or depletion layer thickness is known, equation 13 can be used to solve for the surface concentration of the reactant which can be integrated into the general current-overpotential relation (equation 7) as in the example in equation 15 below:

$$FK_{m,o}(c_o^b - c_o^s) = j_o \left[\frac{c_o^s}{c_o^b} \exp\left(\frac{-\alpha F\eta}{RT}\right) - \frac{c_r^s}{c_r^b} \exp\left(\frac{(1-\alpha)F\eta}{RT}\right) \right] \quad (15)$$

Where $K_{m,o}$ is the mass transfer coefficient for the oxidant being consumed. For a reaction with a stoichiometry of 1, the rate of oxidant consumption is also equal to the rate of reductant creation:

$$FK_{m,o}(c_o^b - c_o^s) = FK_{m,r}(c_r^s - c_r^b) \quad (16)$$

Using these two relations (equations 15 & 16), the surface concentration can be solved for to determine the rate of reaction in the presence of mass transport effects.

2.1.4. Reactant crossover

Without any physical separation between anodic and cathodic compartments within a cell, the fuel and oxidant would be in contact with both electrodes and each other within the electrolyte. In both cases, this is known as crossover of reactants which diminishes the open circuit potential of the cell, as represented by section IV in Fig. 1. In alkaline hydrogen fuel cells, gaseous reactants were separated by a flowing liquid potassium hydroxide (KOH) electrolyte between hydrophobic porous electrodes, with crossover occurring by diffusion of gases through this separation [162]. Even in the case of conventional RFBs and DMFCs with solid electrolyte membranes, it is well known that reactants may diffuse across the membrane leading to an overall loss in current and

therefore coulombic efficiency [163], [164]. In the case of reactants which do not react homogeneously (directly) with each other, crossover leads to a mixed potential at either electrode which reduces the effective potential and/or current of the cell by consuming and reducing the concentration of the effective reactant. For example, methanol fuel crossing through the membrane and making contact with the cathode will be oxidized directly by the oxygen reduction reaction, thereby decreasing the amount of current provided to the external circuit.

Another manifestation of crossover is the decrease in reactant concentrations due to homogeneous reactions. As an example pertinent to the CLFCs found in this dissertation and discussed in detail in section 3.2, when vanadium reactants diffuse across the co-laminar interface, they will tend to react homogeneously with each other before reaching the opposite electrode. For example, a V^{2+} fuel ion may diffuse across the co-laminar interface into the oxidant stream and where it may react homogeneously with a VO_2^+ ion to become oxidized into a V^{3+} and again with another VO_2^+ ion to become a VO^{2+} ion, in this way consuming two oxidant VO_2^+ ions. As such, crossover of V^{2+} fuel leads to a net decrease in VO_2^+ concentration in the oxidant stream and vice versa.

In both heterogeneous and homogeneous cases, diffusive crossover of reactants leads to a net decrease in the average fuel and oxidant concentrations available for reaction. As reactant concentrations are at their maximum at open circuit conditions, the maximum crossover effect can be observed as a decrease in the open circuit potential of the cell with respect to the equilibrium potential specified by the Nernst equation as in Fig. 1.

2.2. Co-laminar flow cells

The present dissertation deals exclusively with flow cells which maintain separation of liquid reactants exclusively through the use of co-laminar flow, with no added physical separators, diffusion blocking channel features or ionomer membranes. This concept, demonstrated in Fig. 4, is possible only within a certain fluid velocity and length scale regime where fluid flow is smooth and free of any turbulence, known as the

laminar flow regime. Fluid dynamics are often characterized empirically using the dimensionless Reynold's number Re which represents a ratio between inertial and viscous forces as defined in equation 15 below:

$$Re = \frac{\rho v L}{\mu} \quad (17)$$

where ρ is the density of the fluid, v is the velocity of the fluid relative to the surface, L is the characteristic length of the surface and μ is the dynamic viscosity of the fluid. For flow within the centre channel of a CLFC, the characteristic length L is often referred to as the hydraulic diameter D_H . For a channel with a rectangular cross-section, the hydraulic diameter is given as:

$$D_H = \frac{4A}{P} \quad (18)$$

where A is the cross-sectional area and P is the perimeter of the cross-section. As an empirically determined value, a Reynold's number below 2000 is said to indicate laminar flow within a duct or pipe [165]. In contrast, flow within a flow-through porous electrode may resemble that within a packed bed of particles, where the characteristic length is taken as the average diameter of the particles. In such a configuration, flow is deemed to be within the laminar flow regime for a Reynold's lower than 180 [166], [167].

In addition to the necessary condition of laminar flow, the membraneless operation of co-laminar flow cells also imposes certain design restrictions to avoid undesirable crossover and efficiency loss. Although laminar flow precludes convective mixing, crossover of reactants across the co-laminar interface still occurs through diffusion. To avoid reactants from creating a mixed potential the average residence time t_{res} of those reactants in the electrochemical chamber must be shorter than their diffusion time t_{diff} across the centre channel to the opposite electrode. This criterion can be estimated using Einstein's relation for one-dimensional Brownian diffusion [168], as a lower bound on the average diffusion time:

$$t_{res} = \frac{L}{v} < \frac{W^2}{2D} = \overline{t_{diff}} \quad (19)$$

Equation 17 includes two design parameters, namely the channel length L and width W , the mean velocity v as an operational parameter and the diffusion coefficient D of the reactant species.

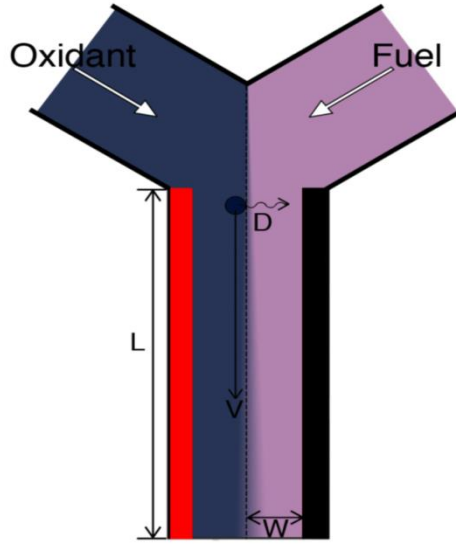


Figure 4. Schematic of CLFC operation.

Operationally, the velocity is determined by the flow rate Q and the channel height H and width W . With this parameter, the above relationship can be rearranged into dimensionless form to express the ratio of solute (reactant) advection to cross-stream diffusion in co-laminar flow cells:

$$\frac{QW}{2DHL} > 1 \quad (20)$$

As this relation is derived for an average diffusion time, it is necessary for the ratio to exceed 1 by an appreciable margin. Similarly, the above design rule can be derived from the Péclet number [165], a dimensionless ratio between advective and diffusive flux. As a general rule, the above relation holds when the rate of downstream advective transport exceeds the rate of diffusion across the channel.

Chapter 3. Summary of contributions

This dissertation presents several contributions to the technological progress of co-laminar flow cells which are contained in the six journal papers provided in Appendix A-F. This chapter summarizes these contributions and explains how they are connected towards the overall objective of this work and how they impact related fields of research in electrochemical energy conversion.

3.1. Microfluidic redox battery

The first study to be undertaken during this Ph. D. was to determine whether a CLFC could be operated as a rechargeable flow battery. To this end, a novel dual-pass device architecture was conceived, modelled and tested experimentally. This study was a joint design venture between my predecessor Jin Wook Lee and myself. Modelling efforts were conducted by Mr. Lee whereas fabrication and testing of the cell were my responsibilities. Highlights from this study were published as a short communication in *Lab on a Chip* in 2013 in order to expedite the publication of this first proof of concept for flow battery operation. Up until this point, all other CLFC research had focused entirely on single pass fuel cell operation.

The starting point for this study was to adapt the existing baseline design, depicted in Fig. 1-d), developed by Kjeang *et al.* and used by later researchers in the group so that unused fuel and oxidant could be collected separately. Due to the commonplace experimental methodology in the literature of using syringe pumps to inject reactants rather than peristaltic pumps, it was decided that a symmetric design which allowed forward and reverse reactant flow would be preferable. As such, merely splitting the outlet channel in the baseline design into a Y junction for separate reactant harvesting was not an option. Instead, a novel dual-pass architecture was conceived. The schematic depicted in Fig. 5 demonstrates the first realization of this idea.

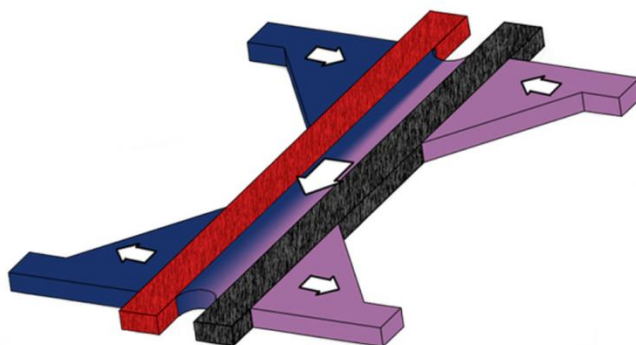


Figure 5. Novel dual-pass architecture [39].

The dual-pass concept involves segmenting the electrodes into two flow-through sections with a stagnant portion in the center where no electrolyte is flowing. During operation the reactants are injected into two inlets and flow through the upstream first section of the electrodes, then down the center channel and finally flow through the downstream section of the electrodes. The electrolyte will tend to flow this way as long as the center section of the electrode has a higher pressure drop than the combination of the upstream and downstream sections. This condition could be imposed more directly by splitting the electrode into upstream and downstream sections with a solid spacing section, as in the future studies by Ibrahim *et al.* which studied the parallel circuit operation and shunt current characteristics of the MRB architecture [99], [100]. . Using the same active flow-through electrode and channel dimensions as the baseline design (not including the stagnant center section), it was expected that the performance of the device would be comparable to the baseline. By forcing the electrolyte through the electrodes twice however, the dual-pass architecture increases the convective velocity of the electrolyte through each section of the electrodes, thereby improving mass transport at the same flow rate. Although not included in the communication, this was observed by higher performance at mid-range flow rates where mass transport losses are present. Although, this necessarily increases the pressure drop required for pumping the reactants, it was estimated through computational modelling based on Darcy's law that the power required for this operation is negligible ($< 1\%$) in comparison with the power output of the device. Due to the widening of the device in the outlet section however, it was also observed by a decrease in the OCV that the diffusive

crossover of reactants was considerably higher than the baseline design at the same flow rates.

It is well known in the vanadium redox battery literature that the onset of hydrogen evolution severely restricts the overpotential and therefore current used for recharging of vanadium reactants [3]. With such a limit on single pass fuel charging, it is imperative to avoid any unnecessary loss of converted reactants due to crossover. Although the first generation of the cell was able to perform a full charge-discharge cycle, the overall energy efficiency was quite impractical (<10%). It was therefore deemed essential to redesign the first realization in order to minimize the diffusive crossover. According to the fluid dynamics simulations, this could be achieved by limiting the expansion of the outlet channels as in the second generation dual-pass architecture found in Appendix A. Overall, the slimmer aspect ratio of the published microfluidic redox battery (MRB) generated less cross-stream diffusion at the outlets resulting in a 20% roundtrip efficiency. At the time of publication, this was the first case of rechargeable flow battery operation by a co-laminar flow cell.

3.2. Reactant recirculation in electrochemical co-laminar flow cells

With the successful recharging capabilities of the MRB design, it was decided to investigate and compare the limits of this design with the first generation dual-pass cell and the original baseline design for the purpose of fuel recirculation. By adding a Y-junction at the outlet of the baseline design it is possible to harvest unused reactants separately and recirculate them back through the inlets. In contrast, the dual-pass cells split the colaminar interface and force the reactants to pass through the electrodes a second time before exiting from the outlets. Moreover, the symmetric design allows the reactants to be recirculated simply by reversing the flow direction. For simple fuel cell discharge operation, both the 1st and 2nd generation dual-pass cells perform slightly better than the baseline design at lower flow rates due to the higher convective velocity through each section of the electrodes. In terms of multi-pass operation however, it was unclear which of these designs would lead to greater overall efficiency. Consequently,

this study seeks to quantify the losses due to reactant crossover and the resulting performance during multi-pass discharge operation.

A simple test to quantify the magnitude of reactant crossover is to monitor the open circuit potential at a range of flow rates. For the simple baseline Y-junction cell, it was observed that the OCP matched the total potential of the reactants for flow rates above $10 \mu\text{L}\cdot\text{min}^{-1}$, indicating that any crossover was insufficient to affect the concentration of reactants at either electrode. Below this value the OCP decreases with flow rate. As the splitting of reactants occurs further downstream from the electrodes it can be expected that diffusion will affect the outlet concentrations at a higher flow rate than this. By measuring the outlet concentrations at open circuit conditions, it is possible to quantify directly the loss associated with this splitting of reactant streams. Indeed, it was observed that crossover at the outlets levels off at a minimum of 2% at $100 \mu\text{L}\cdot\text{min}^{-1}$. The presence of this 2% minimum crossover which is independent of flow rate indicates that regardless of flow velocity, there is always some loss associated with the imperfect splitting of the co-laminar interface into separate streams. Any source of pressure difference between streams such as pump pulsation, syringe diameter discrepancies or device fabrication defects will result in such asymmetric positioning and splitting of the interface. This important result sets a benchmark for all CLFC research intended for recirculation operation.

Performing the same tests on the dual-pass architectures revealed more of the expected relationships between crossover and flow rate. The simple OCP measurements support very well the design changes made between the earlier 1st generation dual-pass cell and the 2nd generation MRB. Both cells reach the same maximum OCP at $300 \mu\text{L}\cdot\text{min}^{-1}$, however the 2nd generation design decreases less for flow rates below this value, indicating that the slimmer design is effective for reducing diffusive crossover. In general however, the degree of crossover and the maximum OCP is worse than the Y-junction due to the reactants passing through the electrodes after the splitting occurs. This is confirmed by the direct measurement of outlet concentrations which shows higher loss at all flow rates. For the dual-pass architectures it is also noteworthy that there is a more direct correlation between the OCP measurements and concentration loss at the outlets. As such, this study demonstrates

the usefulness of OCP measurements for benchmarking dual pass cell designs in particular.

Regarding discharge performance of the cells, simple polarization curve analysis at a range of flow rates indicates that the dual-pass MRB has favorable mass transport and therefore fuel utilization at lower flow rates than the baseline Y-junction. For recirculation capability it was necessary to perform multi-pass experiments to determine whether this mass transport advantage is sufficient to offset the added concentration loss due to the higher diffusive crossover. In the end, the difference observed between the Y-junction baseline and the 2nd generation dual-pass MRB is as expected. Over multiple passes of the same reactants, the MRB produces more power and converts more reactants than the Y-junction, however the OCP measured at each pass indicates more concentration loss at each pass. From a reactant energy point of view, this may lead to an overall reduction in energy efficiency at certain flow rates. From a broader perspective, this indicates that each design has advantages which would suit different applications. For high power operation with abundant reactants, a dual pass design may be preferable, whereas a simple baseline design may be more suitable for high efficiency operation.

3.3. Direct measurement of electrochemical reaction kinetics in flow-through porous electrodes

Considering the relatively low roundtrip efficiency of the MRB device and the minimum 2% concentration loss observed during reactant recirculation, it was clear that most CLFC devices will likely be used for single pass operation. For this reason, it was decided to focus on increasing the overall power density of the baseline cell for the remainder of the project. In order to improve the power density of electrochemical cells, it is commonplace to first investigate the kinetic limitations of the intended reactants. Determining the kinetics of vanadium redox reactions on the carbon paper FTPEs used in our cells is not necessarily a straightforward undertaking.

Although many studies have been conducted on the kinetics of vanadium reactions on the graphite felts used in conventional VRBs, the vast majority of these

have used cyclic voltammetry to establish the heterogeneous rate constants, which is well known to be prone to error when highly porous electrodes are used. Similarly, a previous study in this group by Lee *et al.* used both cyclic voltammetry and Tafel analysis in stirred solutions to determine these rates on the carbon paper electrodes used in our CLFC technology [169]. Due to the curvature and unusually high Tafel slopes observed in that study it was clear that diffusion effects were still present, indicating that perhaps the stirring of the beaker solution was insufficient to replenish the reactants within the porous carbon paper. As such, the objective of this study was to develop a new experimental methodology for extracting kinetic parameters specifically for FTPEs. The primary contributions stemming from this work are the design and validation of a microfluidic three-electrode analytical flow cell for testing the polarization behavior of an FTPE in the absence of diffusion effects. This study was published as a short communication in *Electrochemistry Communications* in 2015.

The three-electrode cell consists of a thin foil or deposited reference electrode placed upstream from a thin section of the material under study as a working electrode, in a straight microchannel with a rectangular cross-section of the same height as that used in our CLFCs. A substantially larger flow-through counter electrode is placed further downstream to provide the current being drawn through the working electrode which determines the potential measured by the reference electrode. The whole cell is designed to measure the polarization of the working electrode at a range of flow rates in a similar flow-through configuration as used in our CLFCs. As flow rates are increased reactants are replenished by forced convection through the working electrode and mass transport effects may be reduced to the point where kinetic rates may be determined by standard Tafel analysis. Validation of this setup was performed by 100% conversion of reactants at low flow rates, leading to a limiting current equal to this degree of conversion.

The results obtained in this study indicate that such a technique is both feasible and valuable for certain reactions and flow-through porous materials. For very fast reactions, the flow rates necessary to mitigate mass transport limitations may become impractical for the particular device; either leading to leaking of the cell or damage to the electrode structure. Ideally, the material under study should also have a reasonably

narrow pore size distribution so that the average flow velocity through the pores is relatively regular. Besides these general findings, the specific exchange currents for both of the vanadium redox reactions were determined on Toray carbon paper. When normalized by the ESA of the electrode, these exchange current densities were found to be $I_0 \approx 0.17 \text{ mA}\cdot\text{cm}^{-2}$ for $\text{V}^{2+}/\text{V}^{3+}$ and $I_0 \approx 0.17 \text{ mA}\cdot\text{cm}^{-2}$ for the $\text{VO}^{2+}/\text{VO}_2^+$ redox couple. In both cases the values were 1.5 orders of magnitude higher than those measured previously by the stirred solution method which supports the idea that the porous interior of the electrode had not participated in the reaction. Overall, the considerably slower rate measured for the $\text{V}^{2+}/\text{V}^{3+}$ redox couple provides much stronger evidence than that found in the literature that this is the limiting reaction in VRBs.

3.4. The importance of wetting in carbon paper electrodes for vanadium redox reactions

The fourth study in this dissertation was a collaboration between our lab and that of Prof. Em. Maria Skyllas-Kazacos, one of the founders of the vanadium redox battery technology in the 1980's. The initial research proposal for the collaboration involved adapting the microfluidic three-electrode analytical cell mentioned above to the thicker felt materials used in their systems. This proposal was subsequently changed to investigate thicker versions of the same carbon paper used in our CLFCs as these were suggested in the literature to lead to higher power density in vanadium redox batteries [170], [171]. With the relative kinetic rates established in the previous study, more focus was placed on understanding the source of the rate difference and various electrode treatments for increasing the rate of the limiting $\text{V}^{2+}/\text{V}^{3+}$ redox couple in particular. As explained below, it was understood during the study that some of the difference was related to the wetting of the carbon paper by each electrolyte.

Many studies have been conducted on various electrochemical, chemical and thermal treatments of porous carbon or graphite electrodes for vanadium redox batteries. Unfortunately, the vast majority of these have relied upon changes in peak separation and peak current in cyclic voltammetry to determine the effects of those treatments. This methodology is well-known to produce erroneous conclusions due to the porosity of the electrode material invalidating the semi-infinite diffusion criterion

necessary for this type of analysis [172]–[176]. This has produced considerable inconsistency and confusion in the VRB literature regarding which electrode treatments may be most effective and even which reaction is truly limiting. The goal of this study is to demonstrate the influence of porosity and the importance of wetting and contact between the electrode and electrolyte and suggest a more complete methodology which provides an alternative interpretation of many of the results in the literature.

The starting point for this study is a clear demonstration of the influence of surface hydrophobicity on the wettability of the internal porous structure of carbon paper. This was done by immersing as-received carbon paper into a blank sulfuric acid electrolyte and observing the capacitance via cyclic voltammetry and electrochemical impedance spectroscopy (EIS). The hydrophobic carbon paper does not make good contact with the electrolyte as seen by the presence of a gaseous layer trapped within and on the surface of the carbon paper, in addition to a repulsive meniscus formed around the edge of the liquid electrolyte. By applying an oxidizing potential to the electrode, the gas layer is seen to disappear and the electrolyte is clearly observed to soak up into the electrode in real time. This electrochemical hydrophilic treatment produces an associated increase in the capacitance of the electrode.

When applying the same treatment in the presence of the limiting V^{2+}/V^{3+} redox couple, the same spontaneous wetting phenomenon is observed with a similar increase in capacitance. However, the reduction and oxidation peaks of the cyclic voltammogram (CV) profiles are also observed to change, increasing in current and decreasing in peak separation, which has typically been interpreted as an increase in catalytic activity for the reaction. A close look at the EIS data however, indicates that the increased wetting merely increases the ESA rather than having any specific catalytic effect, as verified by the inversely proportional relationship between the increase in capacitance and decrease charge transfer resistance. Another chemical pretreatment which was observed to have the same effect is immersion of the carbon paper in the oxidizing VO^{2+}/VO_2^+ solution. The significance of the results are further reinforced by the forced convection of the V^{2+}/V^{3+} electrolyte through an as-received sample of carbon paper which dislodges some of the trapped gas within the electrode and produces more overall contact between the electrode and electrolyte. This produces a similar increase in

capacitance, decrease in charge transfer resistance and decrease in CV peak separation without changing the surface properties of the carbon at all. This suggests that the decrease in CV peak separation is an artifact of the porosity of the sample, and has no bearing on the catalytic properties of the electrode. This final result is meant to further stress the idea that many of the treatments suggested to have catalytically beneficial effects may in fact be merely increasing the wetting of the porous electrodes.

Whether the hydrophilic oxidation pretreatment of the electrode is electrochemical or chemical in nature, a maximum effect is reached when the entire electrode is wetted by the electrolyte. The final aim of this study is to investigate whether further oxidative treatment may have beneficial effects. To this end, several techniques are combined including cyclic voltammetry, EIS and the Tafel analysis made possible by the analytical flow cell previously developed. In all cases, it is observed that the 'fully wetted' electrode can still be further enhanced by additional applied oxidative potentials, but that these effects are temporary and equilibrate back to a maximum wetted/capacitance/ESA state over time. Although the wetting of the electrode has a substantial effect, the kinetics of the fully wetted electrode determined via Tafel analysis still indicate that the $\text{VO}^{2+}/\text{VO}_2^+$ redox couple undergoes the faster reaction.

For both conventional vanadium redox batteries and the CLFCs which utilize the same reactants, the overall value of this study is the well-founded implication that most of the surface treatments suggested in the literature for increasing the kinetics of the vanadium reactions may not be worthwhile. Beyond simply making the electrode surfaces more hydrophilic and therefore increasing the ESA, there is no indication that such treatments affect the intrinsic rates of reaction. This suggests that using higher surface area electrodes may be the only effective way for improving reaction rates.

3.5. *In situ* enhancement of flow-through porous electrodes with carbon nanotubes via flowing deposition

As indicated by the study on wetting of carbon paper, increasing the surface area of the carbon paper may be the only way to increase the rates of vanadium redox reactions. With a new validated experimental technique for measuring these reaction

rates within FTPEs it was time to develop a strategy to increase their surface area. Although much higher surface area carbon materials exist such as carbon aerogels or nanofoams, after a brief investigation into their properties, it was found that these materials generally had poor electronic conductivity and inadequate pore size distributions due to the presence of large cracks which produced uneven flow velocities. Instead, it was decided to investigate the possibility of fabricating higher surface area FTPEs by adding nanomaterials to an existing carbon paper electrode. Although this approach has been implemented in the conventional VRB literature, it is always in the form of a pre-treatment of the electrodes prior to assembly [177]–[179]. In contrast, this work proposed a novel *in situ* method for depositing nanomaterials on FTPEs which could be used on fully assembled cells. By flowing a temporary suspension of carbon nanotubes (CNT) through the carbon paper electrodes it was observed that some of these would adhere to the carbon paper or form agglomerated clusters which would become lodged within or at the surface of the carbon paper and thereby increase the surface available for reaction.

In order to quantify the flowing deposition method being proposed, the three electrode analytical flow cell was used to measure the increase in exchange current density of a single carbon paper electrode after several deposition steps. For the deposition liquid, a very small quantity of CNTs was suspended temporarily in simple deionized water by sonication. Without dispersant the carbon nanotubes tend to self-agglomerate and sediment within water over time. If used immediately after sonication however, the temporary suspension can be injected into the analytical cell and through the working electrode. After each deposition step (0.1 ml of suspension), the cell was rinsed forcefully with deionized water to remove loosely attached CNTs. After each rinsing step, the vanadium reactants were injected into the cell and the kinetics of reaction were determined via Tafel analysis under rapid flow conditions and EIS under stagnant electrolyte conditions. In this study, it was decided to focus exclusively on the limiting V^{2+}/V^{3+} reaction. From this series of tests, the exchange current density for this reaction and capacitance of the sample were observed to increase by over an order of magnitude after a total of 0.4 ml of suspension was injected. From SEM investigations it was found that the CNTs could form fiber bundles which adhered to the carbon paper fibers by simple Van der Waals forces. In addition, CNTs would also agglomerate in

large clusters which would become lodged at the upstream entrance of the flow-through porous carbon paper. In this way, the CNTs would form a high surface area nanoporous blanketing layer on the electrode. Moreover, the high frequency EIS results demonstrated no change in the ohmic resistance of the cells which suggests that the physically agglomerated CNTs are electrically well connected to, and share the relatively good conductivity, of the underlying carbon paper scaffold. In addition, with adequate rinsing steps to remove any loosely adhered material, the performance after deposition was observed to be stable over several hours of continuous potentiostatic operation.

The promising results observed in the analytical cell prompted the same deposition and rinsing method to be attempted *in situ* on a fully assembled CLFC. In this experiment, the suspension was firstly injected through the $\text{VO}^{2+}/\text{VO}_2^+$ cathode of the CLFC and observed to produce no measurable effects, as expected from the considerably higher rate and negligible kinetic overpotential for this reaction. In contrast, when the same deposition suspension was injected through the anode of the cell, both the EIS spectrum (Nyquist plot) and polarization curve were improved. Demonstrating the deposition method in steps, it was found that the charge transfer resistance of the cell could be reduced to the point where the Nyquist plot resembled the single $\text{VO}^{2+}/\text{VO}_2^+$ reaction. Similarly, the power output of the cell was increased by up to 70%, particularly in the kinetic region of the polarization curve. Without any change in the ohmic resistance of the cell, the mass transport region of the curve was also observed to improve slightly. Lastly, the effect of the added CNTs on the pressure drop through the enhanced electrode was measured via pressure transducer. As the first experimental results for pressure drop in a CLFC the data corroborates earlier computational results based on Darcy's Law for this carbon paper. Although the deposition of CNTs increases the pressure drop across the electrode, the power required was determined to be negligible (< 1%) in comparison to the power output of the device in all cases.

In addition to the improvement in our CLFC performance, the utility of the flowing deposition method developed in this study may be of considerable interest to the broader fields of flow batteries, fuel cells, water treatment and any other electrochemical flow cell relying upon FTPEs. As the probability for deposition increases with the convective flux of suspension, the surface area is likely to increase most where the flow

is greatest. From a kinetic standpoint this is the ideal case for deposition as opposed to other ex situ deposition methods such as spray coating which merely apply the material randomly or evenly on the entire electrode. In addition the clustering of deposition material will tend to reduce the overall pore size distribution and may thereby enhance the mass transport characteristics of the flow-through porous electrodes by increasing the average flow velocity. As a low cost *in situ* method, the flowing deposition may be reapplied to fully assembled cells to recover any lost performance. In addition, the use of a temporary suspension provides a universal strategy for customized combinations, thereby enabling greener deposition processes and chemical flexibility. These key advancements warranted protection of the method under a patent application [180], with the expectation that the method could be adapted to many types of industrially relevant electrochemical flow reactors such as capacitive deionization cells, fuel cells and flow batteries.

3.6. Approaching the power density limits of aqueous electrochemical flow cells

The final study in this dissertation combines all of the lessons learned and strategies developed in the past 4 years towards the optimization of CLFC device design for maximum power output. After the positive results obtained with the flowing deposition method it was decided to optimize the architecture of the cell. With mass transport characteristics fundamentally related to the flow velocity and porous properties of the material, initial efforts were instead focused on the ohmic losses of the cell and their associated design parameters such as channel width and electrode size. To understand these ohmic losses, an in depth study was conducted to determine the ionic conductivity of the electrolytes. In this way, it was discovered that the ionic conductivity of the center channel was responsible for roughly two thirds of the total resistance. By reducing the center channel width to half its original size, the resistance could then be reduced by one third while also decreasing the size of the cell. From a parametric study on electrode length, width, and channel width it was found that this strategy was the only general way to increase the power density of the cell through architecture modifications.

Although the vanadium fuel and oxidant are charged from the same stock electrolyte starting point, they differ in hydrogen ion concentration due to the fact that hydrogen ions are consumed during reduction of vanadium oxides as in Equation 2. For this reason, it was found that the ionic conductivity of the V^{2+}/V^{3+} fuel was lower than the VO^{2+}/VO_2^+ oxidant. The concentration of reactants was therefore diminished to increase the relative concentration of sulfuric acid and associated hydrogen ions in order for all electrolytes to approach the maximum ionic conductivity of 3 M sulfuric acid. Although this reduction in concentration also reduces the kinetics of the redox reactions, it was intended to counterbalance this issue with the added electrode surface area during deposition. Overall this increase in electrolyte conductivity contributed to a further 2 Ω reduction in cell resistance. Lastly, it was determined that the finite electronic conductivity of the porous carbon paper electrodes was another significant contribution to the cell resistance, which was nearly eliminated through the use of current collectors. Moreover, the order of magnitude larger conductivity of the current collector material made it possible to decrease the width of the electrodes and overall device footprint. Again, it was strategized that the loss in surface area associated with thinner electrodes could be compensated for by the flowing deposition method. Overall, the changes implemented reduced the cell resistance from roughly 30 to 8 Ω and reduced the projected device area and volume by half.

Once the cell design was optimized to minimize both the device footprint and ohmic resistance, both cell electrodes were enhanced via the flowing deposition treatment previously invented, leading to a record setting power density of roughly 1.45 $W \cdot cm^{-2}$. By performing IR correction on the polarization curves however, it was realised that considerable mass transport effects were still present. As explained previously, the *in situ* flowing deposition method involves an incremental treatment of the electrode followed by a rinsing step to remove loosely attached material. Although the method forms a nanoporous layer at the upstream entrance of the electrode, this layer may not be the ideal case in terms of pore size distribution. Due to unavoidable handling effects, the flow dynamics during treatment and rinsing will inevitably be slightly different from electrolyte flow during operation. As such, it was decided to attempt dynamic flowing deposition during operation by suspending minute quantities of CNTs in the electrolyte itself. When operated at suitable flow rates, additional CNTs would consequently

become lodged in the largest pores through which the flow was greatest, thereby reducing the average pore size distribution of the electrode. In contrast to the original method, this dynamic deposition process would inevitably form an equilibrium between the deposition rate and the pressure build up from pore constriction. As the deposition material builds up, the electrode becomes blocked similarly to a river being naturally dammed by a log jam. As the pore sizes decrease further, the pressure increases until some of the deposited material is washed away, at which point the process begins anew. In some cases, this phenomenon was observed as a regular pulsation in the potentiostatic current. Although this deposition invariably leads to less stability in the current output, the average current is considerably greater than using the original flowing deposition method, with much of the effect being displayed in the mass transport region of the polarization curve. With this alternative method the power output of the optimized cell was increased from 13 to 30 mW. This 17 mW gain in power output was achieved with a minute amount of CNTs, estimated at less than 0.002 \$, a performance increase cost of roughly 0.10 \$·W⁻¹. This enabled the optimized cell to produce up to 2.01 W·cm⁻², which is the highest power density known for any cell based on vanadium reactants, whether CLFC or conventional, and over twice the power density of the leading CLFC found in Table 1.

Chapter 4. Conclusions

Since their advent, considerable diversity has emerged in the field of co-laminar flow cells. Among the innovations aimed towards increasing the performance of CLFCs, the baseline design developed in this group based on flow-through porous electrodes was an important benchmark for the technology and a logical starting point for this project. As an engineering dissertation, this project has involved both fundamental research and technological development. Beginning with new device architectures for added functionality, the present work evolved to include several other contributions including extensive component characterization, the conception of new experimental methods, novel material fabrication and device optimization. All of the lessons learned throughout the project were synthesized into a final CLFC capable of producing four times the power density of the original baseline design. This final chapter will summarize these main findings and provide suggestions for future work and predictions about the future of co-laminar flow cell technology.

4.1. Present work

The first study completed in this dissertation involved the design of novel device architectures for rechargeable battery operation. Apart from the symmetry of the design allowing flow reversal, the dual-pass architecture emanating from this work exhibited another distinct benefit over the baseline design; namely higher convective velocity engendering improved mass transport through the electrodes. This allowed the cell to be more effective at the lower flow rates required for fuel charging, leading to a 20% round trip energy efficiency. On the other hand, the dual-pass architecture also had an inherent drawback due to the decrease in downstream velocity causing larger reactant diffusion at the outlets. This source of concentration loss was the subject of the 2nd study in this dissertation, in which all architectures were characterized and compared with respect to their performance for reactant recirculation. It was found that both the

single pass baseline Y-junction and the dual-pass architectures could be further optimized to reduce the crossover due to diffusion but that ideal separation of reactant streams was impossible due to device and pump imperfections which lead to asymmetric crossover of reactants at all flow rates. This ~2% loss in concentration for each pass represented a fundamental limit on reactant recirculation and rechargeable operation. In order to achieve high efficiency operation, it was therefore found that single pass performance would have to be improved, a conclusion which motivated subsequent work into device power output.

The next study included in this dissertation involved the development of a new experimental technique for characterizing the kinetics and general polarization behavior of flow-through porous electrodes. Using a microfluidic three-electrode cell, materials such as the carbon paper could be characterized individually in the same flow-through configuration encountered within the CLFCs. With this technique the exchange currents for the $\text{VO}^{2+}/\text{VO}_2^+$ and $\text{V}^{2+}/\text{V}^{3+}$ reactions on carbon paper were measured to be $i_0 \approx 3 \text{ mA}\cdot\text{cm}^{-2}$ and $i_0 = 0.048 \text{ mA}\cdot\text{cm}^{-2}$ respectively, indicating that $\text{V}^{2+}/\text{V}^{3+}$ was the limiting reaction in the CLFCs being developed. Further work into the kinetics of vanadium redox reactions was conducted in collaboration with UNSW to understand the effect of electrode wetting on these reactions. In this fourth study it was demonstrated that much of the methodology on porous carbon materials in the VRB literature erroneously views changes in voltammetric peak separation as indicative of changes in intrinsic kinetics of vanadium reactions. To challenge this interpretation it was shown that forcing $\text{V}^{2+}/\text{V}^{3+}$ electrolyte through carbon paper had the same effect on a CV, thereby indicating that this was a result of contact area between the electrode and electrolyte, *i.e.*: ESA, rather than any changes in reaction kinetics. As a more fundamental study on methodology and interpretation, a direct correlation between capacitance and charge transfer resistance was observed and associated with the simple wetting of the electrode perceived visually. Moreover it was suggested that both electrochemical and chemical oxidation of the carbon paper electrodes produced essentially the same effect. In both cases, the treatment favored complete wetting of the electrode by the $\text{V}^{2+}/\text{V}^{3+}$ electrolyte which had a predictable effect on the exchange current density, charge transfer resistance and measured capacitance of the carbon paper sample. Although some of the sluggishness of this reaction can be associated with its poor carbon wetting

properties, it was again observed that even after oxidation treatment this reaction continues to be considerably slower than the $\text{VO}^{2+}/\text{VO}_2^+$ reaction. In general, these results indicate that efforts to improve the intrinsic kinetics of these reactions may be ineffective. In addition to their impact on the present CLFC design, it is hoped and expected that these two methodology studies will be of much use to researchers in the VRB and wider flow battery community.

The implications stemming from the kinetic studies mentioned above added further incentive to develop other ways of improving reaction rates. To this end, the deposition of nanomaterials was attempted to increase the ESA of the FTPEs. In this fifth study, carbon nanotubes were deposited by flowing a temporary suspension of the CNTs through the carbon paper electrodes. The deposition was quantified via the analytical three-electrode cell developed in the 3rd study and shown to increase the exchange current of the working electrode by over an order of magnitude. The method was also used *in situ* to increase the surface area of the anode in a CLFC, leading to a 70% improvement in the power output of the cell in the low current density kinetic regime. With a negligible effect on the pumping power loss through the electrode, this method is expected to find use in other electrochemical cells involving FTPEs and is therefore likely to be of interest to researchers in the field of fuel cells and flow batteries among others.

The success of the flowing deposition method prompted more effort towards reducing the ohmic losses of the cell. By identifying these losses, the ohmic resistance of the cell was effectively reduced to 8 Ω , a fraction of the original 30 Ω value and approaching the minimum theoretical value for a CLFC. With this target achieved, it was decided to add CNTs to the electrolytes as well in order to attain a dynamic equilibrium between the deposition and loss of CNTs during operation. In this way, the logjam concept could be taken to its logical conclusion, forcing the deposition to occur until a minimum pore size and maximum electrochemically active surface area is attained. This dynamic flowing deposition greatly improved the mass transport of reactants allowing the cell to achieve up to 2 Wcm^{-2} , a record breaking power density which brings the CLFC technology within the range demanded by on-chip power and cooling applications.

4.2. Future work

Although this dissertation contains several contributions culminating in record setting CLFC power density, several engineering challenges remain before this technology can become commercially viable. Chief among these challenges is the scale-up of the technology. The final cell design included in this dissertation required certain critical adjustments to the electrode and channel width in order to achieve the highest power density possible. The other cell dimensions such as electrode length or channel height were not changed with respect to the baseline cell. With the use of current collectors, it is conceivable that longer electrodes could be implemented with a proportional increase in operating electrolyte flow rate without any loss in power density; and similarly for the channel height. With such strategies it may be possible to increase the total power output of single cells to reduce the need for complex stacking and open up new potential applications beyond low power sensor devices.

In addition to larger single cells, efficient and robust stacking of cells remains an important step towards co-laminar flow devices with suitable total power output. If a low profile on-chip device structure is sought then this hurdle would necessitate clever design and integration of space efficient reactant manifolds. If a more conventional sandwich structure is to be pursued, then the concepts demonstrated in this work would first have to be adapted and replicated with that architecture. A critical obstacle common to both approaches is the precise pressure control required to maintain several co-laminar interfaces. Any deviation or pulsation in inlet or outlet pressure would produce an associated asymmetry in the position of the interface. For recirculating cells this would lead to an increase in concentration loss at the outlets. Depending on the severity of the pressure difference and the width of the center channel this asymmetry may also produce a drop in the OCP and therefore performance of the affected cell.

Regardless of the performance metrics achieved by CLFCs, application matching and device integration remain the most important issue for this technology moving forward. As CLFC device performance and functionality continue to improve, more research in this direction is essential.

4.3. Technological outlook

As explained in the introduction, with single co-laminar flow cell power output below 1 W, substantial difficulties remain for this technology to achieve the kW scale which typically favors other open electrochemical flow cells such as conventional fuel cells and flow batteries. Unsurprisingly, this has shifted research in CLFCs more towards niche applications with lower power requirements. By avoiding the use of membranes CLFCs potentially benefit from longer lifetimes by eliminating one source of degradation and early failure. This characteristic makes them particularly suitable as backup power supplies for sensors in remote locations provided a reliable reactant pumping mechanism can be found. The high relative component cost of membranes also makes inexpensive CLFC technology particularly appropriate for disposable power sources such as point of care medical devices operating on passively pumped glucose as a fuel. For this reason, it is expected that the current interdisciplinary research trend in this area will continue. On the higher end of the power spectrum, on-chip powering and cooling of microprocessors is the most ambitious application being considered. It is not yet clear whether CLFC technology will become a viable solution for this purpose, but it is likely that many results stemming from this work will find a useful technological outlet.

Although CLFC technology is still in an early phase of development, apart from the niche applications identified above, it remains to be seen if the technology will directly contribute to the global energy supply to any significant degree. It is however, very likely that the technology will continue to contribute indirectly, as it already has, to the advancement of other associated electrochemical technologies. As inexpensive and accessible lab scale platforms, CLFCs are ideal for testing both conventional and exotic reactant combinations. For the low-profile on-chip fabrication style in particular, the transparency of the microfluidic channel materials which makes visual inspection of the reactions easier, further adds to their practicality. As research in renewable energy continues to expand it is expected that CLFCs will become commonplace in electrochemical experimentation.

References

- [1] R. M. Darling, K. G. Gallagher, J. A. Kowalski, S. Ha, and F. R. Brushett, "Pathways to low-cost electrochemical energy storage: a comparison of aqueous and nonaqueous flow batteries," *Energy Environ. Sci.*, vol. 7, no. 11, pp. 3459–3477, 2014.
- [2] G. L. Soloveichik, "Flow Batteries: Current Status and Trends," *Chem. Rev.*, vol. 115, no. 20, pp. 11533–11558, 2015.
- [3] M. Skyllas-Kazacos, M. H. Chakrabarti, S. A. Hajimolana, F. S. Mjalli, and M. Saleem, "Progress in Flow Battery Research and Development," *J. Electrochem. Soc.*, vol. 158, no. 8, pp. R55–R79, 2011.
- [4] H. Ibrahim, A. Ilinca, and J. Perron, "Energy storage systems-Characteristics and comparisons," *Renew. Sustain. Energy Rev.*, vol. 12, no. 5, pp. 1221–1250, 2008.
- [5] N. S. Lewis, "Toward cost-effective solar energy use.," *Science*, vol. 315, no. 5813, pp. 798–801, Feb. 2007.
- [6] B. Dunn, H. Kamath, and J.-M. Tarascon, "Electrical energy storage for the grid: a battery of choices.," *Science*, vol. 334, no. 6058, pp. 928–35, Nov. 2011.
- [7] B. Scrosati and J. Garche, "Lithium batteries: Status, prospects and future," *J. Power Sources*, vol. 195, no. 9, pp. 2419–2430, 2010.
- [8] J. Morse, "Micro-fuel cell power sources," *Int. J. Energy Res.*, vol. 31, no. January, pp. 576–602, 2007.
- [9] A. J. Bard and L. R. Faulkner, *Electrochemical Methods: Fundamentals and Applications*, 2nd ed. John Wiley & Sons Inc., 2001.
- [10] M. Winter and R. J. Brodd, "What are batteries, fuel cells, and supercapacitors?," *Chem. Rev.*, vol. 104, no. 10, pp. 4245–69, Oct. 2004.
- [11] S. J. Peighambardoust, S. Rowshanzamir, and M. Amjadi, "Review of the proton exchange membranes for fuel cell applications," *Int. J. Hydrogen Energy*, vol. 35, no. 17, pp. 9349–9384, Sep. 2010.
- [12] H. Vafiadis and M. Skyllas-Kazacos, "Evaluation of membranes for the novel

vanadium bromine redox flow cell,” *J. Memb. Sci.*, vol. 279, no. 1–2, pp. 394–402, Aug. 2006.

- [13] R. Borup, J. Meyers, B. Pivovar, Y. S. Kim, R. Mukundan, N. Garland, D. Myers, M. Wilson, F. Garzon, D. Wood, P. Zelenay, K. More, K. Stroh, T. Zawodzinski, J. Boncella, J. E. McGrath, M. Inaba, K. Miyatake, M. Hori, K. Ota, Z. Ogumi, S. Miyata, A. Nishikata, Z. Siroma, Y. Uchimoto, K. Yasuda, K. Kimijima, and N. Iwashita, “Scientific Aspects of Polymer Electrolyte Fuel Cell Durability and Degradation,” *Chem. Rev.*, vol. 107, no. 10, pp. 3904–3951, Oct. 2007.
- [14] M. M. Mench, *Fuel Cell Engines*. John Wiley & Sons Inc., 2008.
- [15] M. Skyllas-Kazacos and M. Kazacos, “State of charge monitoring methods for vanadium redox flow battery control,” *J. Power Sources*, vol. 196, no. 20, pp. 8822–8827, Oct. 2011.
- [16] E. H. Yu, X. Wang, U. Krewer, L. Li, and K. Scott, “Direct oxidation alkaline fuel cells: from materials to systems,” *Energy Environ. Sci.*, vol. 5, no. 2, pp. 5668–5680, 2012.
- [17] C. Houchins, G. Kleen, J. Spendelow, J. Kopasz, D. Peterson, N. Garland, D. Ho, J. Marcinkoski, K. Martin, R. Tyler, and D. Papageorgopoulos, “U.S. DOE Progress Towards Developing Low-Cost, High Performance, Durable Polymer Electrolyte Membranes for Fuel Cell Applications,” *Membranes (Basel)*, vol. 2, no. 4, pp. 855–878, 2012.
- [18] A. Heinzl, C. Hebling, M. Müller, M. Zedda, and C. Müller, “Fuel cells for low power applications,” *J. Power Sources*, vol. 105, no. 2, pp. 250–255, 2002.
- [19] S. ichi Yamazaki, Z. Siroma, H. Senoh, T. Ioroi, N. Fujiwara, and K. Yasuda, “A fuel cell with selective electrocatalysts using hydrogen peroxide as both an electron acceptor and a fuel,” *J. Power Sources*, vol. 178, no. 1, pp. 20–25, 2008.
- [20] C. M. Moore, S. D. Minteer, and R. S. Martin, “Microchip-based ethanol/oxygen biofuel cell,” *Lab Chip*, vol. 5, no. 2, pp. 218–225, Feb. 2005.
- [21] S. A. Mousavi Shaegh, N.-T. Nguyen, S. M. Mousavi Ehteshami, and S. H. Chan, “A membraneless hydrogen peroxide fuel cell using Prussian Blue as cathode material,” *Energy Environ. Sci.*, vol. 5, no. 8, pp. 8225–8228, 2012.
- [22] A. K. Shukla, R. K. Raman, and K. Scott, “Advances in Mixed-Reactant Fuel Cells,” *Fuel Cells*, vol. 5, no. 4, pp. 436–447, Dec. 2005.
- [23] W. Sung and J.-W. Choi, “A membraneless microscale fuel cell using non-noble catalysts in alkaline solution,” *J. Power Sources*, vol. 172, no. 1, pp. 198–208, Oct. 2007.

- [24] M. Togo, A. Takamura, T. Asai, H. Kaji, and M. Nishizawa, "An enzyme-based microfluidic biofuel cell using vitamin K3-mediated glucose oxidation," *Electrochim. Acta*, vol. 52, no. 14, pp. 4669–4674, Apr. 2007.
- [25] M. Togo, A. Takamura, T. Asai, H. Kaji, and M. Nishizawa, "Structural studies of enzyme-based microfluidic biofuel cells," *J. Power Sources*, vol. 178, no. 1, pp. 53–58, Mar. 2008.
- [26] S. Tominaka, S. Ohta, H. Obata, T. Momma, and T. Osaka, "On-chip fuel cell: micro direct methanol fuel cell of an air-breathing, membraneless, and monolithic design.," *J. Am. Chem. Soc.*, vol. 130, no. 32, pp. 10456–7, Aug. 2008.
- [27] S. Topcagic and S. D. Minteer, "Development of a membraneless ethanol/oxygen biofuel cell," *Electrochim. Acta*, vol. 51, no. 11, pp. 2168–2172, Feb. 2006.
- [28] M. L. Perry and T. F. Fuller, "A Historical Perspective of Fuel Cell Technology in the 20th Century," *J. Electrochem. Soc.*, vol. 149, no. 7, p. S59, 2002.
- [29] F. R. Brushett, H. T. Duong, J. W. Ng, R. L. Behrens, A. Wieckowski, and P. J. A. Kenis, "Investigation of Pt, Pt₃Co, and Pt₃Co/Mo Cathodes for the ORR in a Microfluidic H₂/O₂ Fuel Cell," *J. Electrochem. Soc.*, vol. 157, no. 6, pp. B837–B845, 2010.
- [30] F. R. Brushett, M. S. Naughton, J. W. D. Ng, L. Yin, and P. J. A. Kenis, "Analysis of Pt/C electrode performance in a flowing-electrolyte alkaline fuel cell," *Int. J. Hydrogen Energy*, vol. 37, no. 3, pp. 2559–2570, Feb. 2012.
- [31] H.-R. Jhong, F. R. Brushett, L. Yin, D. M. Stevenson, and P. J. A. Kenis, "Combining Structural and Electrochemical Analysis of Electrodes Using Micro-Computed Tomography and a Microfluidic Fuel Cell," *J. Electrochem. Soc.*, vol. 159, no. 3, pp. B292–B298, Jan. 2012.
- [32] M. S. Naughton, F. R. Brushett, and P. J. A. Kenis, "Carbonate resilience of flowing electrolyte-based alkaline fuel cells," *J. Power Sources*, vol. 196, no. 4, pp. 1762–1768, Feb. 2011.
- [33] M. A. Burns, B. N. Johnson, S. N. Brahmasandra, K. Handique, J. R. Webster, M. Krishnan, T. S. Sammarco, P. M. Man, D. Jones, D. Heldsinger, C. H. MAstrangelo, and D. T. Burke, "An Integrated Nanoliter DNA Analysis Device," *Science (80-.)*, vol. 282, no. 5388, pp. 484–487, Oct. 1998.
- [34] S. Takayama, E. Ostuni, P. LeDuc, K. Naruse, D. E. Ingber, and G. M. Whitesides, "Subcellular positioning of small molecules.," *Nature*, vol. 411, no. 6841, p. 1016, Jun. 2001.
- [35] R. F. Ismagilov, T. D. Rosmarin, P. J. A. Kenis, D. T. Chiu, W. Zhang, H. A. Stone, and G. M. Whitesides, "Pressure-driven laminar flow in tangential

- microchannels: an elastomeric microfluidic switch.,” *Anal. Chem.*, vol. 73, no. 19, pp. 4682–4687, Oct. 2001.
- [36] G. M. Whitesides, “The origins and the future of microfluidics.,” *Nature*, vol. 442, no. 7101, pp. 368–373, Jul. 2006.
- [37] R. Ferrigno, A. D. Stroock, T. D. Clark, M. Mayer, and G. M. Whitesides, “Membraneless Vanadium Redox Fuel Cell Using Laminar Flow,” *J. Am. Chem. Soc.*, vol. 124, no. 44, pp. 12930–12931, Nov. 2002.
- [38] E. R. Choban, L. J. Markoski, A. Wieckowski, and P. J. A. Kenis, “Microfluidic fuel cell based on laminar flow,” *J. Power Sources*, vol. 128, no. 1, pp. 54–60, Mar. 2004.
- [39] M.-A. Goulet and E. Kjeang, “Co-laminar flow cells for electrochemical energy conversion,” *J. Power Sources*, vol. 260, pp. 186–196, Aug. 2014.
- [40] E. Kjeang, *Microfluidic Fuel Cells and Batteries*. Springer, 2014.
- [41] E. Kjeang, N. Djilali, and D. Sinton, “Microfluidic fuel cells: A review,” *J. Power Sources*, vol. 186, no. 2, pp. 353–369, Jan. 2009.
- [42] S. A. Mousavi Shaegh, N.-T. Nguyen, and S. H. Chan, “A review on membraneless laminar flow-based fuel cells,” *Int. J. Hydrogen Energy*, vol. 36, no. 9, pp. 5675–5694, May 2011.
- [43] M. N. Nasharudin, S. K. Kamarudin, U. a. Hasran, and M. S. Masdar, “Mass transfer and performance of membrane-less micro fuel cell: A review,” *Int. J. Hydrogen Energy*, vol. 39, no. 2, pp. 1039–1055, Jan. 2014.
- [44] B. Ho and E. Kjeang, “Microfluidic fuel cell systems,” *Cent. Eur. J. Eng.*, vol. 1, no. 2, pp. 123–131, Apr. 2011.
- [45] J. L. Cohen, D. J. Volpe, D. A. Westly, A. Pechenik, and H. D. Abruña, “A dual electrolyte H₂/O₂ planar membraneless microchannel fuel cell system with open circuit potentials in excess of 1.4 V.,” *Langmuir*, vol. 21, no. 8, pp. 3544–3550, Apr. 2005.
- [46] E. R. Choban, J. S. Spendelow, L. Gancs, A. Wieckowski, and P. J. A. Kenis, “Membraneless laminar flow-based micro fuel cells operating in alkaline, acidic, and acidic/alkaline media,” *Electrochim. Acta*, vol. 50, no. 27, pp. 5390–5398, Sep. 2005.
- [47] F. Chen, M.-H. Chang, and C.-W. Hsu, “Analysis of membraneless microfuel cell using decomposition of hydrogen peroxide in a Y-shaped microchannel,” *Electrochim. Acta*, vol. 52, no. 25, pp. 7270–7277, Sep. 2007.

- [48] S. Hasegawa, K. Shimotani, K. Kishi, and H. Watanabe, "Electricity Generation from Decomposition of Hydrogen Peroxide," *Electrochem. Solid-State Lett.*, vol. 8, no. 2, pp. A119–A121, 2005.
- [49] A. Bazylak, D. Sinton, and N. Djilali, "Improved fuel utilization in microfluidic fuel cells: A computational study," *J. Power Sources*, vol. 143, no. 1–2, pp. 57–66, Apr. 2005.
- [50] M. H. Sun, G. Velasco Casquillas, S. S. Guo, J. Shi, H. Ji, Q. Ouyang, and Y. Chen, "Characterization of microfluidic fuel cell based on multiple laminar flow," *Microelectron. Eng.*, vol. 84, no. 5–8, pp. 1182–1185, May 2007.
- [51] S. K. Yoon, G. W. Fichtl, and P. J. A. Kenis, "Active control of the depletion boundary layers in microfluidic electrochemical reactors," *Lab Chip*, vol. 6, no. 12, pp. 1516–24, Dec. 2006.
- [52] C. . Chen and P. Yang, "Performance of an air-breathing direct methanol fuel cell," *J. Power Sources*, vol. 123, no. 1, pp. 37–42, Sep. 2003.
- [53] G. Girishkumar, B. McCloskey, A. C. Luntz, S. Swanson, and W. Wilcke, "Lithium–Air Battery: Promise and Challenges," *J. Phys. Chem. Lett.*, vol. 1, no. 14, pp. 2193–2203, Jul. 2010.
- [54] R. S. Jayashree, L. Gancs, E. R. Choban, A. Primak, D. Natarajan, L. J. Markoski, and P. J. A. Kenis, "Air-breathing laminar flow-based microfluidic fuel cell," *J. Am. Chem. Soc.*, vol. 127, no. 48, pp. 16758–16759, Dec. 2005.
- [55] E. Kjeang, B. Proctor, A. Brolo, D. A. Harrington, N. Djilali, and D. Sinton, "High-performance microfluidic vanadium redox fuel cell," *Electrochim. Acta*, vol. 52, no. 15, pp. 4942–4946, Apr. 2007.
- [56] E. Kjeang, J. McKechnie, D. Sinton, and N. Djilali, "Planar and three-dimensional microfluidic fuel cell architectures based on graphite rod electrodes," *J. Power Sources*, vol. 168, no. 2, pp. 379–390, Jun. 2007.
- [57] K. S. Salloum, J. R. Hayes, C. A. Friesen, and J. D. Posner, "Sequential flow membraneless microfluidic fuel cell with porous electrodes," *J. Power Sources*, vol. 180, no. 1, pp. 243–252, May 2008.
- [58] E. Kjeang, R. Michel, D. A. Harrington, N. Djilali, and D. Sinton, "A microfluidic fuel cell with flow-through porous electrodes," *J. Am. Chem. Soc.*, vol. 130, no. 12, pp. 4000–4006, Mar. 2008.
- [59] J. Phirani and S. Basu, "Analyses of fuel utilization in microfluidic fuel cell," *J. Power Sources*, vol. 175, no. 1, pp. 261–265, Jan. 2008.
- [60] D. H. Ahmed, H. B. Park, and H. J. Sung, "Optimum geometrical design for

improved fuel utilization in membraneless micro fuel cell,” *J. Power Sources*, vol. 185, no. 1, pp. 143–152, Oct. 2008.

- [61] H. B. Park, D. H. Ahmed, K. H. Lee, and H. J. Sung, “An H-shaped design for membraneless micro fuel cells,” *Electrochim. Acta*, vol. 54, no. 18, pp. 4416–4425, Jul. 2009.
- [62] D. H. Ahmed and H. B. Park, “The geometrical design of membraneless micro fuel cells: Failure and success,” *Int. J. Energy Res.*, vol. 34, no. May 2009, pp. 878–896, 2010.
- [63] A. Ebrahimi Khabbazi, A. J. Richards, and M. Hoorfar, “Numerical study of the effect of the channel and electrode geometry on the performance of microfluidic fuel cells,” *J. Power Sources*, vol. 195, no. 24, pp. 8141–8151, Dec. 2010.
- [64] J. Xuan, D. Y. C. Leung, M. K. H. Leung, M. Ni, and H. Wang, “A computational study of bifunctional oxygen electrode in air-breathing reversible microfluidic fuel cells,” *Int. J. Hydrogen Energy*, vol. 36, no. 15, pp. 9231–9241, Jul. 2011.
- [65] J. Xuan, M. K. H. Leung, D. Y. C. Leung, M. Ni, and H. Wang, “Hydrodynamic focusing in microfluidic membraneless fuel cells: Breaking the trade-off between fuel utilization and current density,” *Int. J. Hydrogen Energy*, vol. 36, no. 17, pp. 11075–11084, Aug. 2011.
- [66] J. Xuan, M. K. H. Leung, D. Y. C. Leung, and H. Wang, “Laminar flow-based fuel cell working under critical conditions: The effect of parasitic current,” *Appl. Energy*, vol. 90, no. 1, pp. 87–93, Feb. 2012.
- [67] J. Peng, Z. Y. Zhang, and H. T. Niu, “A Three-Dimensional Two-Phase Model for a Membraneless Fuel Cell Using Decomposition of Hydrogen Peroxide with Y-Shaped Microchannel,” *Fuel Cells*, vol. 12, no. 6, pp. 1009–1018, Dec. 2012.
- [68] H. Wang, D. Y. C. Leung, and J. Xuan, “Modeling of an air cathode for microfluidic fuel cells: Transport and polarization behaviors,” *Int. J. Hydrogen Energy*, vol. 36, no. 22, pp. 14704–14718, Nov. 2011.
- [69] I. B. Sprague, D. Byun, and P. Dutta, “Effects of reactant crossover and electrode dimensions on the performance of a microfluidic based laminar flow fuel cell,” *Electrochim. Acta*, vol. 55, no. 28, pp. 8579–8589, Dec. 2010.
- [70] R. Hassanshahi and M. Fathipour, “Design of a New Microfluidic Fuel Cell for Enhanced Current Density and Performance,” *Int. J. Adv. Renew. Energy Res.*, vol. 1, no. 11, pp. 649–654, 2012.
- [71] J. Xuan, M. K. H. Leung, D. Y. C. Leung, and H. Wang, “Towards orientation-independent performance of membraneless microfluidic fuel cell: Understanding the gravity effects,” *Appl. Energy*, vol. 90, no. 1, pp. 80–86, Feb. 2012.

- [72] C.-F. Flores-Rivera, "Modeling and Behavior Analysis of a Membraneless Fuel Cell," *ISRN Appl. Math.*, vol. 2012, pp. 1–24, 2012.
- [73] I. B. Sprague and P. Dutta, "Modeling of Diffuse Charge Effects in a Microfluidic Based Laminar Flow Fuel Cell," *Numer. Heat Transf. Part A Appl.*, vol. 59, no. 1, pp. 1–27, Jan. 2011.
- [74] I. Sprague and P. Dutta, "Depth Averaged Analytic Solution for a Laminar Flow Fuel Cell with Electric Double Layer Effects," *SIAM J. Appl. Math.*, vol. 72, no. 4, pp. 1149–1168, 2012.
- [75] F. R. Brushett, R. S. Jayashree, W.-P. Zhou, and P. J. A. Kenis, "Investigation of fuel and media flexible laminar flow-based fuel cells," *Electrochim. Acta*, vol. 54, no. 27, pp. 7099–7105, Nov. 2009.
- [76] J.-C. Shyu and C.-L. Huang, "Characterization of bubble formation in microfluidic fuel cells employing hydrogen peroxide," *J. Power Sources*, vol. 196, no. 6, pp. 3233–3238, Mar. 2011.
- [77] J.-C. Shyu, C.-S. Wei, C.-J. Lee, and C.-C. Wang, "Investigation of bubble effect in microfluidic fuel cells by a simplified microfluidic reactor," *Appl. Therm. Eng.*, vol. 30, no. 13, pp. 1863–1871, Sep. 2010.
- [78] D. T. Whipple, R. S. Jayashree, D. Egas, N. Alonso-Vante, and P. J. A. Kenis, "Ruthenium cluster-like chalcogenide as a methanol tolerant cathode catalyst in air-breathing laminar flow fuel cells," *Electrochim. Acta*, vol. 54, no. 18, pp. 4384–4388, Jul. 2009.
- [79] D. Morales-Acosta, H. Rodríguez G., L. A. Godinez, and L. G. Arriaga, "Performance increase of microfluidic formic acid fuel cell using Pd/MWCNTs as catalyst," *J. Power Sources*, vol. 195, no. 7, pp. 1862–1865, Apr. 2010.
- [80] F. M. Cuevas-Muñiz, M. Guerra-Balcázar, F. Castaneda, J. Ledesma-García, and L. G. Arriaga, "Performance of Au and AuAg nanoparticles supported on Vulcan in a glucose laminar membraneless microfuel cell," *J. Power Sources*, vol. 196, no. 14, pp. 5853–5857, Jul. 2011.
- [81] D. Morales-Acosta, M. D. Morales-Acosta, L. A. Godinez, L. Álvarez-Contreras, S. M. Duron-Torres, J. Ledesma-García, and L. G. Arriaga, "PdCo supported on multiwalled carbon nanotubes as an anode catalyst in a microfluidic formic acid fuel cell," *J. Power Sources*, vol. 196, no. 22, pp. 9270–9275, Nov. 2011.
- [82] Z. Li, Y. Zhang, P. R. LeDuc, and K. B. Gregory, "Microbial electricity generation via microfluidic flow control," *Biotechnol. Bioeng.*, vol. 108, no. 9, pp. 2061–2069, Sep. 2011.
- [83] A. Zebda, L. Renaud, M. Cretin, F. Pichot, C. Innocent, R. Ferrigno, and S. Tingry,

- "A microfluidic glucose biofuel cell to generate micropower from enzymes at ambient temperature," *Electrochem. commun.*, vol. 11, no. 3, pp. 592–595, Mar. 2009.
- [84] A. Zebda, L. Renaud, M. Cretin, C. Innocent, F. Pichot, R. Ferrigno, and S. Tingry, "Electrochemical performance of a glucose/oxygen microfluidic biofuel cell," *J. Power Sources*, vol. 193, no. 2, pp. 602–606, Sep. 2009.
- [85] A. Zebda, L. Renaud, M. Cretin, C. Innocent, R. Ferrigno, and S. Tingry, "Membraneless microchannel glucose biofuel cell with improved electrical performances," *Sensors Actuators B Chem.*, vol. 149, no. 1, pp. 44–50, Aug. 2010.
- [86] J. R. Hayes, A. M. Engstrom, and C. Friesen, "Orthogonal flow membraneless fuel cell," *J. Power Sources*, vol. 183, no. 1, pp. 257–259, Aug. 2008.
- [87] K. S. Salloum and J. D. Posner, "Counter flow membraneless microfluidic fuel cell," *J. Power Sources*, vol. 195, no. 19, pp. 6941–6944, Oct. 2010.
- [88] A. S. Hollinger, R. J. Maloney, R. S. Jayashree, D. Natarajan, L. J. Markoski, and P. J. A. Kenis, "Nanoporous separator and low fuel concentration to minimize crossover in direct methanol laminar flow fuel cells," *J. Power Sources*, vol. 195, no. 11, pp. 3523–3528, Jun. 2010.
- [89] W. Huo, Y. Zhou, and H. Zhang, "Microfluidic Direct Methanol Fuel Cell with Ladder-Shaped Microchannel for Decreased Methanol Crossover," *Int. J. Electrochem. Sci.*, vol. 8, pp. 4827–4838, 2013.
- [90] M. R. Thorson, F. R. Brushett, C. J. Timberg, and P. J. A. Kenis, "Design rules for electrode arrangement in an air-breathing alkaline direct methanol laminar flow fuel cell," *J. Power Sources*, vol. 218, pp. 28–33, Nov. 2012.
- [91] N. Da Mota, D. A. Finkelstein, J. D. Kirtland, C. A. Rodriguez, A. D. Stroock, and H. D. Abruña, "Membraneless, room-temperature, direct borohydride/cerium fuel cell with power density of over 0.25 W/cm²," *J. Am. Chem. Soc.*, vol. 134, no. 14, pp. 6076–6079, Apr. 2012.
- [92] J. W. Lee and E. Kjeang, "Chip-embedded thin film current collector for microfluidic fuel cells," *Int. J. Hydrogen Energy*, vol. 37, no. 11, pp. 9359–9367, Jun. 2012.
- [93] W. A. Braff, M. Z. Bazant, and C. R. Buie, "Membrane-less hydrogen bromine flow battery," *Nat. Commun.*, vol. 4, p. 2346, Jan. 2013.
- [94] J. W. Lee, M.-A. Goulet, and E. Kjeang, "Microfluidic Redox Battery," *Lab Chip*, vol. 13, pp. 2504–2507, 2013.

- [95] S. A. Mousavi Shaegh, N.-T. Nguyen, S. H. Chan, and W. Zhou, "Air-breathing membraneless laminar flow-based fuel cell with flow-through anode," *Int. J. Hydrogen Energy*, vol. 37, no. 4, pp. 3466–3476, Feb. 2012.
- [96] D. Fuerth and A. Bazylak, "Up-Scaled Microfluidic Fuel Cells With Porous Flow-Through Electrodes," *J. Fluids Eng.*, vol. 135, no. 2, p. 021102, Mar. 2013.
- [97] N. Arjona, M.-A. Goulet, M. Guerra-Balcazar, J. Ledesma-Garcia, E. Kjeang, and L. G. Arriaga, "Direct Formic Acid Microfluidic Fuel Cell with Pd Nanocubes Supported on Flow-Through Microporous Electrodes," *ECS Electrochem. Lett.*, vol. 4, no. 4, pp. F24–F28, 2015.
- [98] J. W. Lee and E. Kjeang, "Nanofluidic Fuel Cell," *J. Power Sources*, vol. 242, pp. 472–477, Nov. 2013.
- [99] O. a. Ibrahim, M. -a. Goulet, and E. Kjeang, "Microfluidic Electrochemical Cell Array in Series: Effect of Shunt Current," *J. Electrochem. Soc.*, vol. 162, no. 7, pp. F639–F644, 2015.
- [100] O. A. Ibrahim, M.-A. Goulet, and E. Kjeang, "In-situ characterization of symmetric dual-pass architecture of microfluidic co-laminar flow cells," *Electrochim. Acta*, vol. 187, pp. 277–285, 2015.
- [101] E. Ortiz-Ortega, M.-A. Goulet, J. W. Lee, M. Guerra-Balcázar, N. Arjona, E. Kjeang, J. Ledesma-García, and L. G. Arriaga, "A nanofluidic direct formic acid fuel cell with a combined flow-through and air-breathing electrode for high performance.," *Lab Chip*, vol. 14, no. 24, pp. 4596–8, 2014.
- [102] D. Krishnamurthy, E. O. Johansson, J. W. Lee, and E. Kjeang, "Computational modeling of microfluidic fuel cells with flow-through porous electrodes," *J. Power Sources*, vol. 196, no. 23, pp. 10019–10031, Dec. 2011.
- [103] I. B. Sprague and P. Dutta, "Improved kinetics from ion advection through overlapping electric double layers in nano-porous electrodes," *Electrochim. Acta*, vol. 91, pp. 20–29, Feb. 2013.
- [104] Y. Yu, Y. Zuo, C. Zuo, X. Liu, and Z. Liu, "A Hierarchical Multiscale Model for Microfluidic Fuel Cells with Porous Electrodes," *Electrochim. Acta*, vol. 116, pp. 237–243, Jan. 2014.
- [105] K. S. Salloum and J. D. Posner, "A membraneless microfluidic fuel cell stack," *J. Power Sources*, vol. 196, no. 3, pp. 1229–1234, Feb. 2011.
- [106] S. Moore, D. Sinton, and D. Erickson, "A plate-frame flow-through microfluidic fuel cell stack," *J. Power Sources*, vol. 196, no. 22, pp. 9481–9487, Nov. 2011.
- [107] B. Ho and E. Kjeang, "Planar Multiplexing of Microfluidic Fuel Cells," *J. Fluids*

Eng., vol. 135, no. 2, p. 021304, Mar. 2013.

- [108] H. Wang, S. Gu, D. Y. C. Leung, H. Xu, M. K. H. Leung, L. Zhang, and J. Xuan, "Development and characteristics of a membraneless microfluidic fuel cell array," *Electrochim. Acta*, vol. 135, pp. 467–477, Jul. 2014.
- [109] M.-A. Goulet and E. Kjeang, "Reactant recirculation in electrochemical co-laminar flow cells," *Electrochim. Acta*, vol. 140, pp. 217–224, 2014.
- [110] J. Marschewski, S. Jung, P. Ruch, N. Prasad, S. Mazzotti, B. Michel, and D. Poulikakos, "Mixing with herringbone-inspired microstructures: overcoming the diffusion limit in co-laminar microfluidic devices," *Lab Chip*, 2015.
- [111] M. J. González-Guerrero, J. P. Esquivel, D. Sánchez-Molas, P. Godignon, F. X. Muñoz, F. J. Del Campo, F. Giroud, S. D. Minter, and N. Sabaté, "Membraneless glucose/O₂ microfluidic enzymatic biofuel cell using pyrolyzed photoresist film electrodes," *Lab Chip*, pp. 2972–2979, May 2013.
- [112] T. Beneyton, I. P. M. Wijaya, C. Ben Salem, a D. Griffiths, and V. Taly, "Membraneless glucose/O₂ microfluidic biofuel cells using covalently bound enzymes," *Chem. Commun. (Camb)*, vol. 49, no. 11, pp. 1094–6, Feb. 2013.
- [113] H.-Y. Wang and J.-Y. Su, "Membraneless microfluidic microbial fuel cell for rapid detection of electrochemical activity of microorganism," *Bioresour. Technol.*, vol. 145, pp. 271–274, Jan. 2013.
- [114] D. Ye, Y. Yang, J. Li, X. Zhu, Q. Liao, B. Deng, and R. Chen, "Performance of a microfluidic microbial fuel cell based on graphite electrodes," *Int. J. Hydrogen Energy*, pp. 1–6, Jun. 2013.
- [115] D. Desmaële, L. Renaud, and S. Tingry, "A wireless sensor powered by a flexible stack of membraneless enzymatic biofuel cells," *Sensors Actuators B Chem.*, 2015.
- [116] A. Dector, R. A. Escalona-Villalpando, D. Dector, V. Vallejo-Becerra, A. U. Chávez-Ramírez, L. G. Arriaga, and J. Ledesma-García, "Perspective use of direct human blood as an energy source in air-breathing hybrid microfluidic fuel cells," *J. Power Sources*, vol. 288, pp. 70–75, 2015.
- [117] L. Renaud, D. Selloum, and S. Tingry, "Xurography for 2D and multi-level glucose/O₂ microfluidic biofuel cell," *Microfluid. Nanofluidics*, pp. 1407–1416, 2015.
- [118] S. Tominaka, H. Obata, and T. Osaka, "On-chip direct methanol fuel cells of a monolithic design: consideration on validity of active-type system," *Energy Environ. Sci.*, vol. 2, no. 8, pp. 845–848, 2009.

- [119] K. G. Lim and G. T. R. Palmore, "Microfluidic biofuel cells: the influence of electrode diffusion layer on performance.," *Biosens. Bioelectron.*, vol. 22, no. 6, pp. 941–947, Jan. 2007.
- [120] A. Zebda, C. Innocent, L. Renaud, and M. Cretin, "Enzyme-Based Microfluidic Biofuel Cell to Generate Micropower," *Enzyme*, 2011.
- [121] R. K. Arun, W. Bekele, and A. Ghatak, "Self oscillating potential generated in patterned micro-fluidic fuel cell," *Electrochim. Acta*, vol. 87, pp. 489–496, Jan. 2013.
- [122] E. Kjeang, A. G. Brolo, D. A. Harrington, N. Djilali, and D. Sinton, "Hydrogen Peroxide as an Oxidant for Microfluidic Fuel Cells," *J. Electrochem. Soc.*, vol. 154, no. 12, pp. B1220–B1226, 2007.
- [123] P. O. López-Montesinos, N. Yossakda, A. Schmidt, F. R. Brushett, W. E. Pelton, and P. J. A. Kenis, "Design, fabrication, and characterization of a planar, silicon-based, monolithically integrated micro laminar flow fuel cell with a bridge-shaped microchannel cross-section," *J. Power Sources*, vol. 196, no. 10, pp. 4638–4645, May 2011.
- [124] M. M. Sabry, A. Sridhar, D. Atienza, P. Ruch, and B. Michel, "Integrated Microfluidic Power Generation and Cooling for Bright Silicon MPSoCs," in *Proceedings of the IEEE/ACM 2014 Design Automation and Test in Europe (DATE) Conference*, 2014, vol. 1, no. 1, pp. 70–75.
- [125] P. Ruch, T. Brunschweiler, W. Escher, S. Paredes, and B. Michel, "Toward five-dimensional scaling: How density improves efficiency in future computers," *IBM J. Res. Dev.*, vol. 55, no. 5, pp. 15:1–15:13, 2011.
- [126] E. R. Choban, P. Waszczuk, and P. J. A. Kenis, "Characterization of Limiting Factors in Laminar Flow-Based Membraneless Microfuel Cells," *Electrochem. Solid-State Lett.*, vol. 8, no. 7, p. A348, 2005.
- [127] J. L. Cohen, D. A. Westly, A. Pechenik, and H. D. Abruña, "Fabrication and preliminary testing of a planar membraneless microchannel fuel cell," *J. Power Sources*, vol. 139, no. 1–2, pp. 96–105, Jan. 2005.
- [128] A. Déctor, F. M. Cuevas-Muñiz, M. Guerra-Balcázar, L. a. Godínez, J. Ledesma-García, and L. G. Arriaga, "Glycerol oxidation in a microfluidic fuel cell using Pd/C and Pd/MWCNT anodes electrodes," *Int. J. Hydrogen Energy*, pp. 1–6, Jan. 2013.
- [129] A. Déctor, J. P. Esquivel, M. J. González, M. Guerra-Balcázar, J. Ledesma-García, N. Sabaté, and L. G. Arriaga, "Formic acid microfluidic fuel cell evaluation in different oxidant conditions," *Electrochim. Acta*, vol. 92, pp. 31–35, Mar. 2013.
- [130] R. Galindo, A. Dector, L. G. Arriaga, S. Gutiérrez, and P. Herrasti, "Maghemite as

a catalyst for glucose oxidation in a microfluidic fuel cell,” *J. Electroanal. Chem.*, vol. 671, pp. 38–43, Apr. 2012.

- [131] A. Li, S. H. Chan, and N.-T. Nguyen, “A laser-micromachined polymeric membraneless fuel cell,” *J. Micromechanics Microengineering*, vol. 17, no. 6, pp. 1107–1113, Jun. 2007.
- [132] I. B. Sprague, P. Dutta, and S. Ha, “Characterization of a membraneless direct-methanol micro fuel cell,” *Proc. Inst. Mech. Eng. Part A J. Power Energy*, vol. 223, no. 7, pp. 799–808, Nov. 2009.
- [133] A. S. Hollinger and P. J. A. Kenis, “Manufacturing all-polymer laminar flow-based fuel cells,” *J. Power Sources*, vol. 240, pp. 486–493, Oct. 2013.
- [134] R. S. Jayashree, D. Egas, J. S. Spendelow, D. Natarajan, L. J. Markoski, and P. J. A. Kenis, “Air-Breathing Laminar Flow-Based Direct Methanol Fuel Cell with Alkaline Electrolyte,” *Electrochem. Solid-State Lett.*, vol. 9, no. 5, pp. A252–A256, 2006.
- [135] R. S. Jayashree, S. K. Yoon, F. R. Brushett, P. O. Lopez-Montesinos, D. Natarajan, L. J. Markoski, and P. J. A. Kenis, “On the performance of membraneless laminar flow-based fuel cells,” *J. Power Sources*, vol. 195, no. 11, pp. 3569–3578, Jun. 2010.
- [136] S. A. Mousavi Shaegh, N.-T. Nguyen, and S. H. Chan, “An air-breathing microfluidic formic acid fuel cell with a porous planar anode: experimental and numerical investigations,” *J. Micromechanics Microengineering*, vol. 20, no. 10, p. 105008, Oct. 2010.
- [137] A. S. Gago, D. Morales-Acosta, L. G. Arriaga, and N. Alonso-Vante, “Carbon supported ruthenium chalcogenide as cathode catalyst in a microfluidic formic acid fuel cell,” *J. Power Sources*, vol. 196, no. 3, pp. 1324–1328, Feb. 2011.
- [138] S. A. Mousavi Shaegh, N.-T. Nguyen, and S. H. Chan, “Air-breathing microfluidic fuel cell with fuel reservoir,” *J. Power Sources*, vol. 209, pp. 312–317, Jul. 2012.
- [139] J. Ma, A. S. Gago, and N. Alonso-Vante, “Performance Study of Platinum Nanoparticles Supported onto MWCNT in a Formic Acid Microfluidic Fuel Cell System,” *J. Electrochem. Soc.*, vol. 160, no. 8, pp. F859–F866, May 2013.
- [140] W. Chen and F. Chen, “Theoretical approaches to studying the single and simultaneous reactions in laminar flow-based membraneless fuel cells,” *J. Power Sources*, vol. 162, no. 2, pp. 1137–1146, Nov. 2006.
- [141] M.-H. Chang, F. Chen, and N.-S. Fang, “Analysis of membraneless fuel cell using laminar flow in a Y-shaped microchannel,” *J. Power Sources*, vol. 159, no. 2, pp. 810–816, Sep. 2006.

- [142] J. Lee, K. G. Lim, G. T. R. Palmore, and A. Tripathi, "Optimization of microfluidic fuel cells using transport principles.," *Anal. Chem.*, vol. 79, no. 19, pp. 7301–7307, Oct. 2007.
- [143] F. Chen, M.-H. Chang, and M.-K. Lin, "Analysis of membraneless formic acid microfuel cell using a planar microchannel," *Electrochim. Acta*, vol. 52, no. 7, pp. 2506–2514, Feb. 2007.
- [144] W. A. Braff and C. R. Buie, "Hydrogen Bromine Laminar Flow Electrochemical Cell for High Power and Efficiency Energy Storage Applications," *ECS Trans.*, vol. 33, no. 39, pp. 179–190, 2011.
- [145] I. Sprague and P. Dutta, "Role of the diffuse layer in acidic and alkaline fuel cells," *Electrochim. Acta*, vol. 56, no. 12, pp. 4518–4525, Apr. 2011.
- [146] J. Xuan, D. Y. C. Leung, M. K. H. Leung, H. Wang, and M. Ni, "Chaotic flow-based fuel cell built on counter-flow microfluidic network: Predicting the over-limiting current behavior," *J. Power Sources*, vol. 196, no. 22, pp. 9391–9397, Nov. 2011.
- [147] R. Hassanshahi, M. Fathipour, and M. Feali, "A New Structure for Improved Fuel Utilization and Performance of Microfluidic Fuel Cell," *Int. J. Adv. Renew. Energy Res.*, vol. 1, no. 11, pp. 605–610, 2012.
- [148] H. Zhang, J. Xuan, H. Xu, M. K. H. Leung, D. Y. C. Leung, L. Zhang, H. Wang, and L. Wang, "Enabling high-concentrated fuel operation of fuel cells with microfluidic principles: A feasibility study," *Appl. Energy*, pp. 1–7, Feb. 2013.
- [149] J. Xuan, H. Wang, D. Y. C. Leung, M. K. H. Leung, H. Xu, L. Zhang, and Y. Shen, "Theoretical Graetz–Damköhler modeling of an air-breathing microfluidic fuel cell," *J. Power Sources*, vol. 231, pp. 1–5, Jun. 2013.
- [150] H. Zhang, M. K. H. Leung, J. Xuan, H. Xu, L. Zhang, D. Y. C. Leung, and H. Wang, "Energy and exergy analysis of microfluidic fuel cell," *Int. J. Hydrogen Energy*, vol. 38, no. 15, pp. 6526–6536, May 2013.
- [151] J. Xuan, D. Y. C. Leung, H. Wang, M. K. H. Leung, B. Wang, and M. Ni, "Air-breathing membraneless laminar flow-based fuel cells: Do they breathe enough oxygen?," *Appl. Energy*, vol. 104, pp. 400–407, Apr. 2013.
- [152] R. A. García-Cuevas, I. Cervantes, L. G. Arriaga, and I. A. Diaz-Diaz, "Toward geometrical design improvement of membraneless fuel cells: Numerical study," *Int. J. Hydrogen Energy*, vol. 38, no. 34, pp. 14791–14800, Nov. 2013.
- [153] C. W. T. Yang, E. Ouellet, and E. T. Lagally, "Using inexpensive Jell-O chips for hands-on microfluidics education.," *Anal. Chem.*, vol. 82, no. 13, pp. 5408–14, Jul. 2010.

- [154] N. K. Thom, K. Yeung, M. B. Pillion, and S. T. Phillips, “‘Fluidic batteries’ as low-cost sources of power in paper-based microfluidic devices,” *Lab Chip*, no. 1, pp. 1768–1770, 2012.
- [155] J. Hur, D. Meng, and C. Kim, “Membraneless micro fuel cell chip enabled by self-pumping of fuel-oxidant mixture,” *Micro Electro Mech. Syst.* (...), pp. 168–171, 2010.
- [156] J. I. Hur, D. D. Meng, and C.-J. Kim, “Self-Pumping Membraneless Miniature Fuel Cell With an Air-Breathing Cathode,” *J. Microelectromechanical Syst.*, vol. 21, no. 2, pp. 476–483, Apr. 2012.
- [157] C. Garcia, B. Chang, and D. Johnson, “Round trip energy efficiency of NASA Glenn regenerative fuel cell system,” in *NHA Annual Hydrogen Conference*, 2006, no. NASA/TM—2006–214054, pp. NASA/TM—2006–214054.
- [158] F. Mitlitsky, B. Myers, and A. H. Weisberg, “Regenerative Fuel Cell Systems,” *Energy & Fuels*, vol. 400, no. 5, pp. 56–71, 1998.
- [159] Z. Yang, J. Zhang, M. C. W. Kintner-Meyer, X. Lu, D. Choi, J. P. Lemmon, and J. Liu, “Electrochemical energy storage for green grid.,” *Chem. Rev.*, vol. 111, no. 5, pp. 3577–3613, May 2011.
- [160] D. You, H. Zhang, and J. Chen, “A simple model for the vanadium redox battery,” *Electrochim. Acta*, vol. 54, no. 27, pp. 6827–6836, Nov. 2009.
- [161] D. R. Lide, *CRC Handbook of Chemistry and Physics*, 90th ed. Boca Raton: FL: CRC Press, 2010.
- [162] K. Kordesch, V. Hacker, J. Gsellmann, M. Cifrain, G. Faleschini, P. Enzinger, R. Fankhauser, M. Ortner, M. Muhr, and R. R. Aronson, “Alkaline fuel cells applications,” *J. Power Sources*, vol. 86, no. 1, pp. 162–165, 2000.
- [163] Z. Yuan, Y. Duan, H. Zhang, X. Li, H. Zhang, and I. Vankelecom, “Advanced porous membranes with ultra-high selectivity and stability for Vanadium flow battery,” *Energy Environ. Sci.*, pp. 22–24, 2015.
- [164] C. Xu, A. Faghri, X. Li, and T. Ward, “Methanol and water crossover in a passive liquid-feed direct methanol fuel cell,” *Int. J. Hydrogen Energy*, vol. 35, no. 4, pp. 1769–1777, Feb. 2010.
- [165] R. Byron Bird, W. E. Stewart, and E. N. Lightfoot, *Transport Phenomena*, 2nd ed. John Wiley & Sons Ltd, 2001.
- [166] D. Seguin, a Montillet, and J. Comiti, “Experimental characterisation of flow regimes in various porous media—I: Limit of laminar flow regime,” *Chem. Eng. Sci.*, vol. 53, no. 21, pp. 3751–3761, 1998.

- [167] D. Seguin, A. Montillet, and J. Comiti, "Experimental characterisation of flow regimes in various porous media—II: Transition to turbulent regime," *Chem. Eng. Sci.*, vol. 53, no. 22, pp. 3897–3909, 1998.
- [168] A. Einstein, *Investigations on the Theory of the Brownian Movement*, 2nd ed., vol. 17, no. 6. Dover Publications, 1956.
- [169] J. W. Lee, J. K. Hong, and E. Kjeang, "Electrochemical characteristics of vanadium redox reactions on porous carbon electrodes for microfluidic fuel cell applications," *Electrochim. Acta*, vol. 83, pp. 430–438, Nov. 2012.
- [170] D. S. Aaron, Q. Liu, Z. Tang, G. M. Grim, A. B. Papandrew, A. Turhan, T. a. Zawodzinski, and M. M. Mench, "Dramatic performance gains in vanadium redox flow batteries through modified cell architecture," *J. Power Sources*, vol. 206, pp. 450–453, May 2012.
- [171] Q. H. Liu, G. M. Grim, a. B. Papandrew, a. Turhan, T. a. Zawodzinski, and M. M. Mench, "High Performance Vanadium Redox Flow Batteries with Optimized Electrode Configuration and Membrane Selection," *J. Electrochem. Soc.*, vol. 159, no. 8, pp. A1246–A1252, 2012.
- [172] E. O. Barnes, X. Chen, P. Li, and R. G. Compton, "Voltammetry at porous electrodes: A theoretical study," *J. Electroanal. Chem.*, vol. 720–721, pp. 92–100, 2014.
- [173] K. R. Ward and R. G. Compton, "Quantifying the apparent 'Catalytic' effect of porous electrode surfaces," *J. Electroanal. Chem.*, vol. 724, pp. 43–47, 2014.
- [174] D. Menshykau, I. Streeter, and R. G. Compton, "Influence of electrode roughness on cyclic voltammetry," *J. Phys. Chem. C*, vol. 112, pp. 14428–14438, 2008.
- [175] D. Menshykau and R. G. Compton, "The influence of electrode porosity on diffusional cyclic voltammetry," *Electroanalysis*, vol. 20, pp. 2387–2394, 2008.
- [176] I. Streeter, G. G. Wildgoose, L. Shao, and R. G. Compton, "Cyclic voltammetry on electrode surfaces covered with porous layers: An analysis of electron transfer kinetics at single-walled carbon nanotube modified electrodes," *Sensors Actuators B Chem.*, vol. 133, no. 2, pp. 462–466, Aug. 2008.
- [177] H. Q. Zhu, Y. M. Zhang, L. Yue, W. S. Li, G. L. Li, D. Shu, and H. Y. Chen, "Graphite-carbon nanotube composite electrodes for all vanadium redox flow battery," *J. Power Sources*, vol. 184, no. 2, pp. 637–640, 2008.
- [178] W. Li, J. Liu, and C. Yan, "Multi-walled carbon nanotubes used as an electrode reaction catalyst for VO_2^+ for a vanadium redox flow battery," *Carbon N. Y.*, vol. 49, no. 11, pp. 3463–3470, 2011.

- [179] M. P. Manahan, Q. H. Liu, M. L. Gross, and M. M. Mench, "Carbon nanoporous layer for reaction location management and performance enhancement in all-vanadium redox flow batteries," *J. Power Sources*, vol. 222, pp. 498–502, Jan. 2013.
- [180] M.-A. Goulet and E. Kjeang, "Process of increasing energy conversion and electrochemical efficiency of a scaffold using a deposition material," p. US Patent Application 14/842,812, 2015.

Appendix A.

Microfluidic redox battery

Microfluidic redox battery

Jin Wook Lee,[†] Marc-Antoni Goulet[†] and Erik Kjeang*Cite this: *Lab Chip*, 2013, 13, 2504

Received 20th April 2013,

Accepted 8th May 2013

DOI: 10.1039/c3lc50499a

www.rsc.org/loc

A miniaturized microfluidic battery is proposed, which is the first membraneless redox battery demonstrated to date. This unique concept capitalizes on dual-pass flow-through porous electrodes combined with stratified, co-laminar flow to generate electrical power on-chip. The fluidic design is symmetric to allow for both charging and discharging operations in forward, reverse, and recirculation modes. The proof-of-concept device fabricated using low-cost materials integrated in a microfluidic chip is shown to produce competitive power levels when operated on a vanadium redox electrolyte. A complete charge/discharge cycle is performed to demonstrate its operation as a rechargeable battery, which is an important step towards providing sustainable power to lab-on-a-chip and microelectronic applications.

As an efficient and environmentally safe energy storage system, redox flow batteries (RFBs) have gained increased attention over the past years for utility grid-scale stationary applications. RFBs are electrochemical energy conversion and storage devices whose overall components are similar to those of polymer electrolyte membrane (PEM) fuel cells.¹ A key distinctive characteristic of RFBs compared to conventional battery technologies is the ability to separate power generation from energy storage.² The discharged electrolytes can be recharged *in situ*, or if necessary, entire storage tanks can be replaced with fresh electrolyte tanks for instant recharge. Vanadium RFBs, which were commercialized in the late 90s, demonstrated several advantages over Li-ion batteries in terms of long-term durability, high round-trip efficiency, and low capital cost.³ Miniaturization of RFBs is however a major challenge due to the stacked architecture with multiple functional layers.

In the realm of low-power, off-grid applications, wireless sensor networks are frequently employed to meet sensing demands from various customers, including military, industrial, commercial, and medical applications. The wireless sensors and signal transmitters

in remote areas typically require long-lasting, durable power sources with low maintenance cost.⁴ The main motivation for miniaturizing power supply units, such as fuel cells or batteries, includes its potential for high energy efficiency, robustness, and compactness. Therefore, lab-on-a-chip (LOC) and microfluidic cells have several advantages in this context, such as high surface-to-volume ratio, on-chip integration capability, and ease of miniaturization with relatively low material cost. Over the past decade, significant advances have been made on air-breathing⁵ and all-liquid^{6,7} microfluidic fuel cells that utilize microscale stratified flow control to eliminate the membrane and reduce cost.^{8,9} More recently, a paper-based microfluidic galvanic cell directly integrated with functional devices was reported by Thom *et al.*¹⁰ However, none of the microfluidic power sources presented to date are capable of *in situ* recharging.

The main goal of the present work is to develop and demonstrate a laminar flow-based microfluidic redox battery (MRB) that is fully capable of *in situ* recharging and cyclic operation. For this purpose, a novel symmetric architecture employing dual-pass flow-through porous electrodes¹¹ is proposed, fabricated, and benchmarked experimentally. Similar to miniaturized membraneless fuel cells,^{8,9} the proposed redox battery is designed to eliminate the membrane by utilizing predictable co-laminar flow at low Reynolds numbers with minimal convective mixing. Removal of the membrane also eludes membrane degradation issues and may potentially enhance durability. To the best of the authors' knowledge, this is the first membraneless MRB employing a single layer LOC architecture reported to date. Manufactured from inexpensive materials with scalable methods, the proposed battery can potentially be used as an integrated power source for low-power applications, such as micro-sensors and actuators and a host of other LOC functions.¹² In addition, if incorporated with an energy harvesting system or solar photovoltaic cell, the proposed device can be employed as a low-cost, durable power source for wireless sensor networks.

Graphical illustrations of the proposed MRB design are provided in Fig. 1. Geometrically symmetric in transversal and longitudinal directions, the present MRB device is designed to be

School of Mechatronic Systems Engineering, Simon Fraser University, 250-13450 102 Avenue, Surrey, BC, V3T 0A3, Canada. E-mail: ekjeang@sfu.ca; Fax: +1 (778) 782-7514; Tel: +1 (778) 782-8791

[†] JWL and MAG contributed equally to this work. EK conceived the concept and overall device architecture. JWL and MAG conducted the experiments and analyzed the data. JWL, MAG, and EK wrote the article.

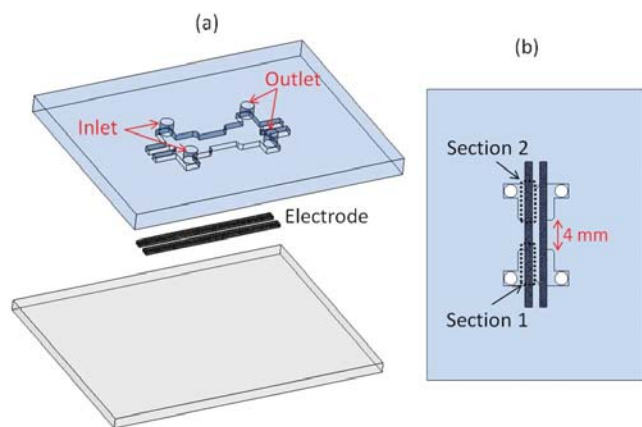


Fig. 1 A schematic representation of the proposed microfluidic redox battery with dual-pass flow-through porous electrodes: (a) an exploded view; and (b) the top view.

compatible with dual electrolyte flow in forward, reverse, and recirculation modes for maximum versatility. The layout consists of four fluid ports (two inlets and two outlets) and two porous electrodes positioned in parallel. The two inlets allow the input of anolyte and catholyte streams directed to flow through the first portion of the electrodes (Section 1 in Fig. 1(b)) where the electrochemical reactions take place. The two streams then enter the central channel where they turn downstream and flow in parallel in a symmetric, co-laminar fashion with minimal mixing between the streams. In Section 2, the two streams make another turn and flow in the opposite direction through the porous electrodes where the same electrochemical reactions take place. Finally, the fluid-containing products of the reactions exit the device through the two outlet ports. The MRB is interfaced electrically by two wires bonded to each end of the porous electrodes using a conductive epoxy. In the middle of the device, a 4 mm long wall is intended to seal the electrode tangentially to minimize unwanted bypass of fresh electrolyte.

The prototype MRB cells were fabricated by standard soft lithography in polydimethylsiloxane (PDMS).¹³ After insertion of the porous electrodes, the PDMS microchannel structure was sealed with a substrate layer (glass slide) using a corona treater (BD-20AC, Electro-Technic Products). The master was 150 μm high to ensure that the porous electrodes (180 μm thick) were slightly compressed for uniform flow distributions when assembled. For evaluation purposes, the MRB was operated on commonly employed vanadium redox electrolyte comprising of four different vanadium ions: $\text{V}^{2+}/\text{V}^{3+}$ and $\text{VO}^{2+}/\text{VO}_2^+$, denoted here as V(II), V(III), V(IV), and V(V), respectively.⁷ The theoretical standard cell potential is 1.246 V and can be increased up to 1.5 V depending on the state of charge. 1.7 M of vanadium redox electrolyte solutions were prepared from a stock electrolyte in 4 M sulphuric acid base according to a previously described procedure.⁷ Carbon nanofoam (Type I, MarkeTech) was selected as the porous electrodes for the MRB due to its rapid electrochemical kinetics,¹⁴ high porosity, extremely high surface area, and ultrafine pore sizes (less than 50 nm).¹⁵

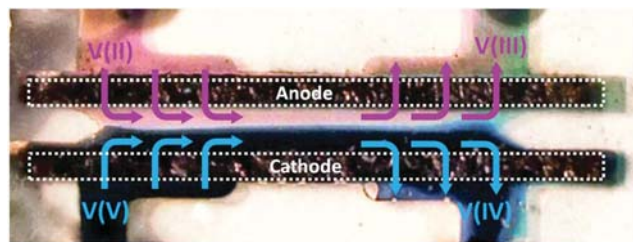


Fig. 2 An annotated image of a microfluidic redox battery operating in discharge mode at $10 \mu\text{L min}^{-1}$ flow rate. The dotted lines indicate the positions of the porous electrodes.

First, a high state-of-charge (SOC) anolyte (93% V(II)) and catholyte (85% V(V)) supplied in a single pass forward mode by a dual syringe pump were used to benchmark the MRB discharge performance with respect to previously reported microfluidic fuel cell devices.¹⁴ An annotated image of the actual device operated in discharge mode is provided in Fig. 2, where the distinct colours of the different reactants and products can be observed. The measured polarization and power density curves of the MRB at a flow rate of $10 \mu\text{L min}^{-1}$ are presented in Fig. 3. The open circuit cell voltage was 1.5 V. Notably, no abrupt potential drops were observed in the activation overpotential region, in contrast to cells with regular carbon paper electrodes known to exhibit more severe activation loss characteristics.¹⁶ This favourable observation, which is particularly encouraging for battery operation at high voltage efficiency, is a consequence of the rapid electrochemical kinetics of the vanadium redox reactions on the carbon nanofoam electrode material.¹⁴ The overall discharge performance achieved by the MRB, indicated by current densities up to 0.6 A cm^{-2} and a peak power density in excess of 0.3 W cm^{-2} , is on the same order of magnitude as recently reported, state-of-the-art miniaturized fuel cells.^{7,14} The corresponding peak power density is 3 W cm^{-3} , if normalized by the single electrode volume ($1 \text{ cm} \times 0.015 \text{ cm} \times 0.1 \text{ cm}$).

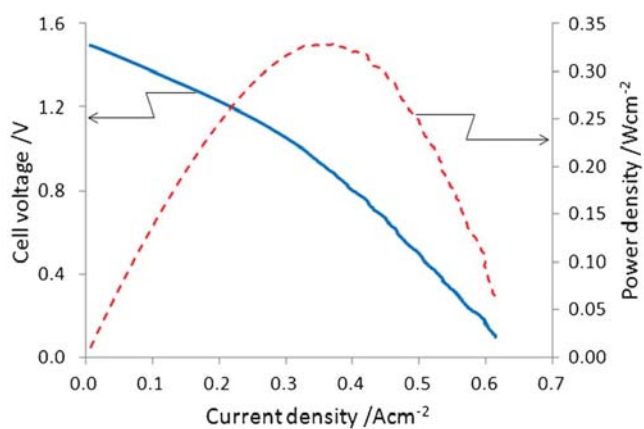


Fig. 3 The discharging performance of the microfluidic redox battery at $10 \mu\text{L min}^{-1}$ flow rate. A linear potential sweep from 1.5 to 0.1 V at 3 mV s^{-1} was performed using a potentiostat (Reference 3000, Gamry Instruments). The current densities and power densities reported here were normalized by the net flow area normal to the main flow direction, 0.015 cm^2 ($1 \text{ cm} \times 0.015 \text{ cm}$).

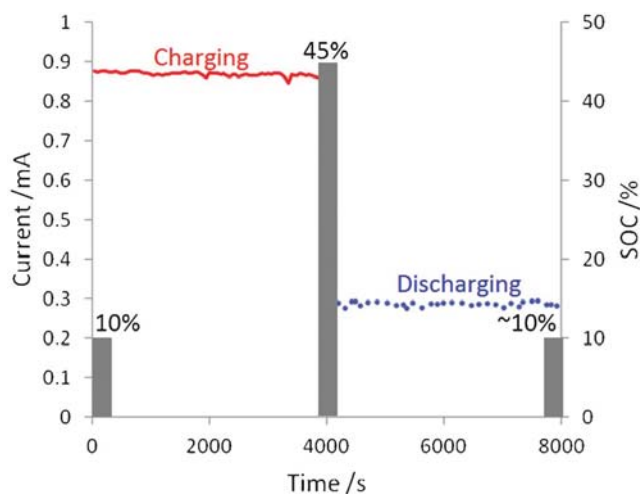


Fig. 4 Proof-of-concept operation of the microfluidic redox battery in a complete charge-discharge cycle. The current during charging at $1 \mu\text{L min}^{-1}$ and 1.7 V and discharging at $1 \mu\text{L min}^{-1}$ and 1.0 V is shown. The bars indicate the state of charge of V(v) measured at the initial, post-charge, and post-discharge conditions.

The *in situ* charging mode operation was conducted in a single pass forward mode using low SOC electrolytes (10%) at a low flow rate of $1 \mu\text{L min}^{-1}$. The flow rates at the inlets were controlled by a syringe pump applying a positive pressure, while the two outlet flow rates were set by a negative pressure from another syringe pump operating simultaneously. A constant potential of 1.7 V was applied by a potentiostat in order to reach the highest charging overpotential possible, while avoiding side reactions and hydrogen evolution that may occur at high cell potentials. As shown in Fig. 4, a steady-state charging current of $0.85 \pm 0.02 \text{ mA}$ was reached. It is worth noting that the characteristic charging curves of the MRB under single pass operation at a fixed cell potential are essentially flat, in contrast to the unsteady curves obtained under electrolyte recirculation (not shown here). The product electrolytes of the charging process were collected in separate syringes and their SOC was measured to be roughly 35% for V(II) and 45% for V(V). The slight asymmetry between the charging of V(II) and V(V) can be attributed to asymmetric crossover of the reactant species, but may also be due to side reactions and/or the uncertainty inherent to the potentiometric SOC measurements. Although only a moderate SOC was reached for this particular cycle, higher SOC levels up to 70% were observed at other operating conditions with this device. Upon completion of a single pass of charging, the flow was reversed to operate the device again in discharge mode to verify the feasibility of cyclic battery operation. An operating point of 1.0 V at $1 \mu\text{L min}^{-1}$, which resulted in a flat discharge profile with an average current of $0.29 \pm 0.02 \text{ mA}$, also shown in Fig. 4, was observed to produce a SOC as close as possible to the initial 10%. The overall round-trip energy efficiency of the obtained *in situ* charge-discharge cycle was estimated by calculating the ratio of the energy furnished by the battery during the discharge to the energy supplied during the charge. For this particular run, the energy efficiency was found to be around 20%. By comparison, the

typical round-trip efficiency of a hydrogen electrolyzer/fuel cell combination is also $\sim 20\%$.¹⁷ As a proof-of-concept, the present MRB device performs reasonably well, although higher round-trip efficiencies exceeding 30% are expected at lower power operating conditions and/or with electrolyte recirculation. Optimization of the battery design and flow management with respect to the operating voltage and power density will be the subject of a future study.

Conclusions

For the first time, a membraneless microfluidic redox battery was demonstrated. Prototypes of the proposed microfluidic battery architecture with unique dual-pass flow-through porous electrodes were designed, fabricated, and tested experimentally. The discharging power density of the battery was found to be equivalent to previously developed microfluidic fuel cells, with a peak power density of 0.3 W cm^{-2} . In addition, the battery device successfully demonstrated *in situ* charging of vanadium redox electrolytes from 10 to 45% state of charge, followed by the discharge of the same electrolytes back to the initial state of charge to complete a full charge-discharge cycle. In the present study, the device demonstrated that the concept of laminar flow-based microfluidic fuel cells can be extended to rechargeable and therefore reusable microfluidic redox batteries, which is a significant breakthrough towards providing sustainable power to lab-on-a-chip applications. The overall battery architecture is compatible with most liquid phase redox chemistries and can facilitate integration with biological and physiological systems for a wide range of on-chip utilities.

Acknowledgements

Funding for this research provided by the Natural Sciences and Engineering Research Council of Canada, Western Economic Diversification Canada, Canada Foundation for Innovation, British Columbia Knowledge Development Fund, and Simon Fraser University (SFU) is highly appreciated. We also acknowledge Mr. Andy Klassen at Prudent Energy for experimental support and advice.

References

- 1 J. Larminie and A. Dicks, *Fuel Cell Systems Explained*, 2003, John Wiley & Sons Inc., Hoboken, 2nd edn, p. 5.
- 2 A. Z. Weber, M. M. Mench, J. P. Meyers, P. N. Ross, J. T. Gostick and Q. H. Liu, *J. Appl. Electrochem.*, 2011, **41**, 1137.
- 3 M. Schreiber, M. Harrer, A. Whitehead, H. Bucsich, M. Dragschitz, E. Seifert and P. Tymciw, *J. Power Sources*, 2012, **206**, 483.
- 4 S. Petersen, P. Doyle, S. Vatland, C. S. Aasland, T. M. Andersen and D. Sjong, *12th IEEE International Conference on Emerging Technologies and Factory Automation*, 2007, 1–3, 219.
- 5 R. S. Jayashree, L. Gancs, E. R. Choban, A. Primak, D. Natarajan, L. J. Markoski and P. J. A. Kenis, *J. Am. Chem. Soc.*, 2005, **127**, 16758.
- 6 R. Ferrigno, A. D. Stroock, T. D. Clark, M. Mayer and G. M. Whitesides, *J. Am. Chem. Soc.*, 2002, **124**, 12930.

- 7 E. Kjeang, R. Michel, D. A. Harrington, N. Djilali and D. Sinton, *J. Am. Chem. Soc.*, 2008, **130**, 4000.
- 8 E. Kjeang, N. Djilali and D. Sinton, *J. Power Sources*, 2009, **186**, 353.
- 9 S. A. M. Shaegh, N. T. Nguyen and S. H. Chan, *Int. J. Hydrogen Energy*, 2011, **36**, 5675.
- 10 N. K. Thom, K. Yeung, M. B. Pillion and S. T. Phillips, *Lab Chip*, 2012, **12**, 1768.
- 11 E. Kjeang, D. Sinton and N. Djilali, *US Patent Application* 20090092882, 2009.
- 12 S. Pennathur, J. C. T. Eijkel and A. van den Berg, *Lab Chip*, 2007, **7**, 1234.
- 13 J. W. Lee and E. Kjeang, *Int. J. Hydrogen Energy*, 2012, **37**, 9359.
- 14 J. W. Lee and E. Kjeang, *J. Power Sources*, 2013, (under review).
- 15 R. W. Pekala, J. C. Farmer, C. T. Alviso, T. D. Tran, S. T. Mayer, J. M. Miller and B. Dunn, *J. Non-Cryst. Solids*, 1998, **225**, 74.
- 16 J. W. Lee, J. K. Hong and E. Kjeang, *Electrochim. Acta*, 2012, **83**, 430.
- 17 A. Yilanci, I. Dincer and H. K. Ozturk, *Prog. Energy Combust. Sci.*, 2009, **35**, 231.

Appendix B.

Reactant recirculation in electrochemical co-laminar flow cells



Reactant recirculation in electrochemical co-laminar flow cells



Marc-Antoni Goulet, Erik Kjeang*

School of Mechatronic Systems Engineering, Simon Fraser University, 250-13450 102 Avenue, Surrey, BC, V3T 0A3, Canada

ARTICLE INFO

Article history:

Received 15 December 2013

Received in revised form 14 March 2014

Accepted 14 March 2014

Available online 28 March 2014

Keywords:

co-laminar flow cell

microfluidic

laminar

fuel cell

flow battery

ABSTRACT

Co-laminar electrochemical cells utilize hydrodynamic engineering rather than a physical separator to prevent mixing of reactants. Commonly known as microfluidic fuel cells and batteries, these cells are based on stratified laminar flow of reactants in a microfluidic channel. The objective of the present work is to evaluate the feasibility and effectiveness of reactant recirculation in co-laminar flow cells with flow-through porous electrodes. Two representative device architectures are fabricated with separate outlets for reactant recirculation in Y-junction and dual-pass configurations. It is found that crossover at the electrodes reduces the open circuit potential of both cells and serves as a useful diagnostic method for assessing the degree of crossover at the outlets. Outlet concentration is monitored at a range of flow rates and indicates that asymmetric splitting of the co-laminar interface can lead to a constant 2% loss of state of charge, while the loss due to diffusion ranges from 0–40%. The dual-pass cell is shown to have greater diffusive loss due to deceleration at the splitting junction but also demonstrates better performance due to its higher convective velocity through the porous electrodes. These effects are observed during a series of discharge operations with recirculating reactants, in which the dual-pass cell results in greater reactant utilization despite its higher crossover rates. Overall, the present results demonstrate reactant recirculation as a useful strategy to combine high reactant utilization and high power density in membraneless co-laminar flow cells.

© 2014 Elsevier Ltd. All rights reserved.

1. Introduction

Among the possibilities for electrochemical energy conversion and storage, fuel cells and flow batteries are advantageous particularly for high power applications due to their ability to admit more reactants upon demand [1]. Traditionally these cells have required some form of physical barrier such as porous separators or ionically conductive membranes to separate the reactants and prevent a mixed potential [2]. Co-laminar flow cells on the other hand, are those which utilize hydrodynamic engineering and the properties of laminar flow to prevent the mixing of individual streams of liquid.

Fluid dynamics is characterized as laminar when the ratio of inertial to viscous forces, otherwise known as the Reynolds number, is sufficiently small [3]. In this flow regime, the absence of turbulence or perpendicular convection allows layered streams to flow side by side with cross-stream mixing occurring strictly through diffusion. This phenomenon has been used for applications ranging from patterning [4], T-sensors [5], subcellular drug delivery [6], and other lab-on-chip applications [7]; but was also proposed as a way

of keeping reactants separate in fuel cells and thereby eliminating the ion-conducting polymer membrane [8,9]. In a pioneering work, Ferrigno et al. introduced two parallel streams of vanadium redox reactants into a micro-channel containing wall deposited anode and cathode electrodes. Although this membraneless cell demonstrated a reasonable power output of $38 \text{ mW} \cdot \text{cm}^{-2}$, the boundary layer depletion at the planar electrodes required very high flow rates which translated into low fuel utilization of only around 0.1%. Since then, many studies have explored various reactant combinations or cell architectures to improve the performance of these microfluidic co-laminar flow fuel cells. Among these, the introduction of flow-through porous electrodes in particular, by Kjeang et al. in 2008, resulted in considerably greater power output and fuel utilization. It was shown that fuel utilization up to 100% was achievable albeit at much lower flow rates [10]. Other notable highlights in the field of co-laminar flow cells has been the development by Jayashree et al. of air-breathing cells for which an ion-conducting blank electrolyte maintains the co-laminar interface and prevents the anolyte from reaching the cathode [11]. Apart from the type of electrodes used, the most critical attribute for co-laminar flow cell design is the geometry of the cell. Even in the absence of convection perpendicular to the flow, reactant mixing and crossover still occurs due to diffusion of species. Cells must be designed so that the residence time for the reactant species at the co-laminar interface

* Corresponding author. Tel.: +1 778 782 8791; fax: +1 778 782 7514.
E-mail address: ekjeang@sfu.ca (E. Kjeang).

is shorter than their diffusion time towards the opposite electrode. A comprehensive review of these concepts and the early developments in microfluidic fuel cells was published in 2009 by Kjeang et al. [12]. Since then the field has expanded to include closely related rechargeable flow batteries [13,14], new electrode materials [15–17], and the reintroduction of porous separators among other developments [18,19].

For practical power output, most conventional fuel cells typically operate at high flow rates and recirculate the unused reactants until depletion. In addition, individual cells are often stacked in series or parallel to reach higher power outputs. Although stacking traditionally involves fabricating cells which can be placed back-to-back to minimize space requirements and ohmic losses [14,20,21], planar multiplexing of monolithic cells [22,23] may also prove useful for lab-on-chip applications. Without any type of membrane or porous separator, fuel cells based on co-laminar flow would be expected to be more prone to reactant crossover than their conventional counterparts, thereby limiting the potential for efficient fuel recirculation. The vast majority of studies in this field have explored only single pass discharge operation and therefore little quantitative data is available in the literature for understanding the breadth of these limitations. The first study to attempt recirculation of depleted reactants was performed by Saloum et al. in 2011, in which a second co-laminar flow fuel cell was placed downstream from the first one [22]. Splitting of the reactant streams without crossover was achieved through the use of a third stream of blank electrolyte. Although this fuel cell pair was able to produce nearly twice the power output at high flow rates when both cells were connected in parallel, the change in concentration of the reactants was not measured and therefore it is unknown to what extent the reactants were diluted by the use of a blank electrolyte. A recent study published by our group proposed a symmetric dual-pass design with flow-through electrodes for reversible charging and discharging of vanadium reactants [13]. In discharge mode the cell performance was equivalent to other flow-through fuel cell designs with the same reactants [10,24], but the cell possessed the added functionality of cyclic operation as a secondary flow battery, and demonstrated for the first time that redox flow batteries can be designed and operated without a membrane. The cell achieved 20% full cycle energy efficiency and was named the microfluidic redox battery (MRB) due to its similarities with conventional vanadium redox flow batteries. Another more recent study by Braff et al. explored the idea of fuel regeneration with a co-laminar hydrogen-bromine flow battery with a gaseous anode. The cell demonstrated the highest power density of any co-laminar cell published to date in both charging and discharging operation with a purported cycle efficiency of up to 91% [14]. It is however not clear whether the cell was actually operated in a full cycle, or whether the voltage efficiencies were merely inferred from independent charge and discharge curves. More comprehensive experimentation would be required to assess whether cyclic operation is feasible for this device. As a liquid-gaseous system, any analysis of fuel recirculation and regeneration would be considerably different from a liquid-liquid system such as the all-vanadium battery.

In either case, reactant recirculation is likely to be essential for the practical application of co-laminar flow cell technology for electrochemical energy conversion and storage. Unless very high single pass fuel utilization becomes possible with simultaneously high power output, it will become necessary for co-laminar flow cells to minimize the waste of unused reactants through recirculation in order to maximize overall energy efficiency. The objective of the present work is therefore to assess the capability and functionality of co-laminar flow cell operation in recirculation mode, and provide guidelines for future developments of practical cell design and operational strategies.

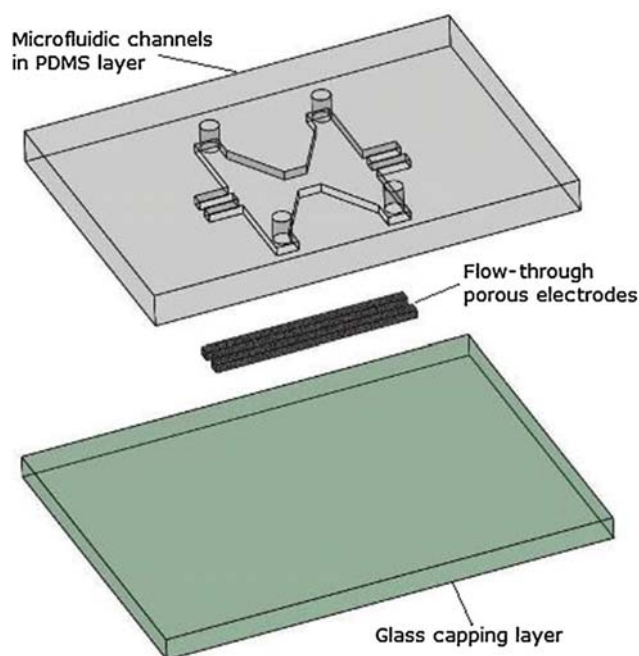


Fig. 1. Co-laminar flow cell assembly and materials.

2. Experimental

2.1. Device fabrication

The microfluidic channels for the co-laminar flow cells used in this study are fabricated by soft lithography of polydimethylsiloxane (PDMS) from a photoresist template. An illustrative example of the cell configuration is provided in Fig. 1 with more detail on the fabrication procedure to be found in earlier literature published by our group [10,25,26]. Unlike previous microfluidic fuel cell designs however, the present cells are designed to have two inlets and two separate outlets for collecting unused reactants. The electrodes are cut from carbon nanof foam (Type I, MarkeTech) and placed into PDMS channels of the same width. This layer is then permanently bonded to a glass substrate via plasma treatment of both surfaces (BD-20AC, Electro-Technic Products). The thickness of the electrodes exceeds the channel height by about 20 μm in order to facilitate slight electrode compression during cell bonding, thereby preventing unwanted bypass of reactants. Holes are punched and tubing inserted to provide access to the inlets and outlets. Electrical contact between the wires and electrodes is achieved through the use of silver conductive epoxy (MG Chemicals). In both co-laminar flow cell architectures presented in this study the active electrode dimensions are 10 mm long, 1 mm wide, and 0.18 mm thick. The channel width between electrodes is 1 mm, whereas the height is slightly lower than the electrode height at 0.16 mm in order to lightly compress the electrodes and prevent bypass of reactants. As such the active volume of each electrode is considered to be 1.6 mm^3 with the total volume of the essential electrochemical chamber, including both electrodes and the center channel, to be 4.8 mm^3 . With three-dimensional flow-through electrodes, there is some debate as to whether the projected electrode area or the area cross-sectional to the reactant flow should be used for normalization. For these cells, the projected active area of one electrode is therefore 10 mm^2 , whereas the cross-sectional area of the electrode is 1.8 mm^2 . Due to the ambiguity, the measured current values are reported without normalization.

2.2. Reactants

The fuel and oxidant used for experimental characterization of the co-laminar flow cells are the same redox couples used in the original vanadium redox flow battery first developed by Skyllas-Kazacos et al. [27]. In this paper, we refer to V^{2+}/V^{3+} and VO^{2+}/VO_2^+ by their respective oxidation states V(II)/V(III) and V(IV)/V(V), respectively. These redox couples undergo the following anodic and cathodic reactions at 298 K [22]:



The fuel and oxidant electrolytes are prepared from a commercial stock solution of 1.7 M V(III)/V(IV) electrolyte in 4 M sulfuric acid by charging the solution with a conventional flow battery. It should be noted that the highly acidic conditions increase the equilibrium potential of the V(IV)/V(V) reaction beyond that predicted for pH=0 by Eq. 2. The concentrations used in this study are equivalent to 50% or 90% of the V(II) and V(V) state of charge for each half-cell, corresponding to 0.85 M and 1.53 M respectively. The relatively high concentration of vanadium leads to a significant variability in the sulfuric acid concentration with respect to the state of charge of V(V). For this reason, the Nernst equation becomes an implicit function which requires knowledge of the pH of the solution for determining the concentration of the V(IV)/V(V) species. Such high concentrations of sulfuric acid make pH measurements both difficult and less meaningful, and it is unknown whether the same Nernst relation is truly applicable. All V(IV)/V(V) concentrations are therefore measured at open circuit potential with a saturated calomel reference electrode (SCE, Fisher Scientific) and compared to previously measured titration curves. These curves (not shown) are obtained via permanganate titration with 0.01 M $KMnO_4$ similarly to the procedure described by Skyllas-Kazacos et al. [28].

2.3. Cell characterization

In all cases the two vanadium electrolytes are injected into the inlets by a dual syringe pump and removed by a second unit of the same pump. The two pumps (Harvard Apparatus) are operated in unison at flow rates ranging from 1 to 300 $\mu\text{L}\cdot\text{min}^{-1}$. The concentrations at the outlets for each experimental condition are measured via SCE by interrupting the experiment and severing the tubing without disturbing the contents. Due to the uncertainty in this measurement, the concentration loss experiments are repeated three times with the error bars in the associated graphs indicating two standard deviations from the average. All polarization measurements are made with a potentiostat (Reference 3000, Gamry) operating at steady state potentiostatic conditions. With equal dimensions, the two cell architectures have very similar ohmic resistance (not shown) as measured by electrochemical impedance spectroscopy (EIS) with the same potentiostat. The polarization and performance data is therefore not corrected for ohmic effects to simplify the discussion of operating point in Section 3.2.

3. Results and discussion

3.1. Reactant crossover

In contrast to single pass operation, fuel recirculation requires the anolyte and catholyte reactant streams to be harvested separately by splitting the streams at the co-laminar interface. The most direct way to understand the limits for fuel recirculation in co-laminar flow cells is to measure the change in concentration between the inlets and outlets at open circuit and other

polarization conditions, which captures the combination of electrochemical reactant depletion and reactant crossover or mixing between the two streams. Quantifying the crossover in this way is intended to shed light on which architectural and operating parameters can be modified to achieve the highest device efficiency. In this section, two categories of device architecture are compared at the same operating conditions. The first of these is the classic Y-junction (or T-junction) cell depicted in Fig. 2-a) in which the reactant streams flow through the porous electrodes and then side by side down the center channel until they split into two outlet streams outside the electrochemical chamber. The second architecture is the novel dual-pass architecture first published by our group in 2013 [13], and depicted in Fig. 2-c). A previously unpublished 1st generation of this type of cell is also depicted in Fig. 2-b). In this type of cell architecture, the splitting of the streams occurs within the electrochemical chamber, sending each stream through their respective electrodes for a second pass before they exit via the separate outlets. This dual-pass concept was developed to enhance mass transport through the electrodes and to enable the symmetric cell to be operated in both flow directions. It should be noted that all architectures being considered utilize the same flow-through porous electrodes to maximize the utilization and productivity of the three-dimensional surface area inside the porous electrodes [29].

3.1.1. Y-junction cells

As with traditional fuel cells and flow batteries, co-laminar flow cells are typically designed with certain operating conditions in mind. In the case of co-laminar flow cells however, the reduction in system complexity and cost engendered by the absence of a membrane leads to added constraints on the flow rates. Assuming that the cross-sectional area of the microchannel and the flow rates are appropriate to maintain the laminar flow necessary to eliminate convective crossover of reactants, it is also desirable to minimize the diffusive crossover of reactants. If the diffusive crossover is severe, a mixed potential will form at the electrodes leading to a loss in cell performance. As with other electrochemical cells, the open circuit potential is a direct measurement of this type of reactant crossover at the electrodes. In addition, excess reactant diffusion will lead to reactant mixing at the splitting point of the streams thereby decreasing the concentration of unused reactants at the outlets and decreasing the efficiency of fuel recirculation. These two consequences of cross-stream diffusion are related but not directly proportional to each other for the Y-junction cell (Fig. 2-a). Notably, cross-stream diffusion at the co-laminar interface is a precursor for reactant crossover and increases downstream, though only a portion of the species that diffuse across the interface will ultimately reach the opposite electrode. In other words, diffusive concentration loss measured at the outlets will dominate over the rate of crossover indicated by the crossover sensitive OCV measurement.

The data presented in Fig. 3 illustrates the effect of the flow rate on the open circuit potential (OCV) of the Y-junction cell. At flow rates of 10 $\mu\text{L}\cdot\text{min}^{-1}$ and above, the OCV is constant and equal to 1.529 V, which coincides with the potential difference of the two reactant half-cells when measured independently via reference electrode and therefore indicates no crossover of reactants. At flow rates below this value, the OCV drops slightly, suggesting the onset of reactant crossover at the electrodes. For the purposes of reactant recirculation, it is desirable to avoid low flow rates for which reactant crossover can be detected. Measuring the concentration of the reactants at the outlets during this OCV operation can reveal more details about this trend.

The data presented in Fig. 4 shows the maximum loss in concentration due to crossover at the outlet junction. With an initial state of charge around 90% for each reactant, the loss in concentration varies from approximately 2% at 100 and 300 $\mu\text{L}\cdot\text{min}^{-1}$

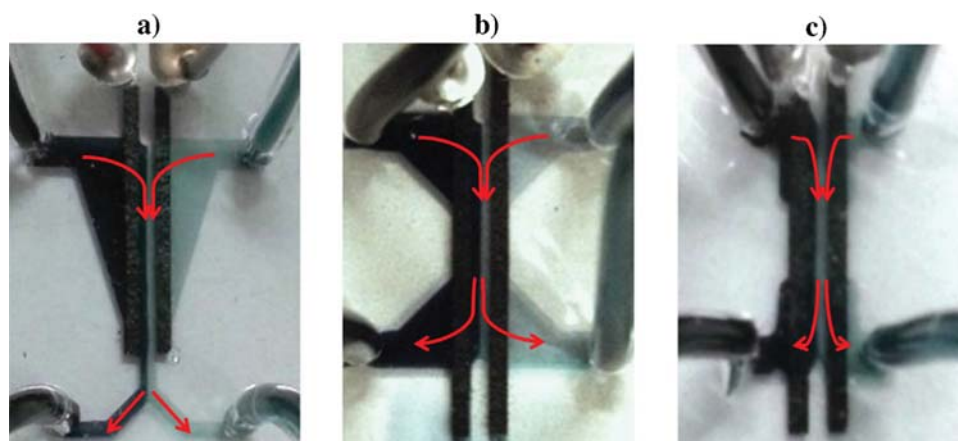


Fig. 2. Real-time annotated images of co-laminar flow cells at OCV with low concentration reactants flowing downwards at $100 \mu\text{L}\cdot\text{min}^{-1}$. In all cases there is no visible diffusion between the V(V) on the left and the V(II) on the right. a) Y-junction cell, b) 1st generation dual-pass cell, and c) 2nd generation dual-pass cell or microfluidic redox battery (MRB).

to nearly 30% at $1 \mu\text{L}\cdot\text{min}^{-1}$. The ‘maximum loss’ reported here represents the most severely affected half-cell and its associated drop in reactant concentration. The reason for this analysis is to adequately capture both sources of crossover losses: asymmetric splitting which leads to a proportion of one stream exiting via the opposite outlet and purely diffusive crossover which occurs gradually along the length of the channel. Splitting a co-laminar

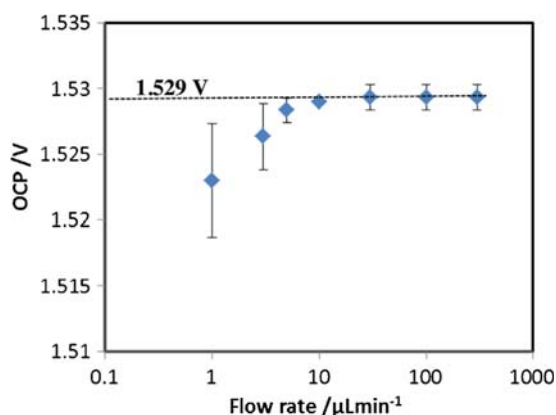


Fig. 3. Open circuit potential between Y-junction cell electrodes measured at a range of flow rates with high concentration reactants totalling 1.529 V in combined initial equilibrium potential.

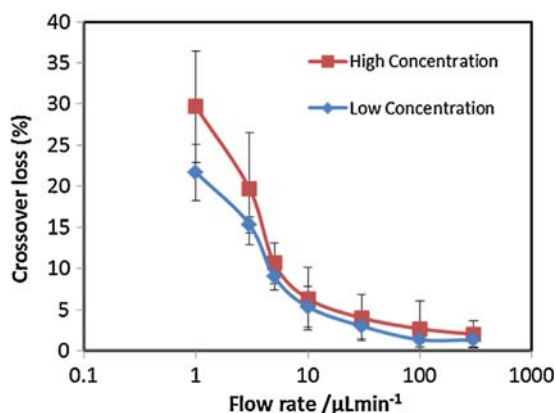


Fig. 4. Maximum loss in concentration as a function of flow rate for high and low concentration (initial SOC = 90% and 50%) reactants flowing through the Y-junction cell at open circuit conditions.

interface and extracting each stream separately would ideally be a completely symmetric process, however achieving this ideal in practice is quite challenging due to differences in syringe volume, device imperfections, pulsation, and other potential sources of variability in flow rates at each outlet. In the present case, it appears that the crossover loss at flow rates above $30 \mu\text{L}\cdot\text{min}^{-1}$ approaches a final constant value of around 2%. This indicates that the loss is due to asymmetric splitting of the streams rather than a diffusive effect which is dependent on the flow rate. Nevertheless, the diffusive mixing obtained at the outlets becomes more noticeable at flow rates below $30 \mu\text{L}\cdot\text{min}^{-1}$ and is shown to precede the mixed potential detected at the electrodes.

The same type of experiment is repeated with lower concentration reactants with an initial state of charge of 50%. The maximum crossover loss for these tests is also plotted in Fig. 4. As expected, the loss is generally only 2/3–3/4 of the loss for the high concentration reactants due to the lower charge gradient and crossover rate. It should be noted that the measurement is not a direct detection of species that have crossed over, but of a reduction in state of charge of the reactants. At first glance, it may be expected that with an initial state of charge ratio of 5/9 between the low and high concentration, the outlet loss at these concentrations would follow the same ratio if we neglect the concentration gradient effect. This notion is oversimplified however, since the reactant species have four possible oxidation states. For example, one V(II) ion which crosses to the V(V) outlet will create three new V(IV) ions and consume two V(V) ions in the process. With these added crossover contributions, the ratio for the loss is expected to be 15/19. Although the present data are insufficient to capture such precise relationships due to the large experimental error inherent in the concentration measurements, the overall trend is in the right direction and lends extra credence to the methodology being used.

3.1.2. Dual-pass cells

The dual-pass cell design depicted in Fig. 2-b) is a previously unpublished and earlier incarnation of the microfluidic redox battery in Fig. 2-c) [13]. It is presented here alongside the 2nd generation design for added clarity and to highlight an important architectural evolution which is applicable to all co-laminar flow cells. Performing the same open circuit potential analysis as described above reveals important design principles for co-laminar flow cells in general and fundamental differences between the Y-junction and dual-pass architectures. Starting with the same high concentration initial reactants, the open circuit potential for each cell is presented in Fig. 5. Not so clearly visible, one of the more

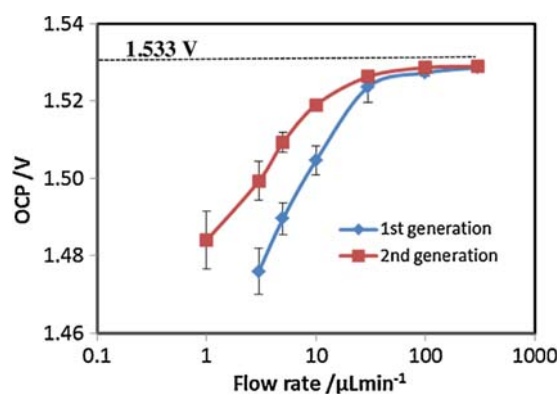


Fig. 5. Open circuit potential between electrodes for both generations of dual-pass architecture with high concentration reactants totalling 1.533 V in combined initial equilibrium potential.

important differences between the dual-pass and Y-junction architectures is the presence of a mixed potential at all flow rates for the dual-pass cells. The OCV plateau for both the 1st and 2nd generation dual-pass cells lies around 1.530 V, whereas the potential difference between the two reactant half-cells for these tests was around 1.533 V. Since the splitting of the co-laminar interface occurs within the electrochemical chamber before the second pass through the electrodes, the same asymmetric or imperfect splitting observed with the Y-junction inevitably causes some degree of reactant crossover which unavoidably reaches the downstream section of the electrodes. Although the mixed potential has minimal effect on device performance, it reduces the practical operating range of the cell.

The more obvious lesson to be gleaned from the data in Fig. 5 is that the cell geometry significantly affects the degree of diffusive crossover. Although both generations of dual-pass cells seem to have the same asymmetric loss at high flow rates, the OCV of the 1st generation drops much faster as the flow rate decreases. As explained previously, cross-stream diffusion is minimized by decreasing the residence time of the reactants in the co-laminar configuration. One way of facilitating reduced residence time is to create a more streamlined cell design that eliminates stagnation points in the flow field and provides more uniform flow distribution through the porous electrodes. The narrower design of the 2nd generation cell was developed with this design philosophy supported by computational fluid dynamics. The data in Fig. 5 shows that cross-stream diffusion has been greatly reduced with the streamlined cell design. This type of design improvement is applicable to many co-laminar flow cell architectures and should be considered as the first step towards minimizing diffusive crossover. Although fuel recirculation was viable with the 1st generation design, the degree of crossover loss was too large to perform a complete charge-discharge cycle with reasonable efficiency. For this reason, the remainder of the analysis will compare the Y-junction architecture strictly with the improved 2nd generation dual-pass architecture.

The same concentration loss experiment conducted on the Y-junction is repeated on the 2nd generation dual-pass architecture. Fig. 6 shows the maximum loss in state of charge as a function of flow rate, revealing the same trend but with generally greater loss. From a purely fluid dynamics point of view, this indicates that the dual-pass configuration ultimately has more cross-stream diffusion than the Y-junction which will reduce the overall efficiency of fuel recirculation. This is a direct consequence of the velocity distribution in the central channel prior to the splitting of the co-laminar interface. The narrowing Y-junction accelerates the convective velocity of the reactants before the split, whereas

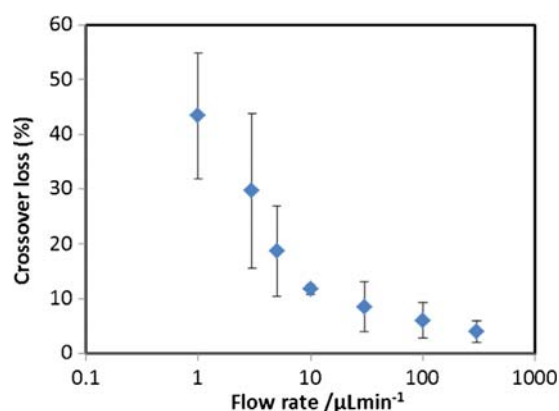


Fig. 6. Maximum loss in concentration as a function of flow rate for high concentration (initial SOC = 90%) reactants flowing through the 2nd generation dual-pass cell at open circuit conditions.

the widening dual-pass design decelerates the velocity of the reactants and therefore increases cross-stream diffusion before the split occurs. As previously shown with the OCV measurements however, this phenomenon can potentially be mitigated through computational fluid dynamics supported cell design. An unexpected benefit of the dual-pass cell is the more direct correlation between the OCV measurement and crossover loss. Unlike the Y-junction where the OCV and crossover are uncorrelated at high flow rates, any crossover in the dual-pass cell happens before the second pass through the electrodes and therefore engenders an associated decrease in OCV. As a simple measurement, the OCV can therefore be used as a quick diagnostic method for experimentally benchmarking crossover in new dual-pass cell designs.

3.2. Performance and operating point

The most common method of evaluating the performance of fuel cells is the ubiquitous polarization curve. The polarization curves presented in Fig. 7 show the steady state discharge currents at a range of potentials from OCV to 0.1 V for both cell architectures at the same flow rates considered in the crossover analysis. Both graphs show a transition from mass transport limited polarization behavior at 1 $\mu\text{L}\cdot\text{min}^{-1}$ to mostly ohmic limited behavior at 300 $\mu\text{L}\cdot\text{min}^{-1}$. At all flow rates, the dual-pass cell outperforms the Y-junction cell by more than 20%. The primary reason for this performance improvement is the increased convective velocity through the electrodes, resulting in reduced mass transport losses and increased current density. By effectively dividing the electrodes into two equal segments (one for each pass), the same flow rates generate twice as high convective velocity inside the electrodes than for the conventional single-pass cell design, i.e., the Y-junction cell. This can be confirmed qualitatively by comparing the polarization curves at high flow rates. The difference between the 100 and 300 $\mu\text{L}\cdot\text{min}^{-1}$ curves for the dual-pass cell is minimal, indicating that the electrodes are nearly saturated with reactants and therefore ohmic limited at 100 $\mu\text{L}\cdot\text{min}^{-1}$. In the case of the Y-junction however, there is still a clear mass transport loss at 100 $\mu\text{L}\cdot\text{min}^{-1}$, indicating that a higher reactant velocity is needed to achieve the same reactant saturation. Other reasons for the general improvement of performance may also include cell variability, a more uniform flow distribution in the dual-pass electrodes and the added 'flow-by' center portion of the electrode. Regardless of the origin, these performance differences lead to differences in fuel utilization and need to be considered in selecting the optimal operating point for fuel recirculation.

To maximize discharge power density the optimal operating potential is typically found around the 'knee' of the polarization

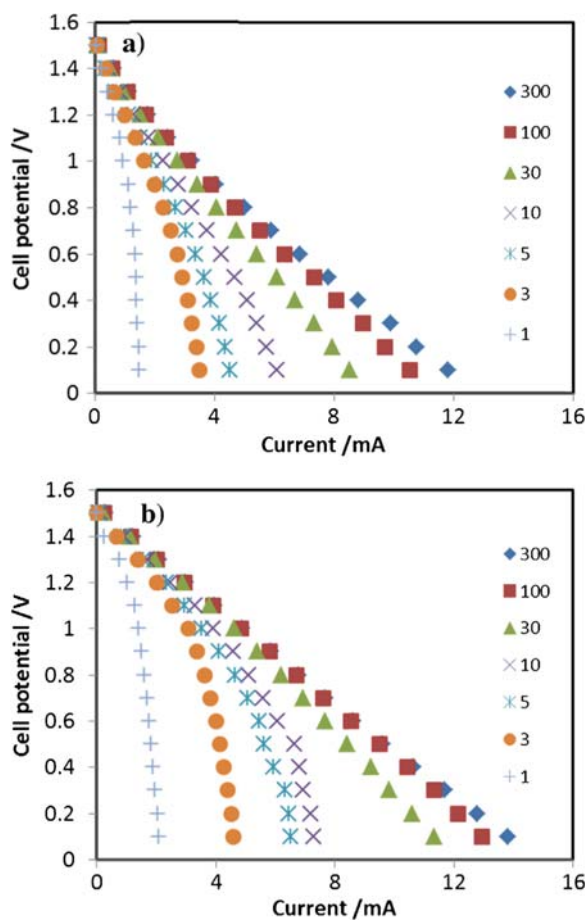


Fig. 7. Polarization curves at a range of flow rates (as indicated in $\mu\text{L}\cdot\text{min}^{-1}$) using high concentration (initial SOC=90%) reactants with the: a) Y-junction cell and b) 2nd generation dual-pass cell.

curve, before the mass transport effects dominate. Although the particular potential at which the maximum power occurs varies slightly for each flow rate, it is typically around 0.8 V for the high concentration reactants being considered. The fuel utilization for each cell calculated from the above polarization curves at this potential is presented in Fig. 8. The graph again clearly demonstrates the consequences of the improved performance of the 2nd generation dual-pass cell, which leads to higher fuel utilization at all flow rates.

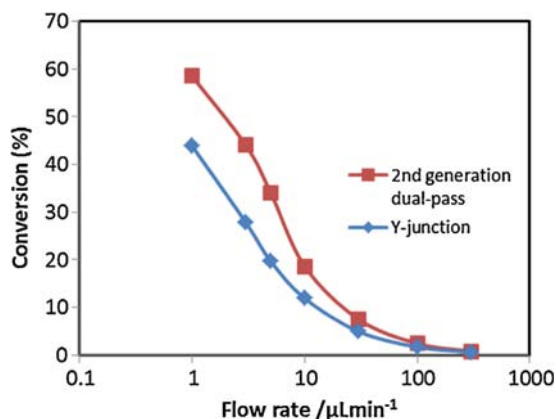


Fig. 8. Fuel utilization or conversion of high concentration (initial SOC=90%) reactants being discharged at 0.8 V.

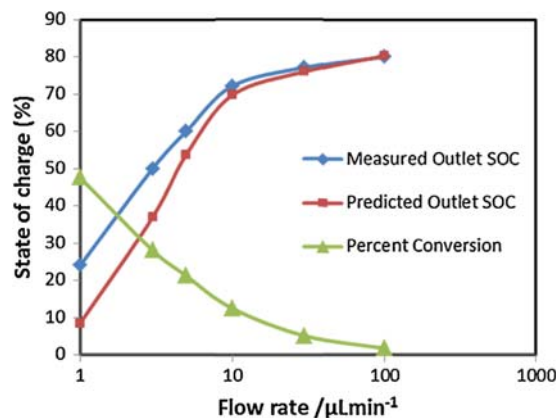


Fig. 9. Measured V(II) outlet concentration and predicted outlet concentration based on high concentration reactant crossover and percent of reactant converted.

Intuitively it may seem sufficient to combine the previous crossover data with the polarization and fuel utilization data to select the optimum operating point for most efficient fuel recirculation. Unfortunately for both types of cell architecture, the situation becomes more complex at higher fuel utilization. As an example, consider the crossover data presented in Fig. 9 for one of the outlets of the Y-junction cell during a potentiostatic discharge at 0.8 V at a variety of flow rates. The predicted remaining concentration C would be given by the relation in Eq. 3 below:

$$C_{\text{predicted}} = C_{\text{initial}} - C_{\text{loss}} - C_{\text{converted}} \quad (3)$$

As can be seen from the data, the measured outlet concentration differs more and more from this prediction as the flow rate decreases. For the Y-junction cell, the amount being converted can be as high as 50% at $1 \mu\text{L}\cdot\text{min}^{-1}$ which means that the concentration of reactants at the splitting point would only be $90\% - 50\% = 40\%$. In this case, it would be more relevant to use the low concentration crossover data from Fig. 4 rather than a high concentration of initial reactants. Indeed, the discrepancy between the predicted and measured concentration coincides reasonably with the difference between the crossover loss at 90% versus 50% initial reactants (*i.e.*, at $1 \mu\text{L}\cdot\text{min}^{-1}$, the difference between high and low concentration crossover from Fig. 4 is roughly 10%, whereas the difference between the measured and predicted SOC in Fig. 9 is roughly 15%). Although this direct comparison is possible for this flow rate, crossover data has not been measured for the entire range of initial reactant concentrations. Most importantly however, it should be noted that although low flow rates produce greater diffusion and crossover, they also result in greater fuel utilization which reduces the concentration of reactants at the splitting point, which in turn reduces the crossover. The relative importance of these effects is specific to each cell geometry and flow rate and therefore not amenable to systematic experimental characterization. The present crossover analysis on low and high concentrations provides reasonable bounds for predicting outlet concentrations in each case.

3.3. Reactant recirculation

In order to verify all of the information gathered thus far, it is illuminating to perform reactant recirculation experiments with both cell architectures under investigation. For this experiment each cell is tested in batch mode discharge operation with 600 μL of 90% initial state of charge reactants. The reactants are pumped through the cells at a flow rate of $30 \mu\text{L}\cdot\text{min}^{-1}$ and collected in separate syringes at the outlets to be recirculated for subsequent runs. For each consecutive run, the initial steady-state OCV of the cell is measured

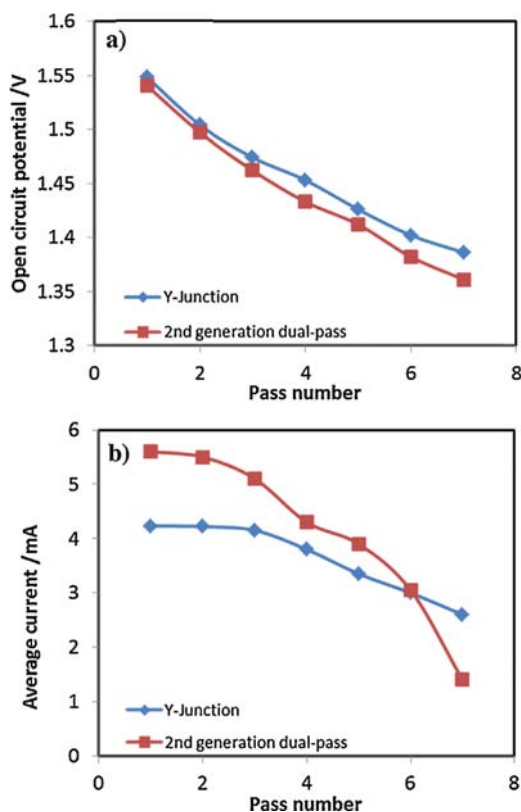


Fig. 10. Recirculation results for the two co-laminar flow cell architectures (Y-junction and dual-pass) based on seven consecutive batch mode discharge operations. Starting with high concentration (initial SOC = 90%) reactants, each discharge operation is conducted at $30 \mu\text{L}\cdot\text{min}^{-1}$ and 0.8 V with the outlet streams being collected in separate syringes for subsequent recirculation. The stepwise drop in reactant concentration is observed indirectly through: a) decrease in OCV and b) decrease in current.

after which the reactants are discharged at a potential of 0.8 V for the remainder of the reservoir volume. As expected, the drop in reactant concentration for each consecutive run is observed as the decrease in the OCV shown in Fig. 10-a). Similarly, the change in concentration can also be observed through the change in discharge current as in Fig. 10-b). Another way of observing the decrease in concentration is by simple visual inspection. Due to the range of

colors associated with the oxidation states of vanadium, the gradual change in concentration can be seen directly as in Fig. 11.

Several of the previously observed phenomena are confirmed through this analysis. Firstly, although both cells start with the same initial reactants, the OCV of the dual-pass cell is lower than that of the Y-junction due to the inevitable asymmetric crossover mentioned earlier. Secondly, the current is generally larger for the dual-pass cell due to its better performance. A closer look at the data also reveals the third trend seen earlier, namely the higher crossover rate for the dual-pass cell. Compiling the results from the previous analysis (Figs. 4 and 6), the crossover loss at $30 \mu\text{L}\cdot\text{min}^{-1}$ amounts to roughly 4% for the Y-junction cell and 8% for the dual-pass cell. During the first discharge operation the current yielded approximately 4.2 mA and 5.6 mA for the two cells, corresponding to roughly 5% and 7% conversion. The total expected concentration drop after the first run therefore adds up to 9% and 15% for the Y-junction and dual-pass cells, respectively. The same trend is expected to occur at each subsequent run, with the concentration of the dual-pass cell decreasing faster than the Y-junction. This is confirmed by the widening gap in OCV for the two cells in Fig. 10-a) and also with the faster decrease in current in Fig. 10-b) obtained with the dual-pass cell. In order to deconvolute this more rapid decay into a crossover component and a performance component, the final concentrations of the reactants are measured separately via reference electrode at the end of the seventh run. The average final concentration for the Y-junction reactants is around 27%, whereas it is 17% for the dual-pass cell. By calculating the total amount of reactant converted during all passes, it is possible to subtract this converted amount from the initial concentration to determine the amount lost to crossover during the experiment, as in Eq. 3. The total amounts converted are 31% for the Y-junction and 35% for the dual-pass cell, while the percentage of reactants lost to crossover are 32% and 38%, respectively. All of these results are directly reflected in the total energy output of the cells. By averaging the power produced over the seven 20 minute discharge operations, the final energy delivered was 24 J for the Y-junction and 28 J for the dual-pass cell.

As expected, this analysis confirms that the dual-pass cell has both higher performance and a higher rate of crossover, which ultimately leads to a more quickly decreasing concentration. The dual-pass cell therefore reaches mass transport limitations more quickly than the Y-junction, resulting in a lower final current in the seventh operation. Overall, this analysis demonstrates that even moderate quantitative knowledge about cell performance and

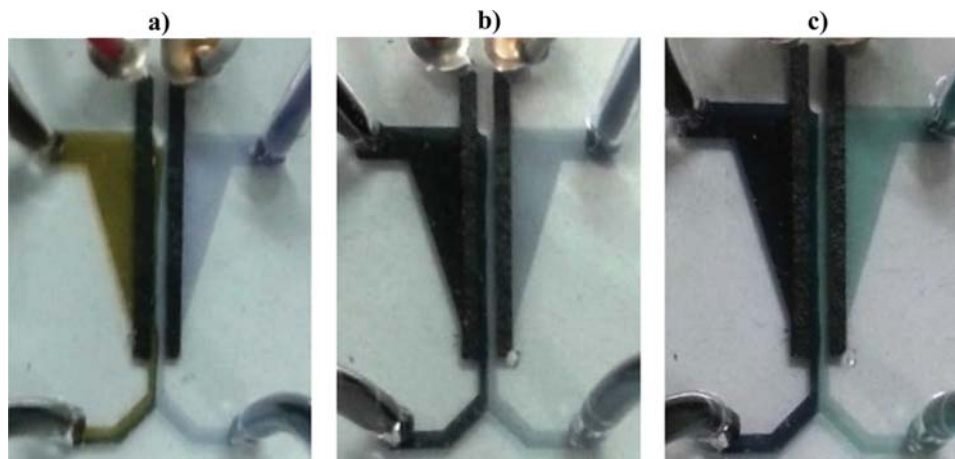


Fig. 11. Real-time images of co-laminar flow cells in batch mode recirculation operation at 0.8 V with reactants of varying concentration flowing downwards at $30 \mu\text{L}\cdot\text{min}^{-1}$. Change in color of a) initial high concentration yellow V(V) and purple V(II) in the first discharge, with a visible decrease in concentration by the b) third discharge, and starting to resemble the final blue V(IV) and green V(III) reactants by the c) fifth discharge.

crossover can provide reasonable predictions about fuel recirculation.

4. Conclusions

This study constitutes a thorough experimental investigation of reactant crossover and utilization in two types of co-laminar flow cells designed for fuel recirculation, namely the Y-junction and dual-pass cell architectures with flow-through porous electrodes. Reactant crossover at the electrodes reduces the open circuit potential of both cells and serves as a useful diagnostic method for assessing the degree of crossover, particularly for the dual-pass cell in which one-half of the electrodes is situated downstream from the splitting point of the co-laminar reactant streams and exposed to partially mixed reactants. Streamlined cell design is demonstrated as an effective mitigation strategy to reduce this type of reactant crossover. Measurements of outlet concentrations reveal that a minimum of 2% of initial concentration is regularly lost due to asymmetric splitting of the streams, imposing a fundamental limit on the efficiency of fuel recirculation. Concentration loss due to diffusion on the other hand is dependent on both flow rate and cell geometry and ranges from roughly 0–40% for the cells and flow rates considered. In general, the dual-pass cell is found to have greater diffusive loss due to its second reactant pass through the electrodes. In regards to performance, the dual-pass cell is shown to have both better performance and reactant utilization at all flow rates. The combination of these effects is directly observed by comparing the overall performance and concentration in both types of cells during a series of batch mode discharge operations with reactant recirculation. The greater current, reactant utilization, and diffusion loss of the dual-pass cell combine to produce a lower final concentration of reactants than for the Y-junction cell. Overall, the present results demonstrate the viability and usefulness of reactant recirculation as a practical approach to combine high reactant utilization and high power density in membraneless co-laminar flow cells.

Acknowledgements

Funding for this research provided by the Natural Sciences and Engineering Research Council of Canada, Western Economic Diversification Canada, Canada Foundation for Innovation, British Columbia Knowledge Development Fund, and Simon Fraser University (SFU) is highly appreciated.

References

- [1] A.Z. Weber, M.M. Mench, J.P. Meyers, P.N. Ross, J.T. Gostick, Q. Liu, Redox flow batteries: a review, *J. Appl. Electrochem.* 41 (2011) 1137–1164.
- [2] M.M. Mench, *Fuel Cell Engines*, John Wiley & Sons Inc, 2008.
- [3] A.D. Stroock, S.K.W. Dertinger, A. Ajdari, I. Mezic, H.A. Stone, G.M. Whitesides, Chaotic mixer for microchannels, *Science* 295 (2002) 647–651 (80–).
- [4] T. Thorsen, R.W. Roberts, F.H. Arnold, S.R. Quake, Dynamic Pattern Formation in a Vesicle-Generating Microfluidic Device, *Phys. Rev. Lett.* 86 (2001) 4163–4166.
- [5] A.E. Kamholz, B.H. Weigl, B.A. Finlayson, P. Yager, Quantitative analysis of molecular interaction in a microfluidic channel: the T-sensor, *Anal. Chem.* 71 (1999) 5340–5347.
- [6] S. Takayama, E. Ostuni, P. LeDuc, K. Naruse, D.E. Ingber, G.M. Whitesides, Sub-cellular positioning of small molecules, *Nature* 411 (2001) 1016.
- [7] H.A. Stone, A.D. Stroock, A. Ajdari, *Engineering Flows in Small Devices*, *Annu. Rev. Fluid Mech.* 36 (2004) 381–411.
- [8] E.R. Choban, L.J. Markoski, A. Wieckowski, P.J.A. Kenis, Microfluidic fuel cell based on laminar flow, *J. Power Sources* 128 (2004) 54–60.
- [9] R. Ferrigno, A.D. Stroock, T.D. Clark, M. Mayer, G.M. Whitesides, Membraneless Vanadium Redox Fuel Cell Using Laminar Flow, *J. Am. Chem. Soc.* 124 (2002) 12930–12931.
- [10] E. Kjeang, R. Michel, D.A. Harrington, N. Djilali, D. Sinton, A microfluidic fuel cell with flow-through porous electrodes, *J. Am. Chem. Soc.* 130 (2008) 4000–4006.
- [11] R.S. Jayashree, L. Gancs, E.R. Choban, A. Primak, D. Natarajan, L.J. Markoski, et al., Air-breathing laminar flow-based microfluidic fuel cell, *J. Am. Chem. Soc.* 127 (2005) 16758–16759.
- [12] E. Kjeang, N. Djilali, D. Sinton, Microfluidic fuel cells: A review, *J. Power Sources* 186 (2009) 353–369.
- [13] J.W. Lee, M.-A. Goulet, E. Kjeang, Microfluidic Redox Battery, *Lab Chip* 13 (2013) 2504–2507.
- [14] W.A. Braff, M.Z. Bazant, C.R. Buie, Membrane-less hydrogen bromine flow battery, *Nat. Commun.* 4 (2013) 2346.
- [15] J.W. Lee, J.K. Hong, E. Kjeang, Electrochemical characteristics of vanadium redox reactions on porous carbon electrodes for microfluidic fuel cell applications, *Electrochim. Acta* 83 (2012) 430–438.
- [16] D. Morales-Acosta, M.D. Morales-Acosta, L.A. Godinez, L. Álvarez-Contreras, S.M. Duron-Torres, J. Ledesma-García, et al., PdCo supported on multiwalled carbon nanotubes as an anode catalyst in a microfluidic formic acid fuel cell, *J. Power Sources* 196 (2011) 9270–9275.
- [17] J. Ma, A.S. Gago, N. Alonso-Vante, Performance Study of Platinum Nanoparticles Supported onto MWCNT in a Formic Acid Microfluidic Fuel Cell System, *J. Electrochem. Soc.* 160 (2013) F859–F866.
- [18] M.R. Thorson, F.R. Brushett, C.J. Timberg, P.J.A. Kenis, Design rules for electrode arrangement in an air-breathing alkaline direct methanol laminar flow fuel cell, *J. Power Sources* 218 (2012) 28–33.
- [19] N. Da Mota, D.A. Finkelstein, J.D. Kirtland, C.A. Rodriguez, A.D. Stroock, H.D. Abruña, Membraneless, room-temperature, direct borohydride/cerium fuel cell with power density of over 0.25 W/cm², *J. Am. Chem. Soc.* 134 (2012) 6076–6079.
- [20] S. Moore, D. Sinton, D. Erickson, A plate-frame flow-through microfluidic fuel cell stack, *J. Power Sources* 196 (2011) 9481–9487.
- [21] A.S. Hollinger, P.J.A. Kenis, Manufacturing all-polymer laminar flow-based fuel cells, *J. Power Sources* 240 (2013) 486–493.
- [22] K.S. Salloum, J.D. Posner, A membraneless microfluidic fuel cell stack, *J. Power Sources* 196 (2011) 1229–1234.
- [23] B. Ho, E. Kjeang, Planar Multiplexing of Microfluidic Fuel Cells, *J. Fluids Eng.* 135 (2013) 021304.
- [24] J.W. Lee, E. Kjeang, Nanofluidic Fuel Cell, *J. Power Sources* 242 (2013) 472–477.
- [25] E. Kjeang, R. Michel, D.A. Harrington, D. Sinton, N. Djilali, An alkaline microfluidic fuel cell based on formate and hypochlorite bleach, *Electrochim. Acta* 54 (2008) 698–705.
- [26] J.W. Lee, E. Kjeang, Chip-embedded thin film current collector for microfluidic fuel cells, *Int. J. Hydrogen Energy* 37 (2012) 9359–9367.
- [27] M. Skyllas-Kazacos, New All-Vanadium Redox Flow Cell (1986).
- [28] M. Skyllas-Kazacos, C. Menictas, M. Kazacos, Thermal Stability of Concentrated V(V) Electrolytes in the Vanadium Redox Cell, *J. Electrochem. Soc.* 143 (1996) 86–88.
- [29] D. Krishnamurthy, E.O. Johansson, J.W. Lee, E. Kjeang, Computational modeling of microfluidic fuel cells with flow-through porous electrodes, *J. Power Sources* 196 (2011) 10019–10031.

Appendix C.

Direct measurement of electrochemical reaction kinetics in flow-through porous electrodes



Direct measurement of electrochemical reaction kinetics in flow-through porous electrodes



Marc-Antoni Goulet^a, Michael Eikerling^b, Erik Kjeang^{a,*}

^a School of Mechatronics Systems Engineering, Simon Fraser University, 250-13450 102 Avenue, Surrey, BC V3T 0A3, Canada

^b Department of Chemistry, Simon Fraser University, 8888 University Drive, Burnaby, BC V5A 1S6, Canada

ARTICLE INFO

Article history:

Received 7 April 2015

Received in revised form 30 April 2015

Accepted 30 April 2015

Available online 8 May 2015

Keywords:

Tafel

Kinetics

Flow-through porous electrode

Microfluidic

Flow cell

Vanadium

ABSTRACT

This work demonstrates the feasibility of measuring electrochemical reaction rates on common flow-through porous electrodes by traditional Tafel analysis. A customized microfluidic channel electrode was designed and demonstrated by measuring the intrinsic kinetics of the V^{2+}/V^{3+} and VO^{2+}/VO_2^+ redox reactions in carbon paper electrodes under forced electrolyte flow. The exchange current density of the V^{2+}/V^{3+} reaction was found to be nearly two orders of magnitude slower than the VO^{2+}/VO_2^+ reaction, indicating that this may be the limiting reaction in vanadium redox flow batteries. The forced convection in this technique is found to generate reproducible exchange current densities which are consistently higher than for conventional electrochemical methods due to improved mass transport.

© 2015 Elsevier B.V. All rights reserved.

1. Introduction

A commonly employed strategy to enhance effective rates of interfacial electrochemical reactions is to design and fabricate porous electrodes with high interfacial area between electronic and ionic conducting phases. Porous electrodes with nanoscopic feature sizes increase the electrochemical surface area (ESA) per unit electrode volume and thereby improve the voltage efficiency of electrochemical energy conversion.

Studying reaction rates on porous electrodes is not as straightforward however as on their planar counterparts. Traditional methods of studying reaction kinetics such as cyclic voltammetry are biased by the porosity, where a smaller peak to peak separation may falsely indicate improved kinetics if the semi-infinite diffusion criterion is ignored [1–3]. Tafel analysis by rotating disk method on porous electrodes has also been shown to lead to higher Tafel slopes particularly for electrodes with deeper pores [4]. Although rotation of the electrode increases convection and reactant replenishment at the surface of the electrode, this convection does not improve penetration of the reaction front into the depths of electrolyte-filled pores. Diffusion limitations, as accounted for in the transmission line model of De Levie [5,6], constrain the performance of porous electrodes. When the reaction penetration depth is much smaller than the thickness of the electrode in a 1D system, this diffusion limitation will lead to an exact doubling of the

Tafel slope [7]. One strategy to reduce diffusion limitations is to reduce the size of the electroactive area, as in the study with ultra-low catalyst loading by Zalitis et al. [8]. To overcome diffusion limitations in general, some researchers have proposed other indirect analytical methods of determining the reaction kinetics of porous materials independently from their morphology [9–11].

While some porous electrodes, such as those of traditional closed-cell batteries, have internal pore structure exclusively designed for diffusion of electroactive species, others are designed with open pores to permit convective flow of reactants. These ‘flow-through porous electrodes’ have long been considered for electrochemical uses such as the recovery of electropositive metals from industrial waste and oxidation of organic pollutants and surfactants [12]. These large scale applications typically utilize a packed or fluidized bed electrochemical reactor with electrodes composed of a layer of highly conductive non-porous particles supported by a current collector grid [13]. Several studies were performed in the 1960s and 1970s to quantify the polarization behavior and potential distribution in such electrodes [5,6,12–19]. Since then, other types of flow-through porous electrodes such as carbon felt have become a popular material and an integral part of redox flow batteries, a new class of batteries which rely on convective mass transport of externally stored reactants [20]. More recently, similar carbon paper electrodes have also been shown to considerably improve the performance of microfluidic co-laminar flow cells [21–24]. Growing interest in these technologies warrants more contemporary research into the polarization behavior of flow-through porous electrodes, which have been largely neglected in the literature, in favor of thin

* Corresponding author. Tel.: +1 778 782 8791; fax: +1 778 782 7514.

E-mail address: ekjeang@sfu.ca (E. Kjeang).

film diffusion based porous electrodes. Moreover, new low cost microfabrication techniques have made it possible for research groups to develop customized microfluidic analytical flow cells [21,25]. At the micro scale, flow is typically laminar and therefore amenable to analytical solution [26]. This allowed the Compton group to develop the concept of channel electrodes as an improvement over rotating disk methods for measuring polarization of planar electrodes [27]. Developing this idea further, the objective of the present work is to demonstrate the viability of using a customized microfluidic electrochemical cell for directly measuring the kinetics and general polarization behavior of accessible flow-through porous electrodes.

2. Methodology

2.1. Materials

The reactants used in this study are the V^{2+}/V^{3+} and VO^{2+}/VO_2^+ redox couples first proposed by Skyllas-Kazacos et al. [28] for the all-vanadium redox flow battery and more recently employed in our co-laminar flow cells [29,30]. The reactants are prepared by charging a 1.7 M commercial grade vanadium stock solution in 4 M H_2SO_4 with a conventional flow battery to achieve a nearly even ratio of V^{2+}/V^{3+} or VO^{2+}/VO_2^+ . Initial concentrations are determined by permanganate titration [29]. The working electrode (WE) and counter electrode (CE) are both made from 180 μm thick Toray carbon paper (TGP-H 060) which is heat treated to increase hydrophilicity as explained in previous work [23]. The carbon paper surface area is measured to be $4 m^2 \cdot g^{-1}$ via mercury intrusion porosimetry which results in an estimated ESA of roughly $4 cm^2$ for the WE used in this study.¹

2.2. Design and fabrication

The microfluidic analytical flow cell is fabricated by soft lithography of poly(dimethylsiloxane) (PDMS) from a photoresist template as described elsewhere [31,32]. As depicted in Fig. 1, the cell consists of a single inlet and outlet with a uniform channel height of 150 μm to compress the electrodes and a channel width of 2 mm in the upstream WE section which gradually expands to a 4 mm width in the downstream CE section. The CE is sized to provide an order of magnitude larger ESA than the WE. Once the electrodes are placed within their respective grooves, the cell is capped by a glass slide and pressure sealed by a customized clamp. Contact is made with the electrodes which extend beyond the cell via copper clips. A saturated calomel reference electrode (RE) is positioned roughly 3 mm upstream from the WE with electrolytic contact made via a porous frit sealed into the PDMS channel. For better visualization of reactant conversion however quasi-reference electrodes are used based on silver and platinum foil for V^{2+}/V^{3+} and VO^{2+}/VO_2^+ respectively.

2.3. Half-cell characterization

The electrolyte is injected into the inlet by syringe pump and removed by a separate syringe pump at the outlet. The two pumps (Harvard Apparatus MA1 70-2209) are operated in unison at flow rates ranging from 2 to 2000 $\mu L \cdot min^{-1}$. All polarization measurements are made with a potentiostat (Gamry Reference 3000) operating at voltammetric scan rates slow enough to ensure steady state conditions. Electrochemical impedance spectroscopy (EIS) measurements are conducted at 10 mV perturbation from the open circuit potential (OCP) to determine the impedance of the WE and make post-run IR corrections. With IR correction, both the saturated calomel and quasi-reference methods generate identical polarization behavior for a given WE.

¹ It should be noted that the true surface area of carbon and that wetted by the electrolyte may differ markedly from this value.

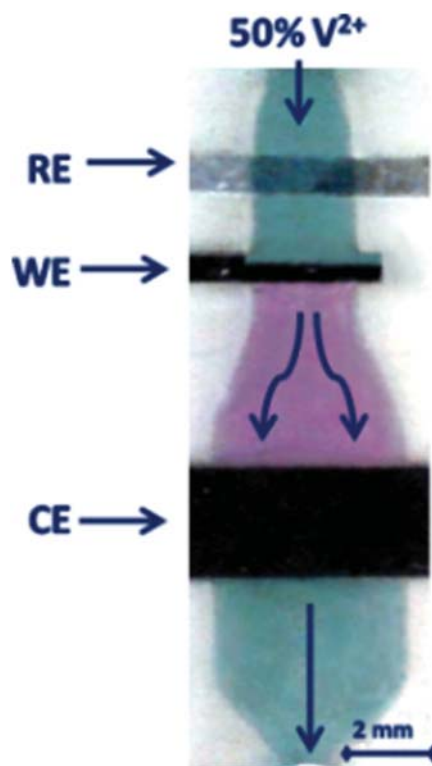


Fig. 1. Annotated image of the analytical flow cell in operation, showing complete reduction and oxidation of V^{2+}/V^{3+} in carbon paper working and counter electrodes, respectively.

3. Results and discussion

3.1. Validation

The stability of the system is first established within the experimental conditions. At negative pH, silver is stable at the negative potential of the V^{2+}/V^{3+} electrolyte whereas platinum is stable at the positive potential of the VO^{2+}/VO_2^+ electrolyte. This is observed by minimal drift (<10 mV) in the OCP of either solution over the course of several hours. The initial concentrations are verified by complete reactant conversion as in Fig. 1, which shows the complete reduction of green V^{3+} to purple V^{2+} . At a flow rate of $2 \mu L \cdot min^{-1}$ the anodic and cathodic limiting currents are averaged over the final 50 mV of the ± 300 mV overpotential range, producing 2.7 ± 0.2 mA and 2.8 ± 0.2 mA which correspond to full conversion of initial concentrations of 49% V^{2+} and 51% V^{3+} respectively from the total 1.7 M vanadium concentration. This demonstrates that all of the electrolyte injected into the flow-through cell can react without any flow bypassing the electrode and that no undesirable side reactions are occurring within the present potential range. The same validation was performed for the VO^{2+}/VO_2^+ solution, revealing initial concentrations of 54% and 46% respectively and no side-reactions within a ± 400 mV overpotential range.

3.2. Electrochemical kinetics

The Tafel curves in Fig. 2 demonstrate qualitatively the effect of flow rate on the polarization behavior of both redox reactions on the same WE. Above $400 \mu L \cdot min^{-1}$ there is little change in the polarization of the V^{2+}/V^{3+} reaction whereas the VO^{2+}/VO_2^+ polarization continues to change even beyond $1200 \mu L \cdot min^{-1}$, indicating that the V^{2+}/V^{3+} reaction is considerably slower than the VO^{2+}/VO_2^+ reaction. Although there is disagreement in the literature [33–35], most experimental studies with solutions that mimic those used in commercial flow battery systems have found that the VO^{2+}/VO_2^+ reaction is faster on carbon

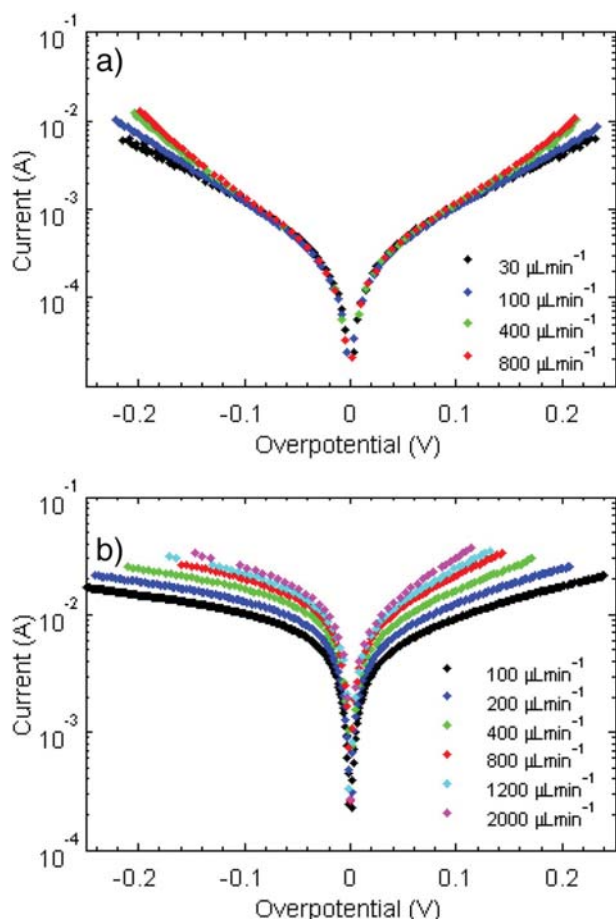


Fig. 2. IR corrected Tafel curves of the a) V^{2+}/V^{3+} and b) VO^{2+}/VO_2^+ reactions.

electrodes [36–41], even though it has a multistep reaction mechanism with both chemical and electrochemical steps [35]. Another feature reported in the literature also seen here is the asymmetry between the anodic and cathodic branch of the VO^{2+}/VO_2^+ reaction [35,42].

The Tafel slopes depicted in Fig. 3 display an asymptotic approach toward a constant value for both reactions. The oxidation and reduction Tafel slopes of the V^{2+}/V^{3+} reaction settle around 120 and 110 $mV \cdot dec^{-1}$ respectively, with minimal change ($<5 mV \cdot dec^{-1}$) beyond 400 $\mu L \cdot min^{-1}$. These values closely match the 118 $mV \cdot dec^{-1}$

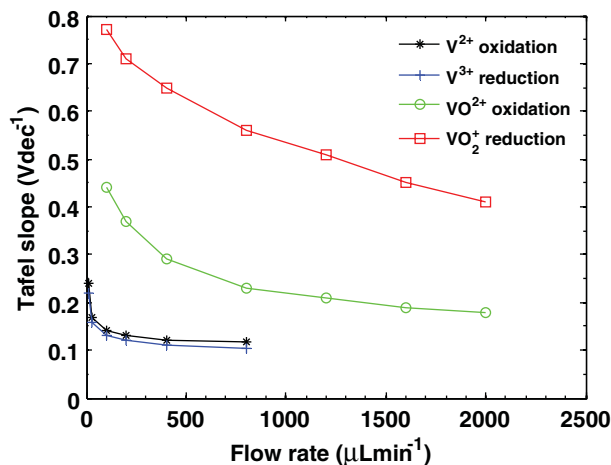


Fig. 3. IR corrected Tafel slopes of a) V^{2+}/V^{3+} at 30–800 $\mu L \cdot min^{-1}$ and b) VO^{2+}/VO_2^+ at 100–2000 $\mu L \cdot min^{-1}$.

predicted by Butler–Volmer kinetics for a simple one-electron transfer reaction in the absence of diffusion limitations. At 400 $\mu L \cdot min^{-1}$ the maximum current in Fig. 2-a) corresponds to only 2.5% conversion of available reactant, which further supports the notion of purely kinetic control. The intercept of the linear Tafel slope reveals an exchange current of roughly 0.17 mA for this reaction corresponding to $i_0 = 0.04 mA \cdot cm^{-2}$ when normalized by the ESA, which agrees closely with the exchange current density of SGL 10AA carbon paper published by Aaron et al. [39] after correcting for the effect of concentration. The present flow cell method is intended to overcome the presence of mass transport effects in the previous study by Lee et al. [38] which used the same electrode material immersed in a stirred solution of the same electrolyte. When normalized by the volume of the immersed electrode, which scales proportionally with the ESA, the i_0 obtained via the flow cell technique is approximately 1.5 orders of magnitude larger than the previous method, indicating that the stirred solution was ineffective at replenishing the reactants within the porous electrode, which can also be observed by the large Tafel slopes in that study.

Although the Tafel slopes for the VO^{2+}/VO_2^+ reaction in Fig. 3 do not reach a constant value, taking the average of the anodic and cathodic intercepts at 2000 $\mu L \cdot min^{-1}$ provides an estimate of $i_0 \approx 3 mA \cdot cm^{-2}$. This nearly two orders of magnitude higher rate of the VO^{2+}/VO_2^+ reaction relative to the V^{2+}/V^{3+} reaction is higher than that observed by Aaron et al. [39] due to the improved mass transport. To more accurately determine the purely kinetic rate of this reaction, higher flow rates and/or reduced electrode size would be required to increase the reaction penetration depth. In either case, the Tafel slopes are unlikely to reach 118 $mV \cdot dec^{-1}$ due to the multistep reaction mechanisms postulated by Gattrell et al. [35].

The exchange current densities observed result in heterogeneous rate constants on the order of 10^{-7} and $10^{-5} cm \cdot s^{-1}$ for the V^{2+}/V^{3+} and VO^{2+}/VO_2^+ reactions respectively. Compared to the rates measured via cyclic voltammetry on planar carbon electrodes, the magnitude for the V^{2+}/V^{3+} reaction falls below the range reported in the literature [36,40], whereas the VO^{2+}/VO_2^+ rate is comparable to that found in the literature [35,40]. This suggests that planar carbon electrodes may not be representative of the intrinsic reaction rates on the porous carbon electrodes used in vanadium redox flow batteries. It should be noted however, that the surface properties of carbon materials and the electrolyte composition may have a considerable impact on the wettability and reaction kinetics of either redox couple.

3.3. Discussion

The contrast between the two redox couples is presented to highlight some of the strengths and limitations of the flow cell technique. When repeated with different working electrodes of the same material at an appropriate flow rate, the sluggish V^{2+}/V^{3+} reaction demonstrates good reproducibility, averaging to $i_0 = 0.05 \pm 0.01 mA \cdot cm^{-2}$. Faster reactions such as VO^{2+}/VO_2^+ on the other hand require higher flow rates or thinner electrodes. In both cases the experiment is constrained by the high flow velocity, in this case 2000 $\mu L \cdot min^{-1}$ being equivalent to 0.1 $m \cdot s^{-1}$ within the channel, which may damage the brittle electrode. It should also be noted that this technique is only useful for flow-through porous electrodes with a narrow pore size distribution which promotes relatively uniform flow over the entire electrochemically active surface.

As a new experimental technique more work needs to be done to optimize the cell design to make it useful for a wide range of reactions and purposes. The effect of channel width was briefly studied, with a $2.5 \times$ wider cell producing roughly the same (within 10%) exchange current density for the V^{2+}/V^{3+} reaction, suggesting minimal edge effects. More work should be done in this regard to refine the technique in parallel to the development of planar channel electrodes [27]. Features such as a separate outlet port for collecting reactants converted by the WE could also be added to increase functionality.

4. Conclusions

A microfluidic three electrode flow cell was developed to study the kinetics of flow-through porous electrodes. It was shown that at sufficiently high flow rates, Tafel analysis can be performed without the need for mass transport corrections. To demonstrate the capabilities of the method, the kinetic rates of the V^{2+}/V^{3+} and VO^{2+}/VO_2^+ reactions on Toray carbon paper were compared. In support of most of the literature, the V^{2+}/V^{3+} reaction was shown to be substantially slower than the VO^{2+}/VO_2^+ reaction and therefore the limiting reaction in vanadium redox batteries based on these materials. Made with ubiquitous microfabrication techniques this cell could also become a useful tool to study both kinetic and mass transport effects on the polarization behavior of flow-through porous electrodes in a way which mimics their use in electrochemical flow cells. Relating the current density to a particular overpotential and flow rate is not possible with cyclic voltammetry or rotating disk methods. This kind of polarization data is essential for complete modeling and design optimization of fuel cells and flow batteries.

Conflict of interest

The authors declare no conflict of interest.

Acknowledgments

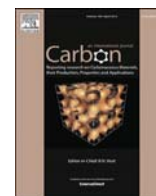
Funding for this research provided by the Natural Sciences and Engineering Research Council of Canada, Western Economic Diversification Canada, Canada Foundation for Innovation, and British Columbia Knowledge Development Fund is highly appreciated.

References

- [1] D. Menshkykau, R.G. Compton, The influence of electrode porosity on diffusional cyclic voltammetry, *Electroanalysis* 20 (2008) 2387–2394.
- [2] D. Menshkykau, I. Streeter, R.G. Compton, Influence of electrode roughness on cyclic voltammetry, *J. Phys. Chem. C* 112 (2008) 14428–14438.
- [3] I. Streeter, G.G. Wildgoose, L. Shao, R.G. Compton, Cyclic voltammetry on electrode surfaces covered with porous layers: an analysis of electron transfer kinetics at single-walled carbon nanotube modified electrodes, *Sensors Actuators B Chem.* 133 (2008) 462–466.
- [4] J.N. Soderberg, A.C. Co, A.H.C. Sirk, V.I. Birss, Impact of porous electrode properties on the electrochemical transfer coefficient, *J. Phys. Chem. B* 110 (2006) 10401–10410.
- [5] R. De Levie, On porous electrodes in electrolyte solutions—IV, *Electrochim. Acta* 9 (1964) 1231–1245.
- [6] R. De Levie, Electrochemical response of porous and rough electrodes, *Adv. Electrochem. Electrochem. Eng.* 6 (1967) 329–397.
- [7] M. Eikerling, A. Kulikovskiy, Polymer Electrolyte Fuel Cells: Physical Principles of Materials and Operation, CRC Press, 2014.
- [8] C.M. Zalitis, D. Kramer, A.R. Kucernak, Electrocatalytic performance of fuel cell reactions at low catalyst loading and high mass transport, *Phys. Chem. Chem. Phys.* 15 (2013) 4329–4340.
- [9] A.A. Kulikovskiy, M. Eikerling, Analytical solutions for impedance of the cathode catalyst layer in PEM fuel cell: layer parameters from impedance spectrum without fitting, *J. Electroanal. Chem.* 691 (2013) 13–17.
- [10] J. Friedl, C.M. Bauer, A. Rinaldi, U. Stimming, Electron transfer kinetics of the $VO_2^+ / VO + 2$ reaction on multi-walled carbon nanotubes, *Carbon N. Y.* 63 (2013) 228–239.
- [11] C. Punckt, M.A. Pope, I.A. Aksay, On the electrochemical response of porous functionalized graphene electrodes, *J. Phys. Chem. C* 117 (2013) 16076–16086.
- [12] J. Newman, W. Tiedemann, Porous-electrode theory with battery applications, *AIChE J.* 21 (1975) 25–38.
- [13] M. Paulin, D. Hutin, Theoretical and experimental study of flow-through porous electrodes, *J. Electrochem. Soc.* 124 (1977) 180–188.
- [14] R. Alkire, B. Gracon, Flow through porous electrodes, *J. Electrochem. Soc.* 122 (1975) 1594–1601.
- [15] B.G. Ateya, L.G. Austin, Steady-state polarization at porous, flow-through electrodes with small pore diameter ii irreversible kinetics, *J. Electrochem. Soc.* 9 (1977) 1540–1548.
- [16] B.G. Ateya, L.G. Austin, Steady-state polarization at porous, flow-through electrodes with small pore diameter i reversible kinetics, *J. Electrochem. Soc.* 124 (1977) 83–89.
- [17] F. Coeuret, D. Hutin, A. Gaunand, Study of the effectiveness of fixed flow-through electrodes, *J. Appl. Electrochem.* 6 (1976) 417–423.
- [18] R.E. Sioda, Electrolysis with flowing solution on porous and wire electrodes, *Electrochim. Acta* 15 (1970) 783–793.
- [19] R.E. Sioda, Distribution of potential in a porous electrode under conditions of flow electrolysis, *Electrochim. Acta* 16 (1971) 1569–1576.
- [20] A.Z. Weber, M.M. Mench, J.P. Meyers, P.N. Ross, J.T. Gostick, Q. Liu, Redox flow batteries: a review, *J. Appl. Electrochem.* 41 (2011) 1137–1164.
- [21] M.-A. Goulet, E. Kjeang, Co-laminar flow cells for electrochemical energy conversion, *J. Power Sources* 260 (2014) 186–196.
- [22] E. Kjeang, N. Djilali, D. Sinton, Microfluidic fuel cells: a review, *J. Power Sources* 186 (2009) 353–369.
- [23] E. Kjeang, R. Michel, D.A. Harrington, N. Djilali, D. Sinton, A microfluidic fuel cell with flow-through porous electrodes, *J. Am. Chem. Soc.* 130 (2008) 4000–4006.
- [24] E. Kjeang, Microfluidic Fuel Cells and Batteries, Springer, 2014.
- [25] G.M. Whitesides, The origins and the future of microfluidics, *Nature* 442 (2006) 368–373.
- [26] E. Kjeang, B. Roesch, J. McKechnie, D.A. Harrington, N. Djilali, D. Sinton, Integrated electrochemical velocimetry for microfluidic devices, *Microfluid. Nanofluid.* 3 (2006) 403–416.
- [27] J.A. Cooper, R.G. Compton, Channel electrodes – a review, *Electroanalysis* 10 (1998) 141–155.
- [28] M. Skyllas-Kazacos, New all-vanadium redox flow cell, *J. Electrochem. Soc.* 133 (1986) 1057–1058.
- [29] M.-A. Goulet, E. Kjeang, Reactant recirculation in electrochemical co-laminar flow cells, *Electrochim. Acta* 140 (2014) 217–224.
- [30] J.W. Lee, M.-A. Goulet, E. Kjeang, Microfluidic redox battery, *Lab Chip* 13 (2013) 2504–2507.
- [31] J. Cooper McDonald, J. Anderson, D. Chiu, H. Wu, Fabrication of microfluidic systems in poly (dimethylsiloxane), *Electrophoresis* 21 (2000) 27–40.
- [32] E. Kjeang, R. Michel, D.A. Harrington, D. Sinton, N. Djilali, An alkaline microfluidic fuel cell based on formate and hypochlorite bleach, *Electrochim. Acta* 54 (2008) 698–705.
- [33] H. Kaneko, K. Nozaki, Y. Wada, T. Aoki, A. Negishi, M. Kamimoto, Vanadium redox reactions and carbon electrodes for vanadium redox flow battery, *Electrochim. Acta* 36 (1991) 1191–1196.
- [34] S. Zhong, M. Skyllas-Kazacos, Electrochemical behaviour of vanadium(V)/Vanadium(IV) redox couple at graphite electrodes, *J. Power Sources* 39 (1992) 1–9.
- [35] M. Gattrell, J. Park, B. MacDougall, J. Apte, S. McCarthy, C.W. Wu, Study of the mechanism of the vanadium 4+/5+ redox reaction in acidic solutions, *J. Electrochem. Soc.* 151 (2004) A123.
- [36] E. Sum, M. Skyllas-Kazacos, A study of the V(II)/V(III) redox couple for redox flow cell applications, *J. Power Sources* 15 (1985) 179–190.
- [37] E. Sum, M. Rychcik, M. Skyllas-Kazacos, Investigation of the V(V)/V(IV) system for use in the positive half-cell of a redox battery, *J. Power Sources* 16 (1985) 85–95.
- [38] J.W. Lee, J.K. Hong, E. Kjeang, Electrochemical characteristics of vanadium redox reactions on porous carbon electrodes for microfluidic fuel cell applications, *Electrochim. Acta* 83 (2012) 430–438.
- [39] D. Aaron, C.-N. Sun, M. Bright, A.B. Papandrew, M.M. Mench, T.A. Zawodzinski, In situ kinetics studies in all-vanadium redox flow batteries, *ECS Electrochem. Lett.* 2 (2013) A29–A31.
- [40] T. Yamamura, N. Watanabe, T. Yano, Y. Shiokawa, Electron-transfer kinetics of Np^{3+}/Np^{4+} , NpO_2^{2+}/NpO_2^{2+} , V^{2+}/V^{3+} , and VO_2^+/VO_2^+ at carbon electrodes, *J. Electrochem. Soc.* 152 (2005) A830.
- [41] G. Oriji, Y. Katayama, T. Miura, Investigations on V(IV)/V(V) and V(II)/V(III) redox reactions by various electrochemical methods, *J. Power Sources* 139 (2005) 321–324.
- [42] M. Gattrell, J. Qian, C. Stewart, P. Graham, B. MacDougall, The electrochemical reduction of VO_2^+ in acidic solution at high overpotentials, *Electrochim. Acta* 51 (2005) 395–407.

Appendix D.

The importance of wetting in carbon paper electrodes for vanadium redox reactions



The importance of wetting in carbon paper electrodes for vanadium redox reactions



Marc-Antoni Goulet ^a, Maria Skyllas-Kazacos ^b, Erik Kjeang ^{a,*}

^a School of Mechatronic Systems Engineering, Simon Fraser University, 250-13450 102 Avenue, Surrey, BC, V3T 0A3, Canada

^b School of Chemical Engineering, UNSW Australia, Sydney, NSW 2052, Australia

ARTICLE INFO

Article history:

Received 10 September 2015

Received in revised form

2 February 2016

Accepted 3 February 2016

Available online 9 February 2016

ABSTRACT

As demand for renewable energy storage increases, flow batteries such as those based on the resilient vanadium redox reactants and inexpensive carbon electrode materials have become more widespread. Thus far, however, there are many conflicting results in the literature regarding the reaction kinetics of the V^{2+}/V^{3+} and VO^{2+}/VO_2^+ redox couples and various methods to enhance these reactions. The present work demonstrates how the misinterpretation of cyclic voltammetry for porous carbon materials may account for many of these inconsistencies. Several oxidation treatments investigated here are observed to have a significant effect on the cyclic voltammogram of the V^{2+}/V^{3+} redox couple reactions. Using electrochemical impedance spectroscopy and a recently developed analytical flow cell technique, these changes are shown to be due almost entirely to the effective wetting of the porous carbon paper rather than any electroactivation effect of surface functional groups on the intrinsic kinetics of the V^{2+}/V^{3+} reaction. A similar methodology is recommended for any future assessment of electrode treatments.

© 2016 Elsevier Ltd. All rights reserved.

1. Introduction

Cost effective grid scale energy storage has been identified as one of the key factors for the successful adoption of intermittent renewable energy such as wind and solar [1]. Flow batteries have recently become an attractive option for such load levelling applications due to the simplicity of scaling their energy content by adjusting the size of their externally stored electrolyte tanks [2]. One of the earliest and most established varieties of this technology is the vanadium redox flow battery which uses vanadium reactants in a sulfuric acid supporting electrolyte for both the anode and cathode. By using the same element on both sides, this all-vanadium system has the potential for long lifetimes by avoiding cross-contamination of the electrolyte streams [3]. Based on low cost materials such as graphite felt electrodes this battery is estimated to have a lower capital cost than other similar energy storage technologies such as flywheels or lithium ion batteries [4]. Development of this technology over the past three decades has ranged from electrochemical studies of the individual vanadium reactions [5,6] to single cell studies [7–9], kilowatt scale stack design [10,11],

and even commercial megawatt scale installations [4]. In order to maximize the cycle efficiency and increase the power density of vanadium batteries much research has been conducted to improve the reversibility of both the V^{2+}/V^{3+} and VO^{2+}/VO_2^+ redox reactions on flow-through porous carbon electrodes. These efforts have included the early work by Sun and Skyllas-Kazacos on thermal and chemical pre-treatments to impart surface oxide functional groups as active sites on graphite felts [12,13], deposition of carbon nanomaterials [14–21], surface functionalization with nitrogen [18,22–29] or oxygen functional groups [21,28,30–45], metal catalyst loading [46–53], and electrolyte additives [52,54–56]. Unfortunately many of these studies lack the methodology required for a proper quantitative analysis of the advertised enhancements of reaction rates. Moreover some of the studies, particularly those regarding surface functionalization with oxygen functional groups, contradict each other even qualitatively. For instance, a study by Yue et al. suggests that hydroxylation of carbon electrodes improves their catalytic activity for both the V^{2+}/V^{3+} and VO^{2+}/VO_2^+ reactions [33]. Other studies by González et al. [31] and Li et al. [40] claim that a reduction of graphene oxide, with an associated decrease in hydroxyl function groups, produces drastically improved electrocatalytic activity. With little reproducibility in the literature it is difficult to draw any firm conclusions about which treatments may be most effective. Moreover there is considerable

* Corresponding author.

E-mail address: ekjeang@sfu.ca (E. Kjeang).

disagreement in the literature over which reaction may be limiting for the vanadium redox battery. Although some older studies have found the V^{2+}/V^{3+} redox couple to have faster kinetics [57–59], most experimental studies have now shown the positive VO^{2+}/VO_2^+ half-cell to be the faster redox couple [5,6,60–64] on commercially relevant carbon electrode materials. In this case, it is unfortunate that the vast majority of the studies mentioned above focus on improving the kinetics of this reaction.

In nearly all of the above-cited studies, cyclic voltammetry has been the primary method used for demonstrating either quantitatively or qualitatively the reaction rate of either redox couple and the effects of treatment on the kinetics thereof. Typically, a decrease in the potential separation between anodic and cathodic reaction peaks has been used to justify an improvement in the kinetics of reaction. This type of analysis is based on the Nicholson method which was derived for the ideal case of 1D diffusion from a semi-infinite planar electrode [65,66]. It has been repeatedly shown in the literature that changes in porosity and surface roughness can have a considerable impact on the peak to peak separation [67–71]. For highly porous materials such as carbon paper and graphite felt, however, other methods are required to assess the effects of electrode treatment on the intrinsic kinetics of the vanadium redox reactions. Deposition of additional porous catalyst layers and carbon nanoparticles only further complicate the issue. Moreover, most studies do not seem to apply IR correction to their CV data, which can significantly affect peak separation.

The present work aims to highlight yet another factor, namely physical wetting of the electrode, which may compound the issue and potentially introduce a significant source of error which makes the interpretation of the cyclic voltammetry results in the literature ever more dubious. Along with visual inspection, both cyclic voltammetry and electrochemical impedance spectroscopy (EIS) are used to demonstrate the connection between wetting, capacitance, charge transfer resistance (R_{ct}), and voltammetric peak separation. In addition, a new experimental method recently developed by our group [64] to mitigate diffusion effects is used to provide corroborating evidence for the observed phenomena.

2. Methodology

2.1. Materials

The starting electrolyte used in this study was prepared by reactive dissolution of V_2O_3 and V_2O_5 in sulfuric acid by a method previously described by Skyllas-Kazacos [72]. The mixed V(III)/V(IV) electrolyte produced (referred to here as $V^{3.5+}$) was then placed into both half-cells of a redox flow cell and fully charged at a current density of 40 mA cm^{-2} to produce V(II) and V(V) solutions in the negative and positive half-cells respectively. These were then mixed in the required ratios to achieve 50% state of charge solutions of V^{2+}/V^{3+} and VO^{2+}/VO_2^+ . The approximately 2 M electrolyte was then analysed by Inductively Coupled Plasma Analysis to accurately determine the vanadium concentration before diluting it down to a final composition of 0.1 M vanadium in 4 M sulfuric acid. The electrode material, MGL370 (AvCarb), was a $370 \mu\text{m}$ thick carbon paper used as received. For all tests, a saturated calomel (SCE) reference electrode was used, but all published potential values are given with respect to the standard hydrogen reference.

2.2. Cell design and preparation

In this work, two approaches were used to characterize the vanadium redox reactions on porous carbon paper electrodes. The first consists of traditional diffusion controlled cyclic voltammetry and EIS in a stagnant electrolyte. The other approach relies upon

forced convection of electrolyte through the porous electrode to eliminate diffusion effects within the electrode. For stagnant electrolyte tests, the carbon paper working electrode (WE) was positioned at a fixed distance from the reference electrode (RE) and immersed to the same depth in each solution in order to expose the same amount of material to the electrolyte. The 4 mm wide carbon paper strip was immersed roughly 15 mm below the surface of the solution. A 5 mm section of the WE was left dry above the electrolyte after which point the electrode was sandwiched between two graphite board current collectors being held by alligator clips. This was to ensure no contact of the graphite board or alligator clips by the electrolyte when the wetting treatment changes the contact angle between the electrode and electrolyte. For electrodes being treated in a different electrolyte, either VO^{2+}/VO_2^+ or 4 M sulfuric acid, the electrode was transferred after treatment to the solution containing V^{2+}/V^{3+} and immersed to the same depth to perform electrochemical measurements on the same area of the electrode. Graphite felt (Nippon Carbon) with a much greater surface area was heat treated and used as counter electrode (CE).

The flow cell used for forced convective transport of reactants through the internal porous structure of the WE was based on an analytical flow cell concept recently demonstrated by our group [64]. In this case however, the flow cell channel structure was made from a laser machined compressible gasket material sandwiched between two acrylic plates as seen in Fig. 1. Fluid access ports were made for the inlet, outlet, and reference electrode ports which housed the same SCE reference electrode. Graphite current collectors were also embedded in the top clear acrylic plate in order to make electrical contact with the carbon paper WE and CE within the channel. These were sealed with wax and contacted via copper strips. The dimensions of the carbon paper flow-through WE were approximately $1 \text{ mm} \times 3 \text{ mm} \times 370 \mu\text{m}$.

2.3. Electrochemical characterization

All electrochemical measurements were performed using a Biologic VSP potentiostat. Cyclic voltammetry (CV) was performed at 100 mV s^{-1} , while EIS was performed at 10 mV perturbation voltage over the frequency range 200 kHz–0.2 Hz. The linear polarization scan used for Tafel analysis was performed at 3 mV s^{-1} which was verified to be sufficiently slow for steady state polarization values. All potentials published in this study were corrected for IR. For forced convection experiments with the analytical flow cell, reactants were injected and extracted by two syringe pumps (Harvard Apparatus) working in unison at a flow rate of $400 \mu\text{L min}^{-1}$.

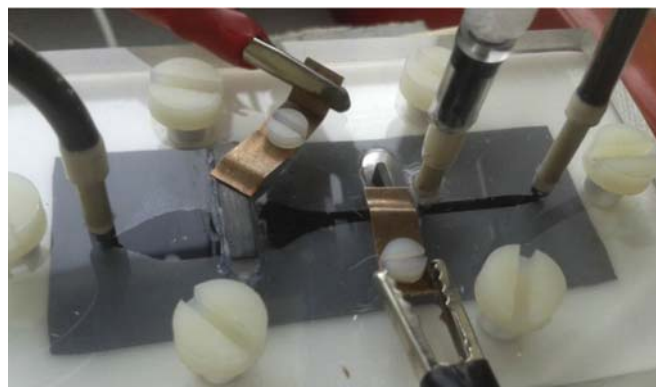


Fig. 1. Three electrode analytical flow cell. (A colour version of this figure can be viewed online.)

3. Results and discussion

The following experiments were performed in order to understand and decouple the phenomenon of porous electrode wetting from its apparent impact on cyclic voltammetry results. The effects of electrochemical and chemical oxidation treatments on the V^{2+}/V^{3+} reaction at carbon paper electrodes were investigated by cyclic voltammetry and EIS with a conventional three electrode cell in a stagnant electrolyte configuration. In addition, a new convection based analytical cell used to eliminate diffusion effects was used to perform Tafel analysis to help understand the effects of the electrode treatments on electrode kinetics.

3.1. Electrochemical oxidation in H_2SO_4

When the carbon paper was initially immersed in a solution of 4 M H_2SO_4 , a layer of trapped gas appeared on its surface, indicative of poor wetting. The effect of electrochemical oxidation on untreated carbon paper was observed by increasing the oxidation limit of voltammetric scans in this solution. As seen in Fig. 2, an electrode cycled ten times at 100 mV s^{-1} between 0.250 and 0.950 V_{SHE} has a relatively stable voltammogram with very small anodic and cathodic currents. Performing a subsequent voltammogram on the same sample, the first cycle up to 1250 mV started along the same current level as the previous scan but followed a much more negative current on the return cathodic scan. During the 2nd and subsequent cycles the separation between the anodic and cathodic currents in the voltammogram increased gradually after each cycle, suggesting that the capacitance of the sample is increasing. In a clear sulfuric acid solution it is possible to visually observe gradual changes occurring at the carbon paper surface whenever the oxidation potential is near 1200 mV, namely the disappearance of the gas bubble layer on the surface. This gas layer, seen in Fig. 3(a), substantially reduces the size of the electrochemical interface and also affects the contact angle (meniscus) between the top of the sample and the surface of the solution. After the 10th cycle, the separation between the anodic and cathodic scans in the voltammogram increased considerably and the majority of the gas layer was removed. Whether the mechanism is purely electrostatic charging, or whether it is electrochemical modification of the carbon surface functional groups, the wettability increases dramatically, which likely leads to similar wetting of the internal pores of the carbon paper and therefore a sizeable increase in the electrochemical interfacial area. This increase in electrochemical surface

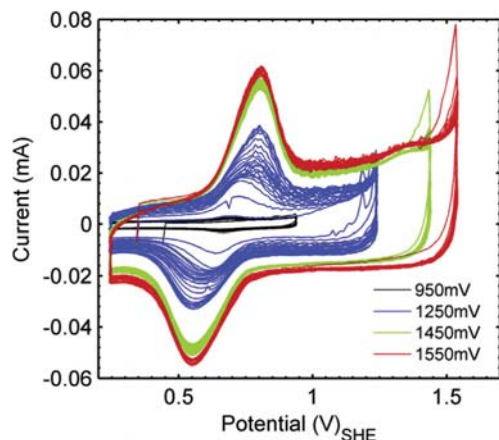


Fig. 2. Ten-cycle CV scans at 100 mV s^{-1} of a carbon paper electrode in a 4 M H_2SO_4 solution with successively greater upper potential limits. (A colour version of this figure can be viewed online.)

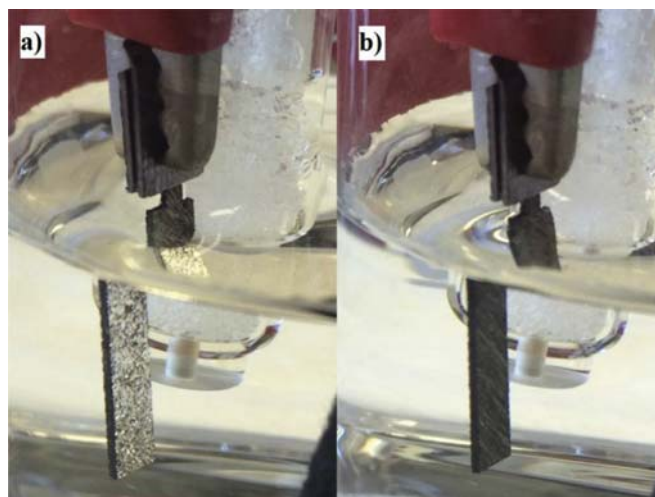


Fig. 3. Carbon paper in sulfuric acid electrolyte a) before and b) after a 0.5 s, 1500 mV anodic oxidation pulse. (A colour version of this figure can be viewed online.)

area (ESA) leads to the higher capacitance seen in Fig. 2. Although this process proceeds slowly around 1200 mV, it can be produced much more quickly by increasing the oxidation potential limit. As an example, the oxidation scans up to 1450 and 1550 mV each demonstrate that the voltammogram width becomes stable after the first cycle and remains roughly the same during the remaining cycles. As such, an average oxidation pulse at 1500 mV was chosen to represent the standard electrochemical oxidation or anodisation treatment. The reduction and oxidation peaks centred at 0.7 V also become larger and more well-defined. In acidic media it has been suggested that these reactions relate to the formation of quinone/hydroquinone functional groups [73,74], but these are not the subject of this study since they seemingly have little effect on the capacitance increase under study (as evidenced by the absence of an effect below 950 mV).

The same effect observed during cyclic voltammetry can be seen more dramatically with a 0.5 s, IR corrected 1500 mV anodic pulse in the 4 M H_2SO_4 solution. As seen in Fig. 3 and in the video attached to Fig. 4, the gas layer on the surface of the carbon paper disappeared entirely after this short pulse treatment and the

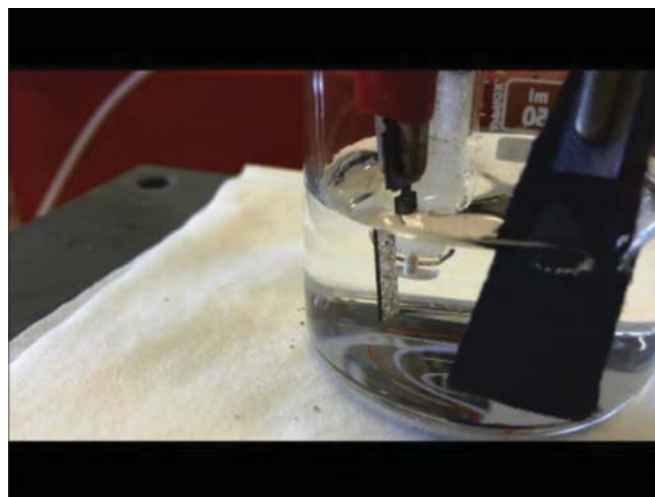


Fig. 4. Video of carbon paper wetting during a 0.5 s, 1550 mV anodic oxidation pulse. (A colour version of this figure can be viewed online.)

contact angle (meniscus) of the carbon with the surface of the electrolyte changed from hydrophobic to hydrophilic. The initial and final capacitance of the carbon paper was measured to be 8 and 140 μF respectively, with subsequent pulsing at the same potential having little measurable effect. This order of magnitude increase seems reasonable considering the extent of the gas layer on the hydrophobic carbon surface. Although oxidation potentials above 1500 mV seemed to further increase the sample capacitance, the effect was only minor compared with the initial increase and may not be permanent for the industrially relevant application under study. Furthermore, higher potentials were not investigated in order to avoid the oxygen evolution reaction which complicates the results due to possible trapped gas bubbles within the porous sample.

Supplementary video related to this article can be found at <http://dx.doi.org/10.1016/j.carbon.2016.02.011>.

3.2. Effect of carbon paper wetting on the $\text{V}^{2+}/\text{V}^{3+}$ reaction

Hydrophilic treatment of carbon paper can be achieved by various methods but here we have concentrated on oxidation pulses in sulfuric acid, in the $\text{V}^{2+}/\text{V}^{3+}$ solution itself, and pre-treatment by immersion in 50% $\text{VO}^{2+}/\text{VO}_2^+$ solution. The effects of these treatments on the $\text{V}^{2+}/\text{V}^{3+}$ reaction were investigated by traditional cyclic voltammetry to reproduce trends similar to those found in the literature. Correlating changes between capacitance and charge transfer resistance with EIS, the source of the CV changes can be more clearly understood. Although more difficult to visualize, the untreated carbon paper has a surface gas layer upon immersion in the $\text{V}^{2+}/\text{V}^{3+}$ solution similar to the case seen in Fig. 3

for sulfuric acid and consequently has roughly the same initial capacitance. As seen in the black curves of Fig. 5-a) and b), the untreated carbon paper has a very high polarization resistance due largely to the minimal wetting of the material and the low ESA. By applying an anodic pulse directly in the $\text{V}^{2+}/\text{V}^{3+}$ solution, the gas layer visually disappears and the capacitance measured via EIS increases from 6 to 90 μF , slightly less than the case in Fig. 3 which was treated and measured in sulfuric acid. In order to verify the source of this effect, the carbon paper was also subjected to an anodic pulse in sulfuric acid and then transferred quickly to the $\text{V}^{2+}/\text{V}^{3+}$ solution to perform EIS and CV. As seen in Fig. 5, the carbon paper anodised in sulfuric acid actually showed more improvement compared to when the same anodic pulse was applied in $\text{V}^{2+}/\text{V}^{3+}$ solution. The difference in wetting was not visually noticeable, but the effect was consistent across several replicates. This is likely due to the $\text{V}^{2+}/\text{V}^{3+}$ species reacting quickly at such a high oxidation potential (1750 mV above the OCP of the redox couple) and thereby utilizing most of the oxidation current for the redox reaction rather than for any surface reactions that affect the wetting process. Immersion of the sample in the oxidizing $\text{VO}^{2+}/\text{VO}_2^+$ solution seemed to have a similar effect on the carbon paper. Although a gas layer was immediately visible upon immersion in $\text{VO}^{2+}/\text{VO}_2^+$, this layer disappeared in less than a minute and the solution eventually wetted the entire immersed carbon paper. The wetted electrode was then dipped into sulfuric acid to remove the $\text{VO}^{2+}/\text{VO}_2^+$ solution from the surface and pores, and then finally dipped to the same depth in $\text{V}^{2+}/\text{V}^{3+}$ solution and tested. It is interesting to note that even though the OCP of the $\text{VO}^{2+}/\text{VO}_2^+$ solution itself was only 1150 mV (vs. SHE) it was equally effective at wetting the carbon paper, leading to CV profiles and EIS results similar to those of the electrode pulsed in sulfuric acid. The in-situ pre-treatment of the electrode materials in readily available oxidizing $\text{VO}^{2+}/\text{VO}_2^+$ would therefore be the most convenient method for vanadium redox battery applications. Contact angle measurements [75] before and after treatment were also considered for comparing different methods of treatment however these did not provide any useful quantitative information due to the fact that all treatments led to the sulfuric acid droplets being absorbed into the carbon paper, making a measurement impossible.

As can be seen from the compiled EIS results in Table 1, the capacitance increase is inversely related to the decrease in R_{ct} for all treatments. This strong correlation indicates that in the case of the porous carbon paper used in this study, the oxidation treatment seems to improve the overall redox reaction rate via an increase in the ESA rather than by any catalytic effect on the intrinsic kinetics of the reaction [76]. As previously mentioned, this type of effect would normally be associated exclusively with an increase in the voltammetric peak currents but it is noteworthy that the treatments also drastically decrease the peak potential separation as well in Fig. 5-a). In most of the vanadium redox battery literature, researchers have often claimed that the different methods mentioned in the introduction can be used to improve the catalytic properties of graphite felts by demonstrating reduced peak separation. For porous materials however, this claim may not necessarily be true. As the electrolyte fills the internal pores of the material, previously unexposed carbon surfaces become surrounded by small pockets of electrolyte. These newly wetted sections, constituting a much larger reaction surface, compete for the same electrolyte reactants in the small pores so that the diffusion layer on the electrode surface within the pores will be different from sections on the surface of the carbon paper which have unconstrained access to the bulk electrolyte. The argument presented here can also be used to interpret some of the studies in the literature which published both CV and EIS data. As an example, the study by Yue et al. [33] purports that the acid treatment of carbon paper improves the kinetics of the

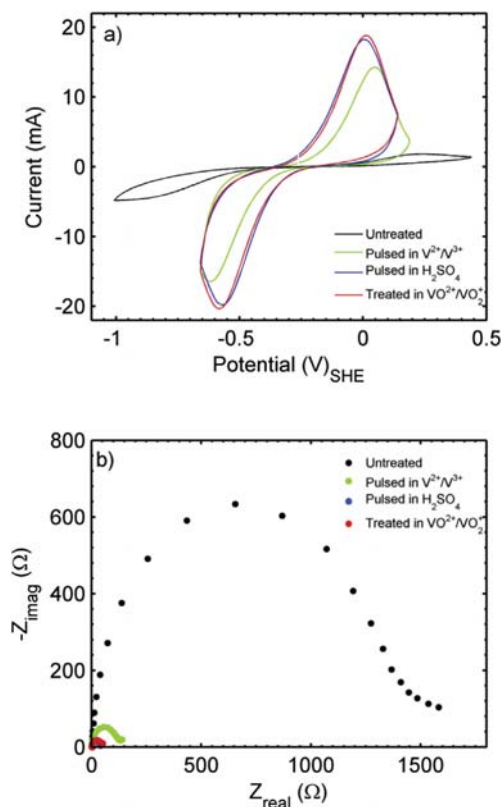


Fig. 5. a) Cyclic voltammograms and b) Nyquist plots of impedance measured for carbon paper in $\text{V}^{2+}/\text{V}^{3+}$ solution in untreated form (black), pulsed in $\text{V}^{2+}/\text{V}^{3+}$ (green), pulsed in sulfuric acid (blue), and pre-treated in $\text{VO}^{2+}/\text{VO}_2^+$ (red). (A colour version of this figure can be viewed online.)

Table 1

Oxidation treatment effects on carbon paper.

Sample type	Untreated	Pulsed in V^{2+}/V^{3+}	Pulsed in H_2SO_4	Treated in VO^{2+}/VO_2^+
Capacitance (μF)	6 ± 1	91 ± 3	142 ± 5	151 ± 7
Capacitance increase (ratio)	NA	15	24	26
R_{ct} (Ω)	1400 ± 200	93 ± 6	54 ± 6	49 ± 4
R_{ct} decrease (ratio)	NA	15	26	29

V^{2+}/V^{3+} reaction by pointing to the reduced cyclic voltammogram peak separation and lower R_{ct} in EIS. What the authors seem to have ignored however, is the increase in the capacitance seen in their study, which indicates as it does in the present study, that the treatment serves primarily to increase the wetted area of the electrode. Several other CV and EIS studies similarly fail to account for the effect of porosity, added surface area, or simply electrode wetting [14,77]. As for the remaining studies on porous materials such as carbon felts which use CV data exclusively; there is insufficient data to conclude anything at all.

Even qualitative interpretation of CV peak separation for highly porous electrode materials is inappropriate, as is proven in Fig. 6. In this experiment, an untreated carbon paper electrode with similar dimensions and adsorbed gas layer was measured by EIS in V^{2+}/V^{3+} to have roughly $6 \mu F$ of capacitance and the same large CV peak separation. The electrode was then placed within a flow channel and the V^{2+}/V^{3+} electrolyte forced through the electrode by syringe. The electrode was then removed from the flow channel and quickly immersed, still wetted, in the same V^{2+}/V^{3+} electrolyte. The increase in peak current attests to the electrolyte wetting the previously inaccessible internal pores of the electrode. As more of the internal pores are wetted however, they compete for smaller pockets of electrolyte and therefore reach their diffusion limited CV peaks earlier. This result demonstrates quite conclusively that for these carbon paper materials, changes in CV curves after thermal, chemical, or electrochemical treatment may not necessarily be due to formation of electroactive sites on the electrode surface. The effect of forced flow is not quite as effective as the other methods for accessing every part of the carbon paper however, increasing the capacitance to only $70 \mu F$ for roughly the same sample dimensions, which leads to a smaller reduction in peak separation. This is not surprising considering that trapped gas bubbles are a common problem in many microfluidic applications and that forced convection is not always sufficient for accessing the smallest pores which would be the first to become diffusion limited during a

linear potential sweep and affect the peak separation the most.

Lastly, it should be noted that the effects seen here were replicated not only on the same carbon paper, but were also largely reproduced on a similar PAN-based carbon fibre paper from a completely different supplier, namely Toray TGP H-120. The similarity of the results (not shown here for brevity) point to the fact that these carbon papers were produced to relatively high standards of quality control for the relevant performance metrics of interest such as conductivity and porosity [78]. This is in stark contrast to the high variability of results observed with graphite felts, as recently expounded by Rabbow et al. [36,37]. This is likely due to their primary function as high temperature thermal insulation for which the electrochemical properties of the surface do not matter. The manufacturing conditions used in the production of these felts could possibly lead to a different surface chemistry with fewer active sites for the vanadium reactions that can in fact be enhanced by surface treatment.

3.3. Transient effects of high potential pulses

As expected, the wetting effects reported in the previous sections are not strictly reversible. Although it is possible to evolve either hydrogen or oxygen gas electrochemically, these reactions tend to generate distinct bubbles that are released from the surface rather than covering it uniformly as in Fig. 3(a). Once this layer is removed, the order of magnitude increase in capacitance mentioned previously is relatively stable over time and is not affected by any applied reduction potential within the hydrogen evolution window. On the other hand, the interaction of the carbon with the electrolyte can also be enhanced beyond this initial wetting by further oxidation. This additional oxidation, which can be accomplished by using electrochemical pulses at higher potentials than those previously employed, is not permanent however. The data in Fig. 7 demonstrates the decay in CV peak currents over the course of 20 cycles after a 1700 mV oxidation pulse in a V^{2+}/V^{3+} solution. The peak currents and capacitance reached initially by this higher oxidation treatment exceed those of samples pulsed at 1500 mV by 10–20%, but the effect is only temporary and tends back towards the wetted steady state behaviour observed in Section 3.2.

The same effects can also be observed with the recently developed analytical flow cell method. The data in Fig. 8 shows the impedance and Tafel behaviour of a smaller carbon paper working electrode under fast convective flow of V^{2+}/V^{3+} reactants. Application of a 1500 mV pulse to the electrode leads to a nearly twofold improvement in both the capacitance and R_{ct} as measured via EIS, and also roughly the same improvement in the Tafel data. This improvement fades over time however, settling to only a 50% improvement in all cases. This small but permanent improvement is likely due to the same situation as in Fig. 6, where the oxidation pulse helps to wet the smallest pores that were not accessible to the forced convective flow of electrolyte. As explained in the original flow cell work, hydrophilic treatment is required to ensure access of reactants to the entire electrode surface [64]. In the case of the brief oxidation pulses used in this study, the mechanism by which this treatment drastically makes the carbon paper hydrophilic is

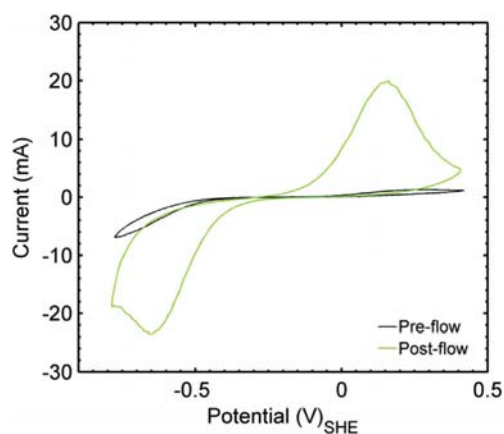


Fig. 6. Cyclic voltammogram at 100 mV s^{-1} on the same sample before and after forced electrolyte injection into the internal pores of the electrode. (A colour version of this figure can be viewed online.)

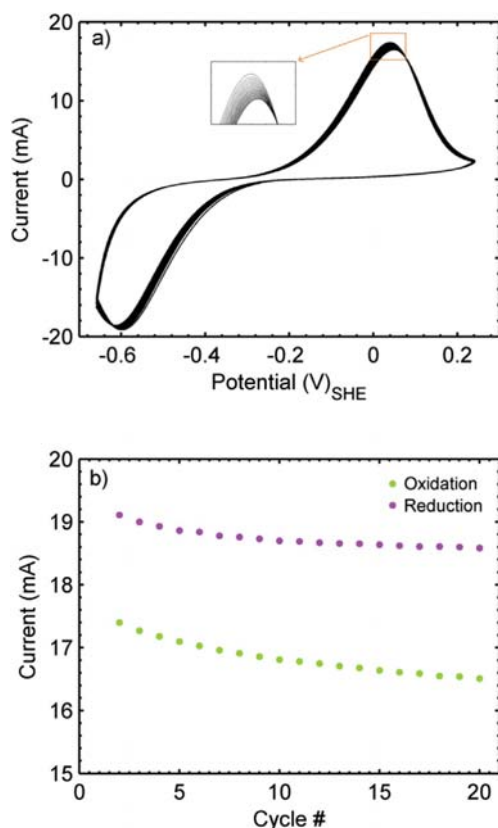


Fig. 7. a) Change in 100 mV s⁻¹ cyclic voltammogram over 20 cycles after a 1700 mV oxidation pulse and b) associated decay in peak currents. (A colour version of this figure can be viewed online.)

unclear. Whether the electrochemical treatment introduces functional groups on the surface of the carbon that provide active sites for the electron transfer reactions, as has been previously suggested [12,79], it is at least capable of conferring a temporary dipole moment to the carbon surface which is sufficient to increase hydrophilicity and induce complete wetting. Although no consistent measurable difference in functional groups was observed via subsequent X-ray photoelectron spectroscopy (XPS) analysis of the carbon paper, the transient effects of higher oxidation potentials observed in both Figs. 7 and 8 do suggest that some form of electrochemical oxidation of the carbon surface beyond the initial wetting is taking place and that this extra surface modification reverts to a reduced form during the cathodic scans over time. Indeed, any attempt to oxidize the surface of the carbon paper to create more surface functional groups is unlikely to endure very long in the highly reducing environment of the V²⁺/V³⁺ solution. Accordingly, it is difficult to imagine why any attempt to oxidize the surface of the electrode would have any long term benefit on the kinetics of the V²⁺/V³⁺ redox couple reaction, since the surface composition would naturally tend towards an equilibrium established by the potential of the electrolyte itself. The effects of electrochemical oxidation and reduction on the kinetics of either vanadium redox couple observed by Bourke et al. [79–81] may be entirely due to the potentials used between tests being very far from the equilibrium of the electrolyte. Although further systematic studies are needed to clarify the effect of surface functional groups on the kinetics of the VO²⁺/VO₂⁺ redox couple reactions, it is likely that those effects are the same transient ones observed here especially given that the positive electrode is also subjected to more negative potentials during discharge of the battery.

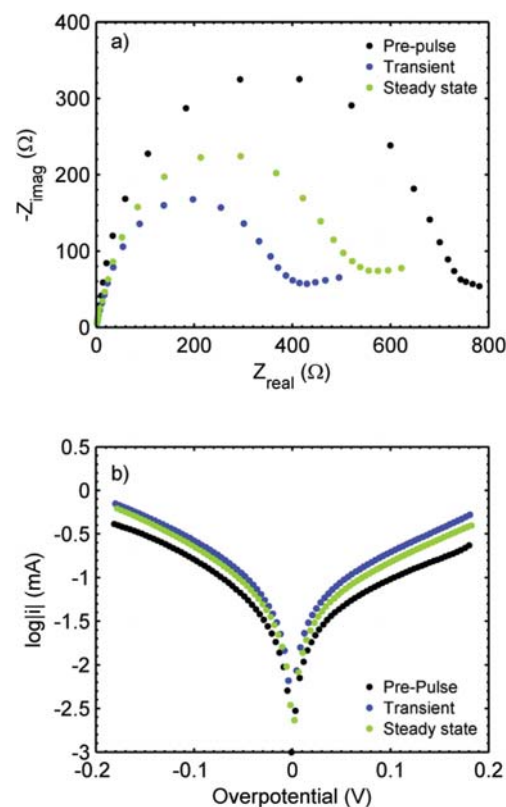


Fig. 8. The effect of a 0.5 s, 1700 mV oxidation pulse in 0.1 M V²⁺/V³⁺ on the a) impedance and b) Tafel polarization of a carbon paper working electrode in an analytical flow cell. (A colour version of this figure can be viewed online.)

3.4. Comparison between V²⁺/V³⁺ and VO²⁺/VO₂⁺ reactions

With a properly wetted electrode it becomes easier to understand differences in electrochemical reaction rates such as those between the V²⁺/V³⁺ and VO²⁺/VO₂⁺ redox couples. In order to achieve equal wetting of the electrode without influencing other factors, the electrode was first tested in VO²⁺/VO₂⁺ and then in V²⁺/V³⁺ in order to duplicate the wetting pre-treatment outlined in Section 3.2. The data in Fig. 9(a) and (b) refer to the same standard electrode being immersed 30 s in a stagnant solution of VO²⁺/VO₂⁺, then rinsed to the same depth in sulfuric acid, and then immersed in V²⁺/V³⁺. In the case of Fig. 9(c), an untreated electrode was placed within the flow cell, tested with VO²⁺/VO₂⁺, rinsed, and then tested again with V²⁺/V³⁺. The data is consistent across all methods, displaying more sluggish kinetics for the V²⁺/V³⁺ reaction, similar to most of the recent literature. In addition, the commonly observed asymmetry between the oxidation and reduction of VO²⁺/VO₂⁺ is also seen here.

Even though the flow distribution within this version of the flow cell was not as uniform as the previously published version and suffers from some mass transport limitations, the Tafel plots roughly reproduce the 2–3x faster reaction rate for VO²⁺/VO₂⁺ seen in the EIS data. Although the disparity between reaction rates is much lower than observed previously, the previous study utilized a commercial grade electrolyte with a different overall composition and different concentrations of reactants. While the qualitative relationships reported here are self-consistent, they could further benefit from the previously published microfabrication techniques in order to get quantitatively precise data from the flow cell method.

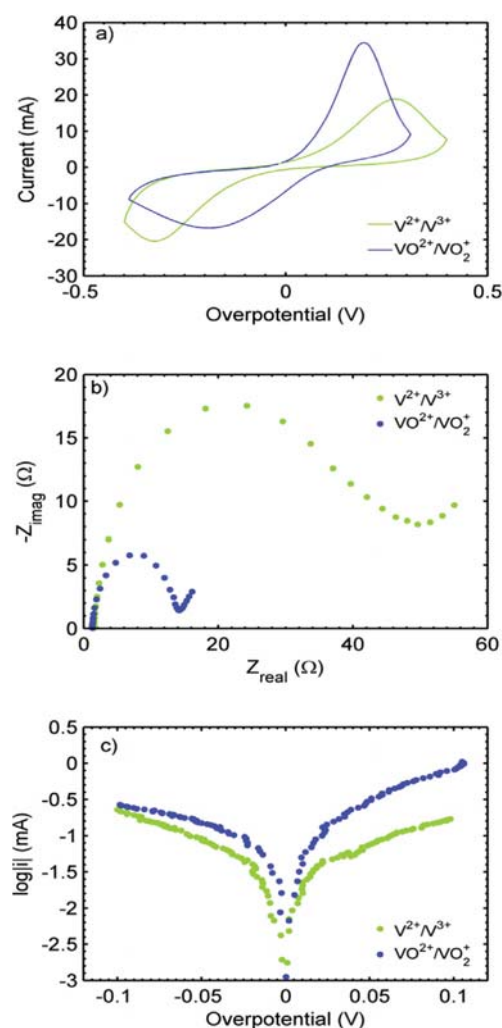


Fig. 9. Comparison between $\text{VO}_2^+/\text{VO}_2^+$ and $\text{V}^{2+}/\text{V}^{3+}$ kinetics (after carbon paper pre-treatment with $\text{VO}_2^+/\text{VO}_2^+$). (A colour version of this figure can be viewed online.)

4. Conclusions

A rigorous experimental investigation into the issues surrounding reaction rate discrepancies in the vanadium redox battery literature was performed. For the porous carbon paper materials being evaluated in this work, it was found that the combination of porosity and variable wetting of the material can have a considerable impact on the perceived relationship between the reaction kinetics of both the $\text{V}^{2+}/\text{V}^{3+}$ and $\text{VO}_2^+/\text{VO}_2^+$ redox couples. Moreover, it was demonstrated that the cyclic voltammetry method most commonly applied in the literature cannot be relied upon to draw any meaningful conclusions about the reaction kinetics on these electrodes. In particular, peak separation in cyclic voltammetry was demonstrated to be a poor indicator of changes in intrinsic reaction rates by forced flow of electrolyte through the porous carbon paper. Attention to details such as IR correction and proper wetting of the porous surface are essential to this diffusion based technique. Other methods such as EIS and flow cell techniques which eliminate diffusion interference must be used in conjunction with cyclic voltammetry in order to extract either qualitative or quantitative data. These techniques were used to establish how both electrochemical (by application of a 1500 mV pulse) and chemical (via immersion in a $\text{VO}_2^+/\text{VO}_2^+$ solution) oxidation of a carbon paper electrode lead to more complete

wetting of the paper in a $\text{V}^{2+}/\text{V}^{3+}$ electrolyte and consequently an increase in the interfacial surface area and capacitance. This capacitance increase was shown to be concomitant and proportional to an increase in the rate of the $\text{V}^{2+}/\text{V}^{3+}$ redox reactions. Application of higher oxidation potentials (>1500 mV) was shown to further increase the capacitance and electrode kinetics but that this added effect is transient and fades over time in the $\text{V}^{2+}/\text{V}^{3+}$ solution. Overall, the results observed in this work suggest that further comparative studies of a range of carbon papers and felts with a similarly thorough methodology are needed to elucidate these phenomena in order to establish a suitable specification for electrode material selection and/or pre-treatment for redox flow battery applications.

Acknowledgements

Funding for this research provided by the Natural Sciences and Engineering Research Council of Canada (NSERC), Western Economic Diversification Canada, Canada Foundation for Innovation, British Columbia Knowledge Development Fund, and Simon Fraser University (SFU) is highly appreciated. The Australian Department of Education and Training is kindly acknowledged for the sponsorship provided by the Australia Endeavour program. We thank Dr. Da-Wei Wang and Dr. Stuart Prescott at UNSW for their generous contribution of equipment, and to Paul Brockbank, Liu Yue Cao, and Yi Feng Li for their technical support.

References

- [1] Z. Yang, J. Zhang, M.C.W. Kintner-Meyer, X. Lu, D. Choi, J.P. Lemmon, et al., Electrochemical energy storage for green grid, *Chem. Rev.* 111 (2011) 3577–3613.
- [2] A.Z. Weber, M.M. Mench, J.P. Meyers, P.N. Ross, J.T. Gostick, Q. Liu, Redox flow batteries: a review, *J. Appl. Electrochem* 41 (2011) 1137–1164.
- [3] M. Skyllas-Kazacos, New all-vanadium redox flow cell, *J. Electrochem. Soc.* 133 (1986) 1057–1058.
- [4] M. Skyllas-Kazacos, M.H. Chakrabarti, S.A. Hajimolana, F.S. Mjalli, M. Saleem, Progress in flow battery research and development, *J. Electrochem. Soc.* 158 (2011) R55–R79.
- [5] E. Sum, M. Skyllas-Kazacos, A study of the $\text{V(II)}/\text{V(III)}$ redox couple for redox flow cell applications, *J. Power Sources* 15 (1985) 179–190.
- [6] E. Sum, M. Rychcik, M. Skyllas-Kazacos, Investigation of the $\text{V(V)}/\text{V(IV)}$ system for use in the positive half-cell of a redox battery, *J. Power Sources* 16 (1985) 85–95.
- [7] M. Skyllas-Kazacos, M. Kazacos, State of charge monitoring methods for vanadium redox flow battery control, *J. Power Sources* 196 (2011) 8822–8827.
- [8] M. Skyllas-Kazacos, Efficient vanadium redox flow cell, *J. Electrochem. Soc.* 134 (1987) 2950.
- [9] J.W. Lee, M.-A. Goulet, E. Kjeang, Microfluidic redox battery, *Lab. Chip* 13 (2013) 2504–2507.
- [10] M. Skyllas-Kazacos, D. Kasherman, D.R. Hong, M. Kazacos, Characteristics and performance redox battery of 1 kW UNSW vanadium, *J. Power Sources* 35 (1991) 399–404.
- [11] P. Zhao, H. Zhang, H. Zhou, J. Chen, S. Gao, B. Yi, Characteristics and performance of 10 kW class all-vanadium redox-flow battery stack, *J. Power Sources* 162 (2006) 1416–1420.
- [12] B. Sun, M. Skyllas-Kazacos, Modification of graphite electrode materials for vanadium redox flow battery application—I. thermal treatment, *Electrochim. Acta* 37 (1992) 1253–1260.
- [13] B. Sun, M. Skyllas-Kazacos, Chemical modification of graphite electrode materials for vanadium redox flow battery application—part II. acid treatments, *Electrochim. Acta* 37 (1992) 2459–2465.
- [14] P. Han, Y. Yue, Z. Liu, W. Xu, L. Zhang, H. Xu, et al., Graphene oxide nanosheets/multi-walled carbon nanotubes hybrid as an excellent electrocatalytic material towards $\text{VO}_2^+/\text{VO}_2^+$ redox couples for vanadium redox flow batteries, *Energy Environ. Sci.* 4 (2011) 4710.
- [15] H.Q. Zhu, Y.M. Zhang, L. Yue, W.S. Li, G.L. Li, D. Shu, et al., Graphite-carbon nanotube composite electrodes for all vanadium redox flow battery, *J. Power Sources* 184 (2008) 637–640.
- [16] G. Wei, C. Jia, J. Liu, C. Yan, Carbon felt supported carbon nanotubes catalysts composite electrode for vanadium redox flow battery application, *J. Power Sources* 220 (2012) 185–192.
- [17] G. Wei, X. Fan, J. Liu, C. Yan, Electrospun carbon nanofibers/electrocatalyst hybrids as asymmetric electrodes for vanadium redox flow battery, *J. Power Sources* 281 (2015) 1–6.
- [18] S. Wang, X. Zhao, T. Cochell, A. Manthiram, Nitrogen-doped carbon nanotube/

- graphite felt as advanced electrode materials for vanadium redox flow batteries, *J. Phys. Chem. Lett.* 3 (2012) 2164–2167.
- [19] W. Li, J. Liu, C. Yan, The electrochemical catalytic activity of single-walled carbon nanotubes towards VO²⁺/VO²⁺ and V³⁺/V²⁺ redox pairs for an all vanadium redox flow battery, *Electrochim. Acta* 79 (2012) 102–108.
 - [20] W. Li, J. Liu, C. Yan, Multi-walled carbon nanotubes used as an electrode reaction catalyst for VO²⁺ for a vanadium redox flow battery, *Carbon N. Y.* 49 (2011) 3463–3470.
 - [21] Z. González, P. Álvarez, C. Blanco, S. Vega-Díaz, F. Tristán-López, L.P. Rajukumar, et al., The influence of carbon nanotubes characteristics in their performance as positive electrodes in vanadium redox flow batteries, *Sustain. Energy Technol. Assess.* 9 (2015) 105–110.
 - [22] L. Shi, S. Liu, Z. He, J. Shen, Nitrogen-doped graphene: effects of nitrogen species on the properties of the vanadium redox flow battery, *Electrochim. Acta* 138 (2014) 93–100.
 - [23] Y. Shao, X. Wang, M. Engelhard, C. Wang, S. Dai, J. Liu, et al., Nitrogen-doped mesoporous carbon for energy storage in vanadium redox flow batteries, *J. Power Sources* 195 (2010) 4375–4379.
 - [24] M. Park, J. Ryu, Y. Kim, J. Cho, Corn protein-derived nitrogen-doped carbon materials with oxygen-rich functional groups: a highly efficient electrocatalyst for all-vanadium redox flow batteries, *Energy Environ. Sci.* 7 (2014) 3727–3735.
 - [25] J. Jin, X. Fu, Q. Liu, Y. Liu, Z. Wei, K. Niu, et al., Identifying the active site in nitrogen-doped graphene for the VO(2+)/VO2(+) redox reaction, *ACS Nano* 7 (2013) 4764–4773.
 - [26] Z. He, A. Su, C. Gao, Z. Zhou, C. Pan, S. Liu, Carbon paper modified by hydrothermal ammoniated treatment for vanadium redox battery, *Ionics (Kiel)* 19 (2013) 1021–1026.
 - [27] Z. He, L. Shi, J. Shen, Z. He, S. Liu, Effects of nitrogen doping on the electrochemical performance of graphite felts for vanadium redox flow batteries, *Int. J. Energy Res.* 39 (2015) 709–716.
 - [28] C. Flox, J. Rubio-García, M. Skoumal, T. Andreu, J.R. Morante, Thermo-chemical treatments based on NH₃/O₂ for improved graphite-based fiber electrodes in vanadium redox flow batteries, *Carbon N. Y.* 60 (2013) 280–288.
 - [29] T. Wu, K. Huang, S. Liu, S. Zhuang, D. Fang, S. Li, et al., Hydrothermal ammoniated treatment of PAN-graphite felt for vanadium redox flow battery, *J. Solid State Electrochem* 16 (2012) 579–585.
 - [30] E.-M. Hammer, B. Berger, L. Komsysiaka, Improvement of the performance of graphite felt electrodes for vanadium-redox-flow-batteries by plasma treatment, *Int. J. Renew. Energy Dev.* 3 (2014) 7–12.
 - [31] Z. González, C. Botas, P. Álvarez, S. Roldán, C. Blanco, R. Santamaría, et al., Thermally reduced graphite oxide as positive electrode in vanadium redox flow batteries, *Carbon N. Y.* 50 (2012) 828–834.
 - [32] W. Zhang, J. Xi, Z. Li, H. Zhou, L. Liu, Z. Wu, et al., Electrochemical activation of graphite felt electrode for VO²⁺/VO²⁺ + redox couple application, *Electrochim. Acta* 89 (2013) 429–435.
 - [33] L. Yue, W. Li, F. Sun, L. Zhao, L. Xing, Highly hydroxylated carbon fibres as electrode materials of all-vanadium redox flow battery, *Carbon N. Y.* 48 (2010) 3079–3090.
 - [34] X. Wu, H. Xu, P. Xu, Y. Shen, L. Lu, J. Shi, et al., Microwave-treated graphite felt as the positive electrode for all-vanadium redox flow battery, *J. Power Sources* 263 (2014) 104–109.
 - [35] X. Wu, H. Xu, Y. Shen, P. Xu, L. Lu, J. Fu, et al., Treatment of graphite felt by modified hummers method for the positive electrode of vanadium redox flow battery, *Electrochim. Acta* 138 (2014) 264–269.
 - [36] T.J. Rabbow, M. Trampert, P. Pokorny, P. Binder, A.H. Whitehead, Variability within a single type of polyacrylonitrile-based graphite felt after thermal treatment. part I: physical properties, *Electrochim. Acta* 173 (2015) 17–23.
 - [37] T.J. Rabbow, M. Trampert, P. Pokorny, P. Binder, A.H. Whitehead, Variability within a single type of polyacrylonitrile-based graphite felt after thermal treatment. part II: chemical properties, *Electrochim. Acta* 173 (2015) 24–30.
 - [38] N. Pour, D.G. Kwabi, T.J. Carney, R.M. Darling, M.L. Perry, Y. Shao-Horn, Influence of edge- and basal-plane sites on the vanadium redox kinetics for flow batteries, *J. Phys. Chem. C* (2015), 150216172359004.
 - [39] J. Melke, P. Jakes, J. Langner, L. Riekehr, U. Kunz, Z. Zhao-Karger, et al., Carbon materials for the positive electrode in all-vanadium redox flow batteries, *Carbon N. Y.* 8 (2014).
 - [40] W. Li, J. Liu, C. Yan, Reduced graphene oxide with tunable C/O ratio and its activity towards vanadium redox pairs for an all vanadium redox flow battery, *Carbon N. Y.* 55 (2013) 313–320.
 - [41] K.J. Kim, Y.J. Kim, J.H. Kim, M.S. Park, The effects of surface modification on carbon felt electrodes for use in vanadium redox flow batteries, *Mater. Chem. Phys.* 131 (2011) 547–553.
 - [42] C. Gao, N. Wang, S. Peng, S. Liu, Y. Lei, X. Liang, et al., Influence of Fenton's reagent treatment on electrochemical properties of graphite felt for all vanadium redox flow battery, *Electrochim. Acta* 88 (2013) 193–202.
 - [43] C. Flox, M. Skoumal, J. Rubio-García, T. Andreu, J.R. Morante, Strategies for enhancing electrochemical activity of carbon-based electrodes for all-vanadium redox flow batteries, *Appl. Energy* 109 (2013) 344–351.
 - [44] A. Di Blasi, O. Di Blasi, N. Briguglio, A.S. Arico, D. Sebastián, M.J. Lázaro, et al., Investigation of several graphite-based electrodes for vanadium redox flow cell, *J. Power Sources* 227 (2013) 15–23.
 - [45] A.M. Pezeshki, J.T. Clement, G.M. Veith, T.A. Zawodzinski, M.M. Mench, High performance electrodes in vanadium redox flow batteries through oxygen-enriched thermal activation, *J. Power Sources* 294 (2015) 333–338.
 - [46] H. Zhou, J. Xi, Z. Li, Z. Zhang, L. Yu, L. Liu, et al., CeO₂ decorated graphite felt as a high-performance electrode for vanadium redox flow batteries, *RSC Adv.* 4 (2014) 61912–61918.
 - [47] X. Wu, H. Xu, L. Lu, H. Zhao, J. Fu, Y. Shen, et al., PbO₂-modified graphite felt as the positive electrode for an all-vanadium redox flow battery, *J. Power Sources* 250 (2014) 274–278.
 - [48] T.-M. Tseng, R.-H. Huang, C.-Y. Huang, K.-L. Hsueh, F.-S. Shieu, Improvement of titanium dioxide addition on carbon black composite for negative electrode in vanadium redox flow battery, *J. Electrochem. Soc.* 160 (2013) A1269–A1275.
 - [49] T.-M. Tseng, R.-H. Huang, C.-Y. Huang, C.-C. Liu, K.-L. Hsueh, F.-S. Shieu, Carbon felt coated with titanium dioxide/carbon black composite as negative electrode for vanadium redox flow battery, *J. Electrochem. Soc.* 161 (2014) A1132–A1138.
 - [50] H.M. Tsai, S.J. Yang, C.C.M. Ma, X. Xie, Preparation and electrochemical activities of iridium-decorated graphene as the electrode for all-vanadium redox flow batteries, *Electrochim. Acta* 77 (2012) 232–236.
 - [51] Y. Shen, H. Xu, P. Xu, X. Wu, Y. Dong, L. Lu, Electrochemical catalytic activity of tungsten trioxide-modified graphite felt toward VO²⁺/VO²⁺ + redox reaction, *Electrochim. Acta* 132 (2014) 37–41.
 - [52] B. Li, M. Gu, Z. Nie, Y. Shao, Q. Luo, X. Wei, et al., Bismuth nanoparticle decorating graphite felt as a high-performance electrode for an all-vanadium redox flow battery, *Nano Lett.* 13 (2013) 1330–1335.
 - [53] B.T. Sun, M. Skyllas-Kazacos, Chemical modification and electrochemical behaviour of graphite fibre in acidic vanadium solutions, *Electrochim. Acta* 36 (1991) 513–517.
 - [54] X. Wu, S. Liu, N. Wang, S. Peng, Z. He, Influence of organic additives on electrochemical properties of the positive electrolyte for all-vanadium redox flow battery, *Electrochim. Acta* 78 (2012) 475–482.
 - [55] M. Skyllas-Kazacos, Evaluation of precipitation inhibitors for supersaturated vanadyl electrolytes for the vanadium redox battery, *Electrochem. Solid-State Lett.* 2 (1999) 121.
 - [56] S. Li, K. Huang, S. Liu, D. Fang, X. Wu, D. Lu, et al., Effect of organic additives on positive electrolyte for vanadium redox battery, *Electrochim. Acta* 56 (2011) 5483–5487.
 - [57] H. Kaneko, K. Nozaki, Y. Wada, T. Aoki, A. Negishi, M. Kamimoto, Vanadium redox reactions and carbon electrodes for vanadium redox flow battery, *Electrochim. Acta* 36 (1991) 1191–1196.
 - [58] S. Zhong, M. Skyllas-Kazacos, Electrochemical behaviour of vanadium(V)/Vanadium(IV) redox couple at graphite electrodes, *J. Power Sources* 39 (1992) 1–9.
 - [59] M. Gattrell, J. Park, B. MacDougall, J. Apte, S. McCarthy, C.W. Wu, Study of the mechanism of the vanadium 4+/5+ redox reaction in acidic solutions, *J. Electrochem. Soc.* 151 (2004) A123.
 - [60] J.W. Lee, J.K. Hong, E. Kjeang, Electrochemical characteristics of vanadium redox reactions on porous carbon electrodes for microfluidic fuel cell applications, *Electrochim. Acta* 83 (2012) 430–438.
 - [61] D. Aaron, C.-N. Sun, M. Bright, A.B. Papandrew, M.M. Mench, T.A. Zawodzinski, In situ kinetics studies in all-vanadium redox flow batteries, *ECS Electrochem. Lett.* 2 (2013) A29–A31.
 - [62] T. Yamamura, N. Watanabe, T. Yano, Y. Shiohara, Electron-transfer kinetics of Np³⁺ / Np⁴⁺, NpO²⁺ / NpO₂²⁺, V²⁺ / V³⁺, and VO²⁺ / VO²⁺ at carbon electrodes, *J. Electrochem. Soc.* 152 (2005) A830.
 - [63] G. Oriji, Y. Katayama, T. Miura, Investigations on V(IV)/V(V) and V(II)/V(III) redox reactions by various electrochemical methods, *J. Power Sources* 139 (2005) 321–324.
 - [64] M.-A. Goulet, M. Eikerling, E. Kjeang, Direct measurement of electrochemical reaction kinetics in flow-through porous electrodes, *Electrochem. Commun.* 57 (2015) 14–17.
 - [65] R.S. Nicholson, Theory and application of cyclic voltammetry: measurement of electrode reaction kinetics, *Anal. Chem.* 37 (1965) 1351–1355.
 - [66] P. Delahay, Theory of irreversible waves in oscillographic polarography, *J. Am. Chem. Soc.* 75 (1953) 1190–1196.
 - [67] E.O. Barnes, X. Chen, P. Li, R.G. Compton, Voltammetry at porous electrodes: a theoretical study, *J. Electroanal. Chem.* 720–721 (2014) 92–100.
 - [68] K.R. Ward, R.G. Compton, Quantifying the apparent “Catalytic” effect of porous electrode surfaces, *J. Electroanal. Chem.* 724 (2014) 43–47.
 - [69] D. Menshkykau, I. Streeter, R.G. Compton, Influence of electrode roughness on cyclic voltammetry, *J. Phys. Chem. C* 112 (2008) 14428–14438.
 - [70] D. Menshkykau, R.G. Compton, The influence of electrode porosity on diffusional cyclic voltammetry, *Electroanalysis* 20 (2008) 2387–2394.
 - [71] I. Streeter, G.G. Wildgoose, L. Shao, R.G. Compton, Cyclic voltammetry on electrode surfaces covered with porous layers: an analysis of electron transfer kinetics at single-walled carbon nanotube modified electrodes, *Sens. Actuators B Chem.* 133 (2008) 462–466.
 - [72] M. Kazacos, M. Skyllas-Kazacos, High Energy Density Vanadium Electrolyte Solutions, Methods of Preparation Thereof and All-vanadium Redox Cells and Batteries Containing High Energy Density Vanadium Electrolyte Solutions, 2006.
 - [73] V. Ruiz, C. Blanco, E. Raymundo-Piñero, V. Khomenko, F. Béguin, R. Santamaría, Effects of thermal treatment of activated carbon on the electrochemical behaviour in supercapacitors, *Electrochim. Acta* 52 (2007) 4969–4973.
 - [74] W. Ma, Y.-T. Long, Quinone/hydroquinone-functionalized biointerfaces for biological applications from the macro- to nano-scale, *Chem. Soc. Rev.* 43

- (2014) 30–41.
- [75] J. Haußmann, F. Wilhelm, S. Enz, M. Klages, A. Pournemat, C. Bergbreiter, et al., GDL and MPL characterization and their relevance to fuel cell modelling, *ECS Trans.* 69 (2015) 1279–1291.
- [76] J. Friedl, C.M. Bauer, A. Rinaldi, U. Stimming, Electron transfer kinetics of the $\text{VO}_2^+/\text{VO}^{2+}$ reaction on multi-walled carbon nanotubes, *Carbon N. Y.* 63 (2013) 228–239.
- [77] J. Shen, S. Liu, Z. He, L. Shi, Influence of antimony ions in negative electrolyte on the electrochemical performance of vanadium redox flow batteries, *Electrochim. Acta* 151 (2015) 297–305.
- [78] R. Schweiss, Influence of bulk fibre properties of PAN-based carbon felts on their performance in vanadium redox flow batteries, *J. Power Sources* 278 (2015) 308–313.
- [79] A. Bourke, N. Quill, R.P. Lynch, D.N. Buckley, Effect of polarization treatment on $\text{V(II)}/\text{V(III)}$ and $\text{V(IV)}/\text{V(V)}$ kinetics at carbon electrodes, *ECS Trans.* 64 (2015) 1–17.
- [80] A. Bourke, N. Quill, R.P. Lynch, D.N. Buckley, Effect of pretreatment on the rate of the $\text{VO}_2^+/\text{VO}_2$ + and $\text{V}^{2+}/\text{V}^{3+}$ reactions at a carbon electrode, *ECS Trans.* 61 (2014) 15–26.
- [81] A. Bourke, R.P. Lynch, D.N. Buckley, Effect of electrode pretreatment on the cyclic voltammetry of $\text{VO}_2^+/\text{VO}_2$ + at a glassy carbon electrode, *ECS Trans.* 53 (2013) 59–67.

Appendix E.

In situ enhancement of flow-through porous electrodes with carbon nanotubes via flowing deposition



In Situ Enhancement of Flow-through Porous Electrodes with Carbon Nanotubes via Flowing Deposition



Marc-Antoni Goulet¹, Aronne Habisch, Erik Kjeang^{1,*}

School of Mechatronic Systems Engineering, Simon Fraser University, 250-13450 102 Avenue, Surrey, BC V3T 0A3, Canada

ARTICLE INFO

Article history:

Received 18 February 2016

Received in revised form 19 April 2016

Accepted 25 April 2016

Available online 26 April 2016

Keywords:

Flow-through porous electrode

Deposition

Carbon nanotube

Electrochemical surface area

Kinetics

ABSTRACT

This study describes a novel flowing deposition method which can be used *in situ* on a fully assembled electrochemical cell to enhance the electrochemical active surface area of flow-through porous electrodes. As a test case, vanadium redox reaction rates are enhanced by flowing deposition of carbon nanotubes on carbon paper electrodes. The deposition is characterized using a recently developed analytical flow cell technique and shown to increase the electrochemical active surface area and therefore the exchange current for the limiting V^{2+}/V^{3+} reaction by over an order of magnitude. When applied to the anode of an assembled vanadium redox flow cell, the method nearly eliminates the overpotential associated with this reaction, thereby significantly improving the power output of the cell by up to 70% in the high voltage efficiency regime. As a surface area treatment, this flowing deposition method could be used to similarly enhance the energy conversion efficiency of many other electrochemical flow cells such as fuel cells, flow batteries and capacitive deionization cells.

© 2016 Elsevier Ltd. All rights reserved.

1. Introduction

In a bid to develop efficient and compact electrochemical energy conversion devices much attention has been devoted toward increasing the electrochemical surface area per unit volume of electrode. Whether for batteries, fuel cells, or capacitors, electrodes with nanoscopic features and porosity are necessary to achieve the highest energy and power densities [1,2]. Among the options available for conductive electrode materials, carbon continues to be principal due to its low cost, chemical resistance, and potentially high surface area [3]. As an inexpensive and abundant material, natural carbon has typically been processed into high surface area particles for electrochemical applications such as activated carbon for electrosorption [4,5] or carbon black as a catalyst support in fuel cells [6]. As a randomly aggregated electrode material these powders require some form of structural support which may interfere with the mass transport of reactants. In addition, amorphous natural carbon with a low degree of graphitization suffers from poor electrical conductivity which is exacerbated by high contact resistance between particles when packed too loosely [7]. A more synthetic approach to manufacturing carbon materials with large active surface area per unit volume

has involved pyrolysis of polymer precursors with a desired architecture and pore size distribution such as woven cloths, felts, papers, or foams [8,9]. Commercial vanadium redox flow batteries which do not require catalysts still rely upon graphite felt as electrodes with a recent trend toward more compact carbon papers made from pyrolyzed polyacrylonitrile (PAN) fibers [10,11]. Typically composed of micrometer sized fibers, these materials albeit fall short of the range needed to support the current densities required by modern energy applications. To attain the ideal nanometer scale pore size distribution while maintaining good electrical conductivity, many recent efforts have been made toward the development of carbon nanofoams [12,13]. With a well-connected carbon structure providing an unbroken electrical pathway, custom pore sizes can be achieved by a template process leading to potentially very high surface area [13,14]. Unfortunately these materials typically suffer from poor mechanical properties such as brittleness and micrometer-sized cracks which skew their overall pore size distribution [15].

One of the most common methods for increasing the active electrode area has been through the synthesis or deposition of high surface area nanomaterials onto a scaffold such as the powders, felts, and papers mentioned above [16]. In the case of metallic catalysts, electrodeposition has been used to synthesize an array of colourfully named nanoscale geometries with very high surface area such as onions and nanoflowers [17]. Most often these nanoparticles are deposited on supporting mesoscopic carbon

* Corresponding author. Tel.: +1 778 782 8791; fax: +1 778 782 7514.
E-mail address: ekjeang@sfu.ca (E. Kjeang).

¹ ISE member.

powders and dispersed as inks for physical deposition. Depending on the design of the final cell and the reaction chemistry involved, these catalyst inks have been physically deposited with an array of methods including doctor-blading [18], immersion [19], spray coating [20], and inkjet printing [21]. Other methods of catalyst deposition such as sputtering and chemical and physical vapor deposition are unlikely to be adopted commercially due to their higher cost. More recently, synthesized carbon nanomaterials such as graphene and carbon nanotubes (CNTs) have received much interest as electrode materials and catalyst supports due to their exceptionally high surface area. In addition, their ordered graphitic structure endows them with high electrical conductivity and mechanical strength [22]. In the case of chemistries which do not rely on precious metal catalysts such as the vanadium redox battery, these nanomaterials have the potential to greatly increase the electrochemical active surface area (ESA) of a supporting carbon electrode such as graphite felt or carbon paper [23–31].

In this study a novel method is described for increasing the ESA of flow-through porous electrodes while addressing the issue of cost reduction. In its present incarnation, the invention consists of *in situ* flowing deposition of carbon nanotubes (CNT) onto a carbon paper scaffold which increases the surface area available for electrochemical reactions [32]. With few steps and no added chemicals or solvents this method provides a simple and environmentally benign way of increasing the performance of electrochemical cells based on flow-through porous electrodes. In the current example, the performance improvement related to the increased surface area is quantified via half-cell electrochemical impedance spectroscopy (EIS) in addition to standard Tafel analysis with the use of an analytical flow cell technique. The deposition method is also demonstrated *in situ* by enhancing the performance of a previously assembled full electrochemical cell for discharge of vanadium redox reactants. The flowing deposition of CNTs is used to increase the surface area of the anode of the cell to offset the slower intrinsic kinetics of the V^{2+}/V^{3+} reaction in particular. The deposition aims to effectively eliminate the kinetic overpotential associated with this reaction in terms of overall device performance.

2. Methodology

2.1. Device fabrication

Assessing the kinetic performance of compact high surface area electrodes which are inherently porous has repeatedly been shown to be prone to error [33–37]. Porosity and surface roughness introduce artificial effects which cannot easily be extracted from polarization data, making it difficult to evaluate both the nanomaterials and deposition methods being used [38,39]. A recent study released by our group has suggested a new analytical flow cell technique for quantifying the kinetics of flow through porous electrodes in particular [40]. This technique uses a customized microfluidic channel to force reactants through the electrode at rates high enough to compensate for diffusion limitations. The analytical flow cell has already proven useful for determining which vanadium half-cell reaction is limiting on carbon paper electrodes and the effect of electro-oxidation on the rate of the V^{2+}/V^{3+} reaction in particular [41].

In the present work, the previously published three electrode analytical flow cell depicted in Fig. 1a is used for half-cell ESA characterization and initial analysis of the flow deposition method [40]. Additionally, for the purpose of demonstrating *in situ* deposition in a full electrochemical cell, the previously published co-laminar flow cell (CLFC) depicted in Fig. 1b is used [42]. This new class of electrochemical cell is based on membraneless co-laminar flow to achieve reactant separation and has been extensively reviewed elsewhere [43,44]. The microfluidic channels for these cells are fabricated by soft lithography of poly (dimethylsiloxane) (PDMS) from a photoresist template. The analytical flow cell consists of a single inlet and outlet with a uniform channel height of 150 μm to compress the electrodes and a channel width of 2 mm in the upstream WE section which gradually expands to a 4 mm width in the downstream CE section. The active section of the WE is therefore 2 mm wide, with a flow-through depth of 0.5 mm. The CE is sized with a flow-through depth of 4 mm to provide an order of magnitude larger ESA than the WE. Once the electrodes are placed within their respective grooves, the cell is capped by a glass slide and pressure sealed by a customized clamp. Contact is made with the electrodes which

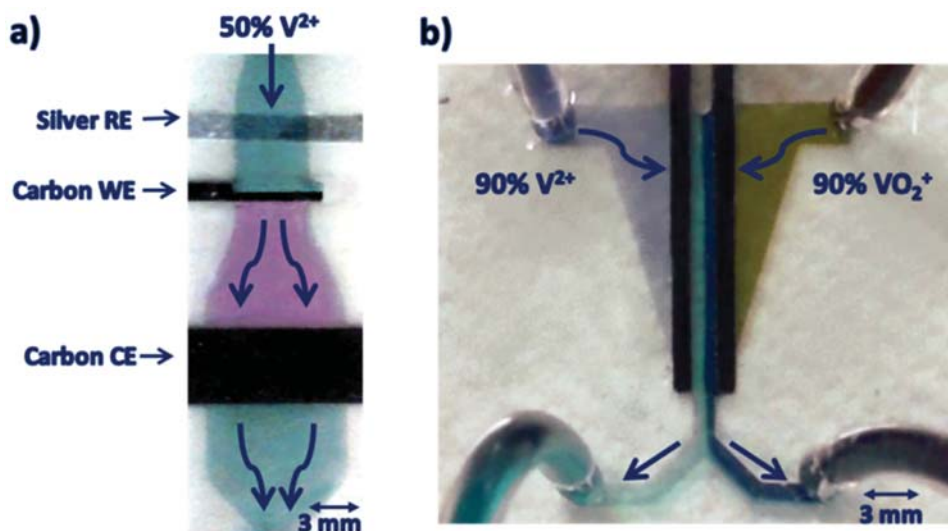


Fig. 1. Annotated live images of a) the analytical flow cell during complete oxidation of 50% V^{2+} on the upstream working electrode and subsequent complete reduction on the downstream counter electrode [40] and b) the co-laminar flow cell discharging 90% vanadium reactants. The colour changes observed are indicative of the different vanadium ion oxidation states and hence show effective reactant conversion in each flow-through porous electrode [42].

extend beyond the cell via copper clips. The co-laminar flow cell on the other hand has two identical electrodes with 1 mm flow-through depth and an active length of 10 mm compressed to a similar 150 μm channel height through which the reactants are pumped. The cell is more permanently bonded by plasma treatment of the PDMS and glass slide cap layer [45].

2.2. Materials

The reactants in this study are the $\text{V}^{2+}/\text{V}^{3+}$ and $\text{VO}^{2+}/\text{VO}_2^+$ redox couples prepared by charging a commercial grade 1.7 M vanadium in 4 M sulfuric acid stock solution with a conventional flow battery. For the purpose of studying the kinetics of the limiting reaction, the microfluidic analytical flow cell in Fig. 1a is operated with a 50% state of charge (SOC) $\text{V}^{2+}/\text{V}^{3+}$ solution in order to have equal concentrations of reductant and oxidant. The negative equilibrium potential of this redox couple ($-0.255 \text{ V}_{\text{SHE}}$) permits the use of a silver foil as reference electrode (RE), with 180 μm thick Toray carbon paper (TGP 060) with a specific surface area of roughly $4 \text{ m}^2 \cdot \text{g}^{-1}$ serving as both the working electrode (WE) and counter electrode (CE) as described in the original study [40]. For discharge performance tests, the CLFC shown in Fig. 1 uses the same carbon paper electrodes with both $\text{V}^{2+}/\text{V}^{3+}$ and $\text{VO}^{2+}/\text{VO}_2^+$ reactants charged to roughly 90% SOC, representative of typical battery discharge operation. In all cases the carbon paper electrodes are

heat treated to increase hydrophilicity. The multi-walled carbon nanotubes (CNT) for electrode enhancement purchased from Cheap Tubes Inc. are 10–50 μm in length and $<10 \text{ nm}$ in outer diameter. A very dilute temporary suspension of these CNTs in deionized water is prepared by sonication for one hour and injected immediately afterwards through the carbon paper inside the microfluidic cell. The carbon paper electrodes are rinsed forcefully with deionized water to remove loosely deposited CNTs before being used with vanadium reactants.

2.3. Characterization

Two syringe pumps (Harvard Apparatus MA1 70-2209) are operated in unison at flow rates ranging from 2 to 400 $\mu\text{L} \cdot \text{min}^{-1}$ to inject the reactants into the inlets and remove them from the outlets of either cell. All polarization measurements are made with a potentiostat (Gamry Reference 3000) operating at voltammetric scan rates slow enough to ensure steady state conditions. Electrochemical impedance spectroscopy (EIS) measurements are conducted at 10 mV perturbation from the open circuit potential (OCP) at 1–300 000 Hz to determine the impedance of the cells. All Tafel plots are IR corrected by extracting the effects of ohmic resistance in order to display only the relevant kinetics, whereas ohmic effects are preserved for all polarization data during discharge of the co-laminar flow cell to demonstrate

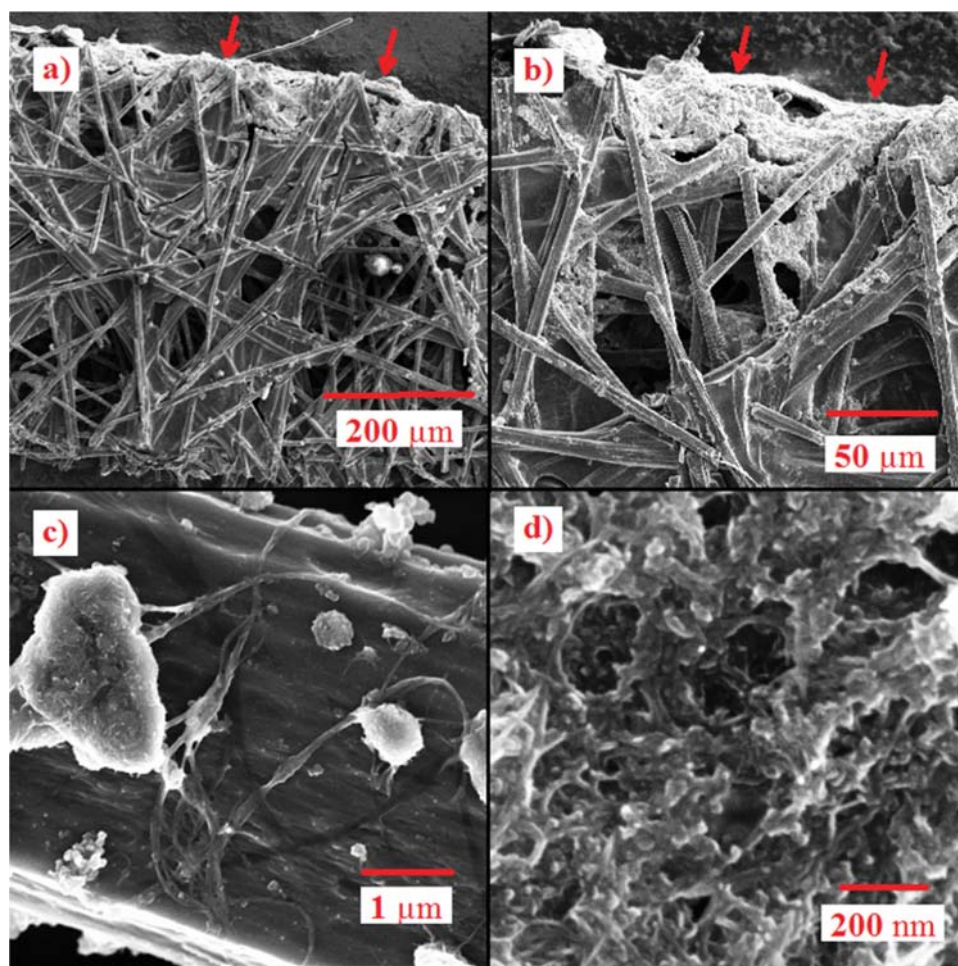


Fig. 2. Scanning electron microscope images of flowing CNT deposition on a porous carbon paper electrode where red arrows indicate flow direction: a) full electrode width; b) blanketing layer of CNTs at the electrode entrance; c) individual CNT fiber bundles and amorphous agglomerates adsorbed on a single carbon fiber; and d) nanoscale amorphous CNT agglomerate structure.

genuine overall performance improvements. The capacitance of the WE in the analytical cell is determined via Simplex method fitting with Echem Analyst software (Gamry), where the goodness of fit was below 2×10^{-3} in all cases [38]. The pressure drop from inlet to outlet was measured by a pressure transducer (Honeywell HSCMRRN001PDAA5) placed in parallel with the fluidic circuit with the output read by a source meter (Keithley 2400).

3. Results and discussion

This work proposes a novel flow-through deposition method for CNTs on carbon paper electrodes in order to increase the ESA and kinetic rates of flow-through porous electrodes used in electrochemical cells. The effectiveness of the CNT deposition is quantified with the microfluidic analytical cell technique recently published by the authors supported by corroborating evidence from EIS [40]. Additionally, the performance of a co-laminar flow cell for discharge of vanadium redox reactants is assessed by both EIS and polarization data before and after *in situ* deposition of CNTs on the anode of the cell. Lastly, the effect of the added CNTs on the pressure drop through the enhanced electrode is measured via pressure transducer.

3.1. Flowing CNT deposition

The goal for deposition of electroactive material on flow-through porous electrodes is to distribute the deposited material as uniformly as possible where reactant flow is most likely. This is accomplished naturally by *in situ* flowing deposition which ensures deposition of electroactive material where reactants are being converted during flow-through operation of the cell. For the vanadium redox reactions under investigation in this study, carbon nanotubes were chosen as the electroactive deposition material for their high surface area and conductivity. Without hydrophilic surface functionalization, carbon nanoparticles and nanotubes do not form stable suspensions in aqueous solutions, but rather phase separate into macroscopic agglomerates [46]. Although stable suspensions have been achieved by the addition of solvents to help solvate the nanoparticles, this method was found to interfere with the reactions used in this study. In addition, the omission of solvents reduces the complexity and cost of the deposition and satisfies the growing need for 'greener' chemical processes. The proposed flowing deposition method is based on the simple idea of maximizing the time before agglomeration such that the deposition procedure can be completed [32]. This is accomplished by preparation of a very dilute suspension of carbon nanotubes in deionized water to decrease the probability of carbon nanotube interactions. Sonication of the mixture leads to a temporary suspension in which CNT fiber bundles can be visually observed to agglomerate over the course of an hour. When the temporary suspension is injected into the analytical flow cell depicted in Fig. 1a, some of the CNTs become lodged within and at the entrance to the carbon paper working electrode, while others pass through the electrode and are either deposited at the thicker counter electrode or may potentially reach the outlet. In this sense, the upstream working electrode acts as a first filter for the suspension simply through Van der Waals interactions between the scaffold material and the deposition material. As more of the suspension is injected, a dark layer forms at the entrance to the working electrode which is composed of agglomerated CNTs as seen in Fig. 2a. The scanning electron microscope (SEM) images in Fig. 2 depict the different structures formed by the CNTs during the deposition. The top down view in Fig. 2a shows the overall structure of a 500 μm wide carbon paper electrode after deposition of CNTs in the analytical flow cell. The carbon paper, with 7 μm diameter carbon fibers connected by sections of pyrolyzed binder,

serves as a supporting scaffold for the deposited CNTs primarily distributed at the upstream side of the paper. A magnified view of the upper section is provided in Fig. 2b which shows the CNTs blanketing the surface of the carbon paper which acted as the electrode inlet for the incoming flow of CNTs. A detailed view of one of the carbon fibers in Fig. 2c illustrates the two primary structures encountered during these experiments, namely randomly amalgamated amorphous clumps of CNTs and self-assembled CNT fiber bundles which seem to attach themselves to the larger carbon paper fibers. It is highly likely that these physically adhered, naturally occurring CNT bundles provide the mechanical support required for this deposition method to provide stable electrode enhancement during electrolyte flow without the need for additional binder materials. It should be noted that the filtration or deposition process is only semi-stable however. When pressure fluctuations or pulsations are imposed on the analytical cell, deposited CNT agglomerates can be seen to detach from the working electrode. Reversing the flow direction can even dislodge the blanketing layer at the entrance of the working electrode. This type of instability can lead to considerable variation in the performance data. For this reason, a thorough rinsing step was implemented after each deposition step involving flow of pure deionized water in order to retain only the most firmly attached CNTs. This was verified by repeating polarization measurements during continuous flow of reactants. Accordingly, all polarization data presented in this study is based upon those repetitions which did not vary significantly over time and therefore representative of stable operation. It should be noted however that the stability of every deposition step is not synonymous with reproducibility; i.e., a thoroughly rinsed agglomeration of CNTs may be stable but is unique. Lastly, it is interesting to note that the amorphous section seen in Fig. 2d which is the primary form of the blanketing layer at the inlet of the electrode has a nanoporous structure. This is a desirable feature for flow-through porous electrodes with potential for increased ESA and reaction rates.

3.2. Quantitative characterization of electrode enhancement

In order to accurately evaluate the electrode enhancement of the flowing deposition method, the original carbon paper scaffold electrode is placed within a three electrode analytical flow cell to characterize the impedance and polarization of the electrode under both quiescent and convective electrolyte conditions, respectively. As previously discussed, the deposition method consists of injecting a temporary suspension of CNTs through the working electrode, followed by a rinsing step before testing the EIS and Tafel behavior of the electrode in a $\text{V}^{2+}/\text{V}^{3+}$ electrolyte. This process is repeated four times by adding 0.1 ml of suspension in each successive deposition step.

The Nyquist plots in Fig. 3a demonstrate a distinct reduction in charge transfer resistance (R_{ct}) after each deposition step until the final step when no significant change is observed. It should be noted that the high frequency ohmic resistance of the electrode, which is used for post-run IR correction of polarization data, remains constant throughout the experiment. The improvements in reaction rate measured via the EIS perturbation method are further supported by standard Tafel analysis with the analytical flow cell technique recently developed by our group [40]. After each EIS measurement in quiescent electrolyte, the cell is operated at a high flow rate of 400 $\mu\text{L}\cdot\text{min}^{-1}$ in order to minimize mass transport effects. In conjunction with a small electrode depth, the high flow rate leads to conversion below 5% for the $\text{V}^{2+}/\text{V}^{3+}$ reactants in this experiment, thereby ensuring predominantly kinetic control. This is also substantiated by the fact that the linear Tafel slopes in Fig. 3b are within 30 $\text{mV}\cdot\text{dec}^{-1}$ of the theoretical value for a one electron transfer reaction in the absence of diffusion

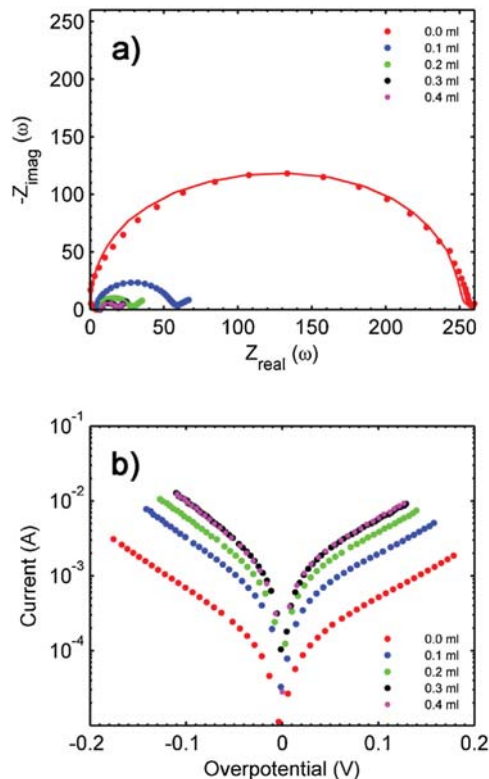


Fig. 3. Analytical flow cell characterization of 50% V^{2+}/V^{3+} redox reactions on a carbon paper electrode enhanced by four successive CNT deposition steps: a) Nyquist plot of impedance data (points) with associated curve fits (lines); and b) Tafel plots.

[40]. In agreement with the EIS data, the Tafel measurements display similar improvements in reaction rate as seen by the increase in exchange current determined by the y-intercept of the Tafel slopes. As with the EIS data, the largest relative improvement occurs during the first deposition step, with diminishing returns as the procedure is repeated. It should also be noted that the deposition process was continued beyond 0.4 ml with little measurable effect. This could be due to the deposition process reaching a saturation point in the stability of adhered CNTs, with additional CNTs being too weakly bound to the carbon paper scaffold to resist being washed out during the rinsing step. Nevertheless, as seen in Fig. 4, both Tafel analysis and EIS indicate that the method is capable of enhancing the baseline reaction rate of this electrode by over an order of magnitude. With no significant change in the Tafel slopes in Fig. 3b there is no reason to believe that the mechanism for the V^{2+}/V^{3+} reaction changes during the deposition procedure. Indeed, the data in Fig. 4a shows a clear linear relationship between the electrode capacitance and charge transfer resistance, which suggests that the increase in reaction rate is solely due to an increase in ESA, rather than any change in the intrinsic kinetics of the reaction. Similarly, the exchange current measured in Fig. 3b should also increase proportionally to the ESA, as described in a similar study by Friedl et al. [38]. In addition, the slope of proportionality between the charge transfer resistance and the exchange current should follow the low-field approximation of the Butler-Erdey-Gruz-Volmer (BE-GV) expression for a one electron transfer:

$$I_0 = \frac{RT}{F} R_{ct}^{-1}$$

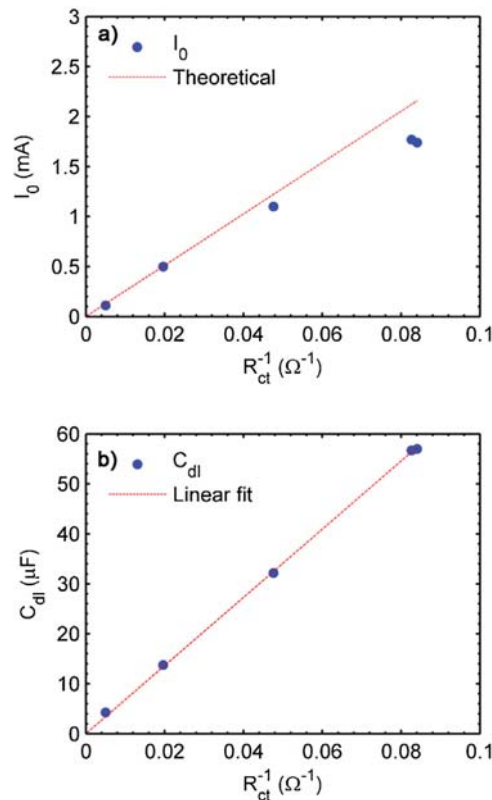


Fig. 4. Effect of CNT deposition on R_{ct}^{-1} and the correlated increase in a) exchange current and b) capacitance of the carbon paper electrode in V^{2+}/V^{3+} electrolyte. The point closest to the origin represents the untreated carbon paper, with successive CNT deposition steps from Fig. 3 located progressively further from the origin.

where R is the universal gas constant, T is the temperature, and F is Faraday's constant. This theoretical relationship has been added to Fig. 4b to highlight the results from the deposition. The exchange current measured for the baseline carbon paper and the first deposition step fall directly on the theoretical line, indicating that the EIS and Tafel techniques are consistent and interchangeable. As the deposition continues the exchange current increases, but also deviates slightly from the theoretical line. Even though the Tafel slopes for the higher deposition levels do not display any significant mass transport effects, these could still be present and would decrease the measured exchange current as observed here. Although the blanket layer of deposited CNTs at the entrance to the electrode in Fig. 2b is relatively uniform, there will inevitably be variability in the deposition which influences the pore size distribution and thereby the local flow velocity. It is conceivable that some sections of the nanoporous structure of the deposited layer are not being replenished with reactants as quickly as others. It should also be noted that small differences in Tafel fitting on a log scale can produce large variation in the exchange current on a linear scale. Most notably, the very high current produced by the enhanced carbon paper electrode requires increasingly large IR correction which restricts the feasible overpotential range, making the linear fit less precise. Nevertheless, both techniques demonstrate the capability of the proposed deposition method to considerably increase the electrochemically active surface area of flow-through porous electrodes. From the capacitance and charge transfer resistance data, this increase was measured to be 15x, whereas the exchange current increased by 13x.

3.3. In situ flow cell enhancement

The following *in situ* experiment is designed to enhance the surface area of the anode electrode of the co-laminar flow cell depicted in Fig. 1b as a proof-of-concept of *in situ* electrode enhancement in a complete electrochemical flow cell device used for energy conversion. This is achieved by pumping the temporarily suspended CNTs through that electrode, while pumping only deionized water through the other electrode. The high flow rate ($1000 \mu\text{L}\cdot\text{min}^{-1}$) ensures that the two streams meet in the center channel and flow toward the outlet without crossing over to the other side [42]. After rinsing both sides of the cell with deionized water, the CLFC is then operated as a fuel cell or discharging flow battery by pumping 90% V^{2+} through the anode and 90% VO_2^+ through the cathode. As a two electrode cell with kinetically different reactants on each side, the charge transfer portion of the Nyquist plot of impedance shown in Fig. 5 displays a combination of two semicircles, with the less visible higher frequency smaller semicircle corresponding to the faster $\text{VO}_2^+/\text{VO}_2^+$ redox reaction while the lower frequency greater semicircle relates to the more sluggish $\text{V}^{2+}/\text{V}^{3+}$ reaction. As explained in the previous section, the inverse of the charge transfer resistance is proportional to the rate of reaction and therefore inherently linked to the ESA of the electrode with the limiting reaction. By increasing the area of the anode, it is expected that the charge transfer resistance of the cell will decrease, whereas depositing CNTs on the cathode where the faster $\text{VO}_2^+/\text{VO}_2^+$ reaction occurs should have no significant effect. This behavior was observed when a large quantity of CNTs was deposited on the cathode with no measurable change in the R_{ct} of the cell. The same quantity was then deposited on the anode, leading to an appreciable decrease in R_{ct} . This result can be taken as further evidence that $\text{V}^{2+}/\text{V}^{3+}$ is the limiting reaction for the vanadium redox battery chemistry with these carbon materials [40,41]. The Nyquist plot portrayed in Fig. 5 illustrates the effect of incremental CNT deposition steps on the limiting anode. As before, the cell is rinsed with water between each deposition step and then operated with charged reactants to measure both polarization and EIS behavior. As expected, the larger $\text{V}^{2+}/\text{V}^{3+}$ semicircle which determines the R_{ct} of the cell decreases with each deposition step until the point where the Nyquist plot resembles a single semicircle, indicating similar kinetics for both electrodes. This demonstrates that the deposition treatment can effectively compensate for the sluggish kinetics of the $\text{V}^{2+}/\text{V}^{3+}$ reaction. As in the analytical flow cell case, the CNT deposition has no effect on

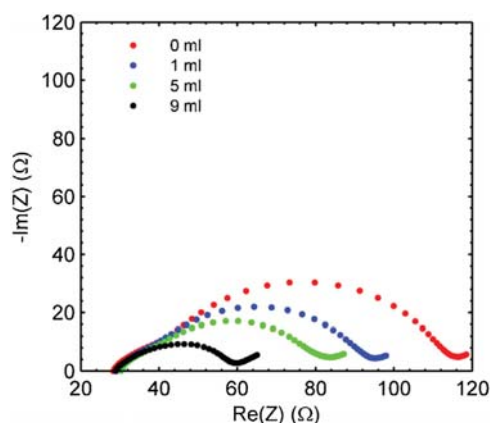


Fig. 5. Nyquist plot of impedance for the co-laminar flow cell subjected to *in situ* anode electrode enhancement by flowing deposition of CNTs in successive steps (as indicated in terms of the total suspension volume applied).

the high frequency intercept of the Nyquist plot, indicating that the ohmic resistance of the cell has not changed.

Increasing the surface area of the limiting electrode reduces the activation or kinetic overpotential of this reaction and therefore the polarization behavior of the entire cell improves. The trend observed in the EIS data can also be seen in the cell polarization curves of Fig. 6a. In the same way that the charge transfer resistance improves incrementally, the kinetic region in the polarization curves improve incrementally as well, leading to greater overall current at a given cell voltage. With no effect on the ohmic resistance of the cell, the linear section of the polarization curve should not change appreciably, but there is a slight improvement in this section which may indicate that the mass transport of reactants has been improved as well. Indeed, the nanoporosity of the deposited CNT layer may reduce the concentration overpotential of the electrode and further boost the performance. At high power output typically relevant for fuel cells, the enhancement of the anode with 9 ml of injected temporary CNT suspension leads to a 23% increase in the maximum power density of the cell as shown in Fig. 6b. At $100 \mu\text{L}\cdot\text{min}^{-1}$ this enhanced cell produced a maximum power of 10.4 mW, equivalent to roughly $700 \text{ mW}\cdot\text{cm}^{-2}$ when normalized by the electrode area cross-sectional to the flow and $2330 \text{ mW}\cdot\text{cm}^{-3}$ when normalized by the total volume of the electrochemical chamber (both electrodes and center channel) as recently recommended for this technology [43]. It was also observed that further deposition of CNTs on the anode had no measurable effect, indicating that the cathode was likely now limiting the reaction rate.

As a surface area enhancement however, the value of the flowing deposition treatment is more clearly evident in the low current density kinetic regime typically relevant for high energy efficiency operation. As shown in Fig. 7, up to 70% improvement in

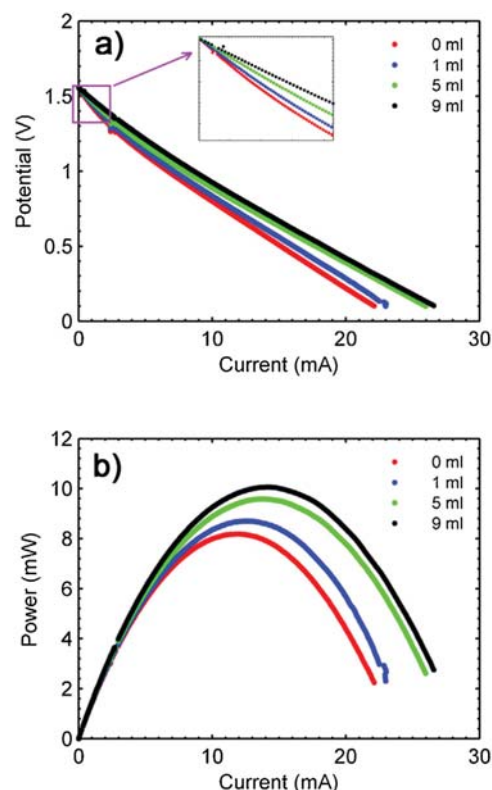


Fig. 6. *In situ* a) polarization and b) power curves of a co-laminar flow cell subjected to successive CNT deposition steps on the anode.

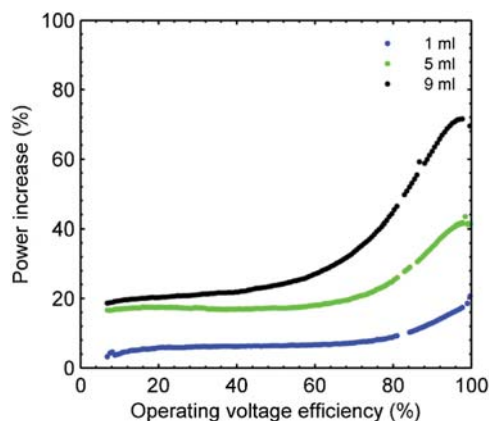


Fig. 7. Power increase due to successive *in situ* CNT deposition steps on the anode.

power was achieved in this cell solely by compensating for the sluggish kinetics of the V^{2+}/V^{3+} reaction. As an example, an operating voltage of 1.4 V leads to a voltage efficiency of 90% for this system. At this operating point, the 9 ml deposition enhancement leads to 62% more current or power. Depending on the application, this improvement could be exploited for reducing the overall system size and cost by the same factor. This is why cost-effective elimination of the kinetic overpotential is generally the first and most important step towards energy efficient cell design. Once this has been achieved, as in the present example, ohmic losses are likely to dominate the cell performance at low to medium current densities. As an effective *in situ* technique for enhancing existing flow-through porous electrodes, the method demonstrated in this work will allow for thinner electrodes which will in turn reduce the area specific resistance of conventional sandwich structure cells [10,11].

Lastly, it is important to understand what effect the deposition of a nanoporous CNT layer may have on the overall operation of the cell. In particular, it may be expected that the added pressure required for pumping reactants through smaller pore sizes may substantially decrease the net power gained by this deposition method. Previous modeling investigations have suggested that the power lost to pumping requirements is quite minimal (<1%) even for flow-through porous electrodes, but without experimental evidence [47,48]. The data displayed in Fig. 8 shows the measured pressure versus flow rate relationship for the incremental stages of electrode enhancement discussed thus far. To the authors'

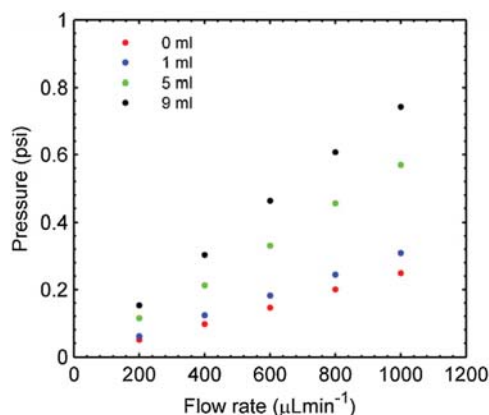


Fig. 8. Pressure drop between the anode inlet and outlet of the co-laminar flow cell subjected to successive steps of CNT deposition.

knowledge, these are the first experimental measurements of the pumping pressure required for operation of a microfluidic co-laminar flow cell. As expected from Darcy's law for flow through porous media, the increase in pressure is linear in all cases with respect to the change in flow rate. For the baseline cell with no enhancement, the experimental values for the pressure are in good agreement with a previous modeling study on a similar cell design with flow-through porous electrodes [47]. Comparing the required pressures at each flow rate, the fully enhanced electrode with 9 ml of deposition treatment consistently requires 3x the pumping pressure of the baseline electrode. When these pressures are converted into pumping power however, the power lost is insignificant to the power gained. For the single electrode measured, the pumping power $P = \dot{Q}\Delta p$ equates to roughly 0.001 mW for the baseline case and 0.003 mW for the fully enhanced case at a flow rate of $100 \mu\text{L}\cdot\text{min}^{-1}$. This negligible change is less than 1% of the power output, even in the low current density kinetic regime typically used as an operating point for high efficiency electrochemical cells.

3.4. Discussion

The method developed in this study has several industrial advantages over other deposition methods described in the literature. Without any solvents, the only material cost is the substance being deposited. Depending on the nature of the deposited substance, this makes the process more environmentally benign by avoiding toxic solvents which may require special handling or disposal procedures. Although demonstrated with carbon nanotubes, the method could be applied with other nanomaterials that have the potential to adhere, either physically by Van der Waals forces or chemically by surface functionalization, to the electrode of interest. In addition, the method is generalizable to many flow based electrochemical cells such as redox flow batteries, liquid fuel cells, capacitive deionizers for water treatment, etc. [49] Moreover, the method can be applied to these types of cells *in situ* to enhance the electrochemical active surface area of their electrodes where it is most needed during operation. Though the surface area enhancement is expected to partially wash out over time, the flowing deposition treatment could potentially be reapplied to recover optimal performance without opening the cell as demonstrated here. One drawback of the method is the difficulty in quantifying the amount of material being deposited, though this is unlikely to be important for commercial purposes since it is reasonable to assume that the method would always be applied to achieve a maximum level of enhancement as in the case described in this work.

4. Conclusions

In this work, a novel technique and results pertaining to the characterization and enhancement of electrochemical cells based on flow-through porous electrodes have been presented. Using a temporary aqueous suspension of carbon nanotubes, a novel deposition method was developed involving the pressure driven flow of this suspension through a porous carbon paper electrode. The deposition distribution was observed via SEM to produce a primary agglomerated layer of CNTs at the upstream entrance to the carbon paper with more scattered agglomerates of deposited CNTs within the carbon paper. Nanoscale carbon nanotube fiber bundles were also observed to physically adhere to the microscale carbon paper fibers. This deposition of nanotubes was characterized electrochemically with a new technique involving a microfluidic analytical cell and shown to increase the capacitance and exchange current density of a carbon paper electrode by over an

order of magnitude in a V^{2+}/V^{3+} electrolyte. The flowing deposition method was then used *in situ* in an assembled co-laminar flow cell to similarly increase the electrochemical active surface area and kinetic rates of the anode. The enhancement of the anode produced an increase in power density of the co-laminar flow cell as high as 70% when operated with V^{2+}/V^{3+} and VO^{2+}/VO_2^+ reactants at $100 \mu\text{L}\cdot\text{min}^{-1}$. The pressure drop through the modified electrode was also observed to increase but only negligibly in comparison to the overall power gained. Overall, the proposed flow deposition method could potentially be applied to a wide range of electrochemical cells in order to enhance both power output and energy conversion efficiency.

Acknowledgements

Funding for this research provided by the Natural Sciences and Engineering Research Council of Canada, Western Economic Diversification Canada, Canada Foundation for Innovation, British Columbia Knowledge Development Fund, and Simon Fraser University is highly appreciated.

References

- [1] A. Jänes, H. Kurig, E. Lust, Characterisation of activated nanoporous carbon for supercapacitor electrode materials, *Carbon* N. Y. 45 (2007) 1226–1233, doi: <http://dx.doi.org/10.1016/j.carbon.2007.01.024>.
- [2] S.H. Joo, S.J. Choi, I. Oh, J. Kwak, Z. Liu, O. Terasaki, et al., Ordered nanoporous arrays of carbon supporting high dispersions of platinum nanoparticles, *Nature* 412 (2001) 169–172, doi: <http://dx.doi.org/10.1038/35106621>.
- [3] F. Rodríguez-reinoso, The role of carbon materials in heterogeneous catalysis, *Carbon* N. Y. 36 (1998) 159–175, doi: [http://dx.doi.org/10.1016/S0008-6223\(97\)00173-5](http://dx.doi.org/10.1016/S0008-6223(97)00173-5).
- [4] G.J.W. Nataraj, J. Cox, R.G.A. Wills, F.C. Walsh, Electrochemical characterisation of activated carbon particles used in redox flow battery electrodes, *J. Power Sources* 185 (2008) 1499–1504, doi: <http://dx.doi.org/10.1016/j.jpowsour.2008.08.020>.
- [5] S.Y. Qian, B.E. Conway, G. Jerkiewicz, Electrochemical sorption of H into Fe and mild-steel: kinetic conditions for enhancement or inhibition by adsorbed HS-, *Phys. Chem. Chem. Phys.* 1 (1999) 2805–2813, doi: <http://dx.doi.org/10.1039/a901369e>.
- [6] E. Antolini, E.R. Gonzalez, Polymer supports for low-temperature fuel cell catalysts, *Appl. Catal. A Gen.* 365 (2009) 1–19, doi: <http://dx.doi.org/10.1016/j.apcata.2009.05.045>.
- [7] D. Pantea, H. Darmstadt, S. Kaliaguine, C. Roy, Electrical conductivity of conductive carbon blacks: Influence of surface chemistry and topology, *Appl. Surf. Sci.* 217 (2003) 181–193, doi: [http://dx.doi.org/10.1016/S0169-4332\(03\)00550-6](http://dx.doi.org/10.1016/S0169-4332(03)00550-6).
- [8] S.K. Nataraj, K.S. Yang, T.M. Aminabhavi, Polyacrylonitrile-based nanofibers—A state-of-the-art review, *Prog. Polym. Sci.* 37 (2012) 487–513, doi: <http://dx.doi.org/10.1016/j.progpolymsci.2011.07.001>.
- [9] A.L. Dicks, The role of carbon in fuel cells, *J. Power Sources* 156 (2006) 128–141, doi: <http://dx.doi.org/10.1016/j.jpowsour.2006.02.054>.
- [10] D.S. Aaron, Q. Liu, Z. Tang, G.M. Grim, A.B. Papandrew, A. Turhan, et al., Dramatic performance gains in vanadium redox flow batteries through modified cell architecture, *J. Power Sources* 206 (2012) 450–453, doi: <http://dx.doi.org/10.1016/j.jpowsour.2011.12.026>.
- [11] Q.H. Liu, G.M. Grim, A.B. Papandrew, A. Turhan, T.A. Zawodzinski, M.M. Mench, High Performance Vanadium Redox Flow Batteries with Optimized Electrode Configuration and Membrane Selection, *J. Electrochem. Soc.* 159 (2012) A1246–A1252, doi: <http://dx.doi.org/10.1149/2.051208jes>.
- [12] A.L.M. Reddy, S.R. Gowda, M.M. Shaijumon, P.M. Ajayan, Hybrid nanostructures for energy storage applications, *Adv. Mater.* 24 (2012) 5045–5064, doi: <http://dx.doi.org/10.1002/adma.201104502>.
- [13] S. Chabi, C. Peng, D. Hu, Y. Zhu, Ideal three-dimensional electrode structures for electrochemical energy storage, *Adv. Mater.* 26 (2014) 2440–2445, doi: <http://dx.doi.org/10.1002/adma.201305095>.
- [14] M. Depardieu, R. Janot, C. Sanchez, A. Bentaleb, C. Gervais, M. Birot, et al., Carbonaceous multiscale-cellular foams as novel electrodes for stable, efficient lithium–sulfur batteries, *RSC Adv.* 4 (2014) 23971, doi: <http://dx.doi.org/10.1039/c4ra03110e>.
- [15] J.W. Lee, E. Kjeang, Nanofluidic Fuel Cell, *J. Power Sources* 242 (2013) 472–477, doi: <http://dx.doi.org/10.1016/j.jpowsour.2013.05.129>.
- [16] S. Litster, G. McLean, PEM fuel cell electrodes, *J. Power Sources* 130 (2004) 61–76, doi: <http://dx.doi.org/10.1016/j.jpowsour.2003.12.055>.
- [17] H. Jiang, P.S. Lee, C. Li, 3D carbon based nanostructures for advanced supercapacitors, *Energy Environ. Sci.* 6 (2013) 41–53, doi: <http://dx.doi.org/10.1039/C2EE23284G>.
- [18] G. Bender, T.A. Zawodzinski, A.P. Saab, Fabrication of high precision PEFC membrane electrode assemblies, *J. Power Sources* 124 (2003) 114–117, doi: [http://dx.doi.org/10.1016/S0378-7753\(03\)00735-3](http://dx.doi.org/10.1016/S0378-7753(03)00735-3).
- [19] N. Arjona, M.-A. Goulet, M. Guerra-Balcázar, J. Ledesma-García, E. Kjeang, L.G. Arriaga, Direct Formic Acid Microfluidic Fuel Cell with Pd Nanocubes Supported on Flow-Through Microporous Electrodes, *ECS Electrochem. Lett.* 4 (2015) F24–F28, doi: <http://dx.doi.org/10.1149/2.0031504eel>.
- [20] V. Meille, Review on methods to deposit catalysts on structured surfaces, *Appl. Catal. A Gen.* 315 (2006) 1–17, doi: <http://dx.doi.org/10.1016/j.apcata.2006.08.031>.
- [21] A.D. Taylor, E.Y. Kim, V.P. Humes, J. Kizuka, L.T. Thompson, Inkjet printing of carbon supported platinum 3-D catalyst layers for use in fuel cells, *J. Power Sources* 171 (2007) 101–106, doi: <http://dx.doi.org/10.1016/j.jpowsour.2007.01.024>.
- [22] M.F.L. De Volder, S.H. Tawfik, R.H. Baughman, A.J. Hart, Carbon nanotubes: present and future commercial applications—SOM, *Science* 339 (2013) 535–539, doi: <http://dx.doi.org/10.1126/science.1222453>.
- [23] P. Han, Y. Yue, Z. Liu, W. Xu, L. Zhang, H. Xu, et al., Graphene oxide nanosheets/multi-walled carbon nanotubes hybrid as an excellent electrocatalytic material towards VO^{2+}/VO_2^+ redox couples for vanadium redox flow batteries, *Energy Environ. Sci.* 4 (2011) 4710, doi: <http://dx.doi.org/10.1039/c1ee01776d>.
- [24] H.Q. Zhu, Y.M. Zhang, L. Yue, W.S. Li, G.L. Li, D. Shu, et al., Graphite-carbon nanotube composite electrodes for all vanadium redox flow battery, *J. Power Sources* 184 (2008) 637–640, doi: <http://dx.doi.org/10.1016/j.jpowsour.2008.04.016>.
- [25] G. Wei, C. Jia, J. Liu, C. Yan, Carbon felt supported carbon nanotubes catalysts composite electrode for vanadium redox flow battery application, *J. Power Sources* 220 (2012) 185–192, doi: <http://dx.doi.org/10.1016/j.jpowsour.2012.07.081>.
- [26] G. Wei, X. Fan, J. Liu, C. Yan, Electrospun carbon nanofibers/electrocatalyst hybrids as asymmetric electrodes for vanadium redox flow battery, *J. Power Sources* 281 (2015) 1–6, doi: <http://dx.doi.org/10.1016/j.jpowsour.2015.01.161>.
- [27] S. Wang, X. Zhao, T. Cochell, A. Manthiram, Nitrogen-doped carbon nanotube/graphite felt as advanced electrode materials for vanadium redox flow batteries, *J. Phys. Chem. Lett.* 3 (2012) 2164–2167.
- [28] W. Li, J. Liu, C. Yan, The electrochemical catalytic activity of single-walled carbon nanotubes towards VO^{2+}/VO_2^+ and V^{3+}/V^{2+} redox pairs for an all vanadium redox flow battery, *Electrochim. Acta* 79 (2012) 102–108, doi: <http://dx.doi.org/10.1016/j.electacta.2012.06.109>.
- [29] W. Li, J. Liu, C. Yan, Multi-walled carbon nanotubes used as an electrode reaction catalyst for VO^{2+} for a vanadium redox flow battery, *Carbon* N. Y. 49 (2011) 3463–3470, doi: <http://dx.doi.org/10.1016/j.carbon.2011.04.045>.
- [30] Z. González, P. Álvarez, C. Blanco, S. Vega-Díaz, F. Tristán-López, L.P. Rajukumar, et al., The influence of carbon nanotubes characteristics in their performance as positive electrodes in vanadium redox flow batteries, *Sustain. Energy Technol. Assessments* 9 (2015) 105–110, doi: <http://dx.doi.org/10.1016/j.seta.2014.12.008>.
- [31] M.P. Manahan, Q.H. Liu, M.L. Gross, M.M. Mench, Carbon nanoporous layer for reaction location management and performance enhancement in all-vanadium redox flow batteries, *J. Power Sources* 222 (2013) 498–502, doi: <http://dx.doi.org/10.1016/j.jpowsour.2012.08.097>.
- [32] M.-A. Goulet, E. Kjeang, Process of increasing energy conversion and electrochemical efficiency of a scaffold using a deposition material, (2015) US Patent Application 14/842, 812.
- [33] E.O. Barnes, X. Chen, P. Li, R.G. Compton, Voltammetry at porous electrodes: A theoretical study, *J. Electroanal. Chem.* 720–721 (2014) 92–100, doi: <http://dx.doi.org/10.1016/j.jelechem.2014.03.028>.
- [34] D. Menshykau, R.G. Compton, The influence of electrode porosity on diffusional cyclic voltammetry, *Electroanalysis* 20 (2008) 2387–2394, doi: <http://dx.doi.org/10.1002/elan.200804334>.
- [35] D. Menshykau, I. Streeter, R.G. Compton, Influence of electrode roughness on cyclic voltammetry, *J. Phys. Chem. C* 112 (2008) 14428–14438, doi: <http://dx.doi.org/10.1021/jp8047423>.
- [36] I. Streeter, G.G. Wildgoose, L. Shao, R.G. Compton, Cyclic voltammetry on electrode surfaces covered with porous layers: An analysis of electron transfer kinetics at single-walled carbon nanotube modified electrodes, *Sensors Actuators B Chem.* 133 (2008) 462–466, doi: <http://dx.doi.org/10.1016/j.snb.2008.03.015>.
- [37] K.R. Ward, R.G. Compton, Quantifying the apparent catalytic effect of porous electrode surfaces, *J. Electroanal. Chem.* 724 (2014) 43–47, doi: <http://dx.doi.org/10.1016/j.jelechem.2014.04.009>.
- [38] J. Friedl, C.M. Bauer, A. Rinaldi, U. Stimming, Electron transfer kinetics of the VO^{2+}/VO_2^+ Reaction on multi-walled carbon nanotubes, *Carbon* N. Y. 63 (2013) 228–239, doi: <http://dx.doi.org/10.1016/j.carbon.2013.06.076>.
- [39] C. Punckt, M.A. Pope, I.A. Aksay, On the Electrochemical Response of Porous Functionalized Graphene Electrodes, *J. Phys. Chem. C* 117 (2013) 16076–16086, doi: <http://dx.doi.org/10.1021/jp405142k>.
- [40] M.-A. Goulet, M. Eikerling, E. Kjeang, Direct measurement of electrochemical reaction kinetics in flow-through porous electrodes, *Electrochem. Commun.* 57 (2015) 14–17, doi: <http://dx.doi.org/10.1016/j.elecom.2015.04.019>.
- [41] M.-A. Goulet, M. Skyllas-Kazacos, E. Kjeang, The importance of wetting in carbon paper electrodes for vanadium redox reactions, *Carbon* N. Y. 101 (2016) 390–398, doi: <http://dx.doi.org/10.1016/j.carbon.2016.02.011>.
- [42] M.-A. Goulet, E. Kjeang, Reactant recirculation in electrochemical co-laminar flow cells, *Electrochim. Acta* 140 (2014) 217–224.

- [43] M.-A. Goulet, E. Kjeang, Co-laminar flow cells for electrochemical energy conversion, *J. Power Sources* 260 (2014) 186–196.
- [44] E. Kjeang, *Microfluidic Fuel Cells and Batteries*, Springer, 2014.
- [45] K. Haubert, T. Drier, D. Beebe, PDMS bonding by means of a portable, low-cost corona system, *Lab Chip* 6 (2006) 1548, doi:<http://dx.doi.org/10.1039/b610567j>.
- [46] L. Jiang, L. Gao, J. Sun, Production of aqueous colloidal dispersions of carbon nanotubes, *J. Colloid Interface Sci.* 260 (2003) 89–94, doi:[http://dx.doi.org/10.1016/S0021-9797\(02\)00176-5](http://dx.doi.org/10.1016/S0021-9797(02)00176-5).
- [47] D. Krishnamurthy, E.O. Johansson, J.W. Lee, E. Kjeang, Computational modeling of microfluidic fuel cells with flow-through porous electrodes, *J. Power Sources* 196 (2011) 10019–10031, doi:<http://dx.doi.org/10.1016/j.jpowsour.2011.08.024>.
- [48] E. Kjeang, R. Michel, D.A. Harrington, N. Djilali, D. Sinton, A microfluidic fuel cell with flow-through porous electrodes, *J. Am. Chem. Soc.* 130 (2008) 4000–4006, doi:<http://dx.doi.org/10.1021/ja078248c>.
- [49] Y. Oren, Capacitive deionization (CDI) for desalination and water treatment—past, present and future (a review), *Desalination* 228 (2008) 10–29, doi:<http://dx.doi.org/10.1016/j.desal.2007.08.005>.

Appendix F.

Approaching the power density limits of aqueous electrochemical flow cells

Maximizing the power density of aqueous electrochemical flow cells

Marc-Antoni Goulet^a, Omar A. Ibrahim^a, Will H.J. Kim^a, Erik Kjeang^{a*}

^aSchool of Mechatronic Systems Engineering, Simon Fraser University, 250-13450 102
Avenue, Surrey, BC, V3T 0A3, Canada

*Corresponding Author: Tel: +1 778 782 8791, Fax: +1 778 782 7514,

E-mail: ekjeang@sfu.ca

Abstract

To transition toward sustainable energy systems, next generation power sources must provide high power density at minimum cost. Using inexpensive and environmentally friendly fabrication methods, this work describes a room temperature electrochemical flow cell with a maximum power density of $2.01 \text{ W}\cdot\text{cm}^{-2}$ or $13.4 \text{ W}\cdot\text{cm}^{-3}$. In part, this is achieved by minimizing ohmic resistance through decreased electrode spacing, implementation of current collectors and improvement of electrolyte conductivity. The majority of the performance gain is provided by a novel *in operando* dynamic flowing deposition method for which the cell design has been optimized. Carbon nanotubes (CNTs) are deposited dynamically at the entrance of and within the carbon paper electrodes during operation of the cell. A natural equilibrium is reached between deposition and detachment of CNTs at which the electrochemical surface area and pore size distribution of the flow-through porous electrodes are greatly enhanced. In this way, the novel deposition method more than doubles the power density of the cell and sets a new performance benchmark for what is practically attainable with aqueous electrochemical flow cells. Overall, it is expected that the design and operation methods illustrated here will enable a wide range of electrochemical flow cell technologies to achieve optimal performance.

Keywords: *flow cell; fuel cell; flow battery; mass transport; kinetics; power density*

1. Introduction

Whether for utility or consumer scale applications, there is a growing demand for electrochemical energy solutions due to their application flexibility [1,2]. Among the options available for open electrochemical cells based on bulk flow of reactants, a new subcategory has recently emerged which relies on co-laminar flow rather than membranes to achieve reactant separation [3,4]. These co-laminar flow cells (CLFCs) have been developed as both fuel cells and rechargeable flow batteries [5,6] with a wide range of reactant chemistries [7–10]. Although constrained in size by the hydrodynamic conditions necessary for laminar flow, these typically microscale devices benefit from the lower materials cost and higher durability expected from membraneless design [11]. It was suggested in a recent review by our group that to assess the viability of CLFC technology, efforts would need to be made to determine the ideal cell dimensions to produce the maximum power density as a starting point for scale-up of the technology and practical application pairing [12].

Thus far, one of the most ambitious applications identified for CLFCs is on-chip power and cooling of processors for which higher power density has been emphasized as the metric of choice [13]. Others have proposed the combination of inexpensive CLFC technology with readily available biofuels such as glucose for powering biomedical devices [14–17]. Regardless of the application, aiming for high power density typically increases other performance metrics such as energy efficiency or fuel utilization and can also reduce material cost and device footprint. Using a combined experimental and modelling approach, the advances demonstrated in this work set a new standard in the power density of co-laminar flow cells, without the use of catalysts or elevated

temperatures and pressures; thereby providing a low-cost benchmark for further research into system scale-up and device integration. To the authors' knowledge the achieved power density also exceeds that of conventional aqueous fuel cells and flow batteries based on membrane electrode assembly (MEA) architectures. This is accomplished by simultaneously addressing all three sources of voltage loss in electrochemical cells, namely those due to kinetic, ohmic and mass transport constraints. The inspiration for this endeavour stems from the promising preliminary results observed with the *in situ* flowing deposition method recently invented by our group whereby a temporary suspension of carbon nanotubes (CNTs) is injected through an assembled flow cell before operation in order to increase the surface area of the pre-existing carbon paper electrode by over an order of magnitude [18]. In the present work, it is further shown that this flowing deposition can be achieved dynamically during operation of a flow cell, leading to even higher surface area and better mass transport characteristics [19]. To realize the full benefit of the deposition method however, extensive characterization and optimization of cell design was necessary to reduce the overall ohmic resistance of the cell toward the fundamental limit imposed by liquid electrolytes. When enhanced with *in operando* dynamic flowing deposition of CNTs, the next generation cell design is shown to achieve record breaking power density.

2. Experimental

2.1 Materials

The V^{2+}/V^{3+} and VO^{2+}/VO_2^+ reactants used in this study are prepared by charging a commercial grade 1.7 M vanadium redox species in 4 M sulfuric acid solution with a

conventional flow battery to a 90-95% state of charge (SOC). The reactant concentration is then lowered to roughly 1.0 M by subsequent addition of 4 M sulfuric acid. These reactants are pumped into and out of the CLFCs with two syringe pumps (Harvard Apparatus MA1 70-2209) operated in unison at flow rates ranging from 10 to 200 $\mu\text{L}\cdot\text{min}^{-1}$. Multi-walled carbon nanotubes (CNTs) for electrode enhancement are 10-50 μm in length and <10 nm in outer diameter. Flowing deposition of a temporary dilute suspension of CNTs in deionized water is accomplished with the same injection and rinsing method previously reported [18], whereas CNTs are dispersed directly into the reactants for dynamic *in operando* flowing deposition.

2.2 Cell fabrication

All CLFCs are fabricated by soft lithography of 150 μm high microfluidic channels in poly(dimethylsiloxane) (PDMS) as described elsewhere. A glass slide is used to cap the channels and compress 180 μm thick heat treated Toray TGP-060 carbon paper electrodes positioned within grooves as shown in Fig. 1. The baseline cell is based on the same design used in previous studies [20], with an active electrode length of 10 mm, width of 1.0 mm and channel width of 1.0 mm; whereas the next generation cell design uses the same length with an average channel width of 0.5 mm and electrode width of only 0.5 mm. In addition the next generation cell uses current collectors taped to the glass slide which extend outside the cell for electrical contact.

2.3 Characterization

Polarization curves are based on the average steady state current for each potentiostatic measurement with a Gamry Reference 3000 potentiostat. Electrochemical impedance spectroscopy (EIS) measurements are conducted at 10 mV perturbation from the open circuit potential (OCP) to verify the impedance of the cell.

For the purpose of power density calculations, conventional sandwich structure cell design is typically normalized by the geometric electrode area parallel to the membrane or co-laminar interface [4–6], whereas for ‘monolithic’ or single layer on-chip cells the ‘projected’ area of a single electrode has often been used [3,21]. To avoid ambiguity in performance improvement however, volumetric density has been suggested to encompass both perspectives and provide a meaningful metric for comparison [12]. For example, the baseline cell with a 150 μm channel height would therefore have a ‘projected’ electrode area of 0.1 cm^2 , a ‘cross-sectional’ electrode area of 0.015 cm^2 and an electrochemical chamber volume of 0.0045 cm^3 , whereas the smaller footprint next generation cell has the same cross-sectional area but a chamber volume of only 0.00225 cm^3 .

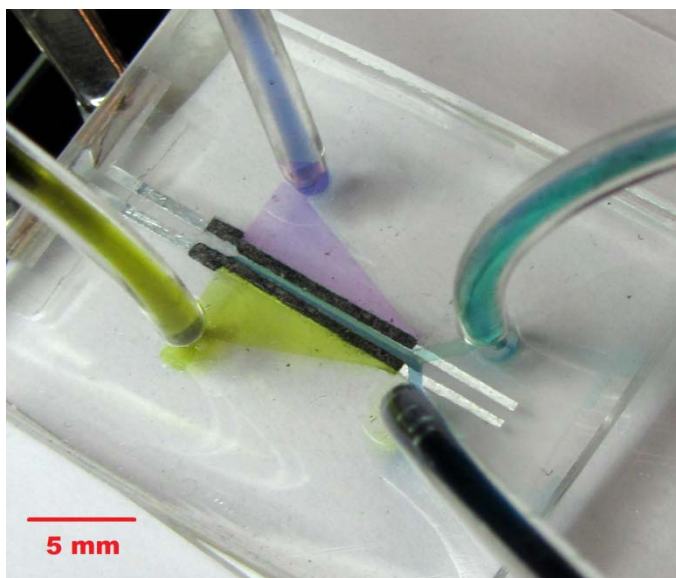


Fig. 1. Real-time image of next generation co-laminar flow cell discharging vanadium redox reactants. The colour changes observed are indicative of the different vanadium ion oxidation states.

3. Results and discussion

3.1 Cell optimization

The baseline electrochemical flow cell for this work is a modified form of the original cell design with carbon paper flow-through porous electrodes first conceived by Kjeang et al. [21]. The proposed design advances are informed by complete characterization of each source of voltage loss in this cell. The kinetic reaction rates and polarization behaviour for each vanadium redox couple on carbon paper electrodes were established using an analytical flow cell technique, as previously reported [22]. An investigation into the ionic conductivity of the electrolytes, discussed in section S1 of the electronic supplementary information (ESI) and displayed in Fig. S1-1 and Table S1-1,

reveals that ionic resistance of the centre channel accounts for roughly two thirds ($20\ \Omega$) of the overall resistance of the baseline cell, with the remainder being comprised of contact and electrical resistance within the electrode. With these values known, an experimental and computational parametric study is conducted to investigate the effect of cell dimensions on power density. The results of this study, shown in Fig. S2-1 and S2-2 and compiled in Table S2-1 and S2-2 of the ESI, indicate that volumetric power density can best be enhanced by decreasing the width of the centre channel. Although larger electrode width also has a positive effect on power output through both decreased electrical resistance and increased electrochemical surface area (ESA), these effects can be better improved through the use of current collectors [23] and surface area enhancement, respectively [18]. In addition to architectural modifications, the investigation into ionic conductivity also reveals that changes in electrolyte formulation can further decrease the ohmic resistance of the centre channel.

The next generation cell architecture displayed in Fig. 1 incorporates the above mentioned strategies to achieve a minimum ohmic resistance. Reducing the channel width of the baseline cell by half decreases the ohmic resistance by approximately $10\ \Omega$ and increases the volumetric power density by nearly 50%. Further reduction in channel width becomes fundamentally challenging for on-chip prototype fabrication and also compromises the open circuit potential of the cell due to diffusive crossover [20]. As explained in the ESI, another $2\text{--}3\ \Omega$ of channel resistance can be eliminated by reducing the overall vanadium ion concentration to increase the ionic conductivity of the $\text{V}^{2+}/\text{V}^{3+}$ electrolyte. Lastly, by incorporating current collectors such as those used by Lee et al. [23], the electrical resistance of the electrodes and contacts can be nearly eliminated.

With current collectors providing the necessary electrical conductivity, the width of the carbon paper electrodes in the next generation design can also be reduced, leading to a smaller device footprint without any impact on the cell resistance. Combining these three approaches the overall ohmic resistance of the baseline cell can be reduced from 30 Ω to approximately 8 Ω as shown by the high frequency intercept in Fig. 2. When converted into an area specific resistance (ASR) using the 0.015 cm^2 area of the co-laminar interface, this results in an ASR of 0.12 $\Omega \cdot \text{cm}^2$ for the entire cell, which is to the authors knowledge better than any published value for an aqueous flow cell [24] due to the high ionic conductivity of the liquid H_2SO_4 electrolyte as compared to the solid electrolytes otherwise used for electrode separation [25].

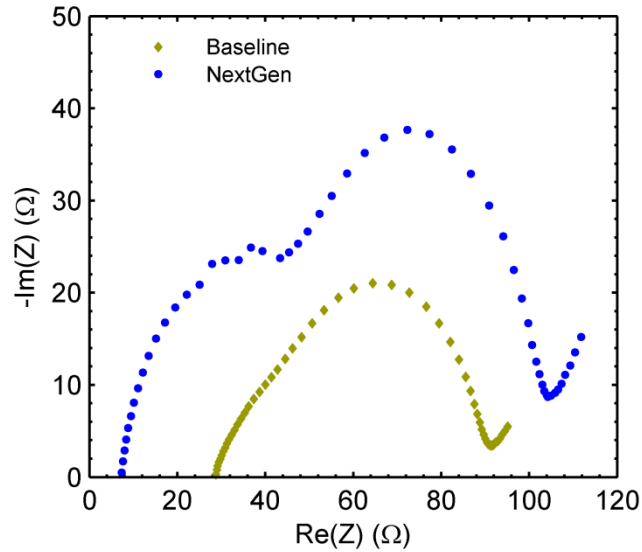


Fig. 2. Nyquist plot of baseline cell impedance operated with 90% SOC, 1.7 M vanadium reactants, and next generation cell operated with 95% SOC, 1.0 M vanadium reactants.

3.2 Dynamic flowing deposition

Although a decreased electrode width and lower vanadium ion concentration both engender an overall reduction in reaction kinetics, these adverse effects can be compensated for by ESA enhancement of the electrode material. Using the flowing deposition method recently invented by our group, carbon nanotubes (CNTs) are deposited at the upstream entrance and within the porous carbon paper. As explained in the previous study [18] and depicted in Fig. 3, the CNTs form a nanoporous layer with a much greater surface area per volume than the carbon paper scaffold. The deposition is performed prior to cell operation by injecting a temporary aqueous suspension of CNTs through both electrodes of the assembled cell, followed by rinsing of the electrodes at high flow rate. The deposition process reaches a saturation point at which additional CNT deposition does not have any further effect due to loosely adhered material being swept away during flow cell operation. This method is modified in the current study to further enhance the surface area and mass transport properties of the electrodes by performing flowing deposition *dynamically* during operation with CNTs suspended directly in the redox electrolytes. When deposited in this way, the *in operando* flowing deposition method ensures lodging of deposition material within and obstruction of the main flow pathways of the porous electrodes which can have synergistic effects between increased ESA and reduced pore size by enhancing local mass transport where it is most needed [19].

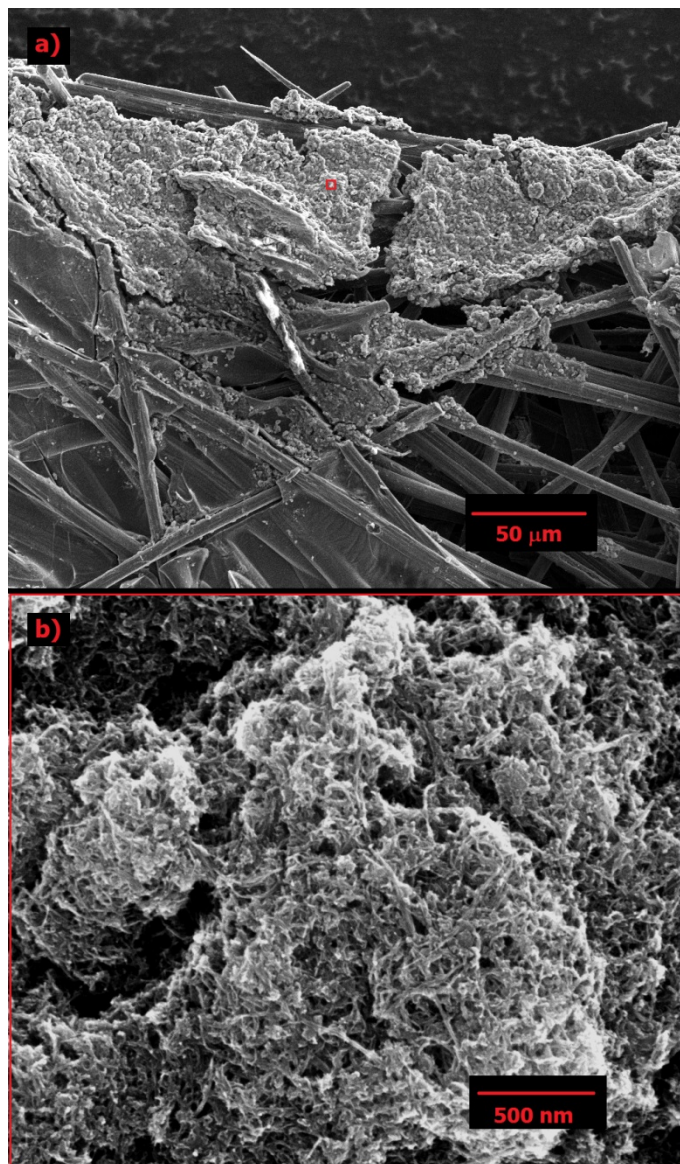


Fig. 3. SEM images of CNT flowing deposition on carbon paper.

While the dynamically deposited electrode material will tend to form the same nanoporous structures as those observed in Fig. 3, at certain flow velocity and concentration combinations the deposition rate will exceed the rate at which CNTs are shed from the carbon paper. In this case, the build-up of CNTs will obstruct and further reduce the size of the larger pores seen in Fig. 3-a), leading to an increasing pressure drop

across the electrode until the pressure is sufficient to remove the obstruction, at which point the process repeats. In this way, a natural dynamic equilibrium between the average pore size and flow velocity is obtained, akin to the natural formation of logjams in rivers [26]. This dynamic process of deposition, jamming and obstruction removal was observed by differential pressure transducer across an electrode. For the $200 \mu\text{L}\cdot\text{min}^{-1}$ case, regular pressure pulsations would occur from 5.8 – 7.2 kPa roughly every 5 s for the entire duration of flow. When multiplied by the flow rate through the electrode this leads to a maximum total pumping power consumption of 0.05 mW. Although this value is considerably higher than for the previous deposition method [18], it is negligible ($< 0.1\%$) when compared to the power output of the cell and indicates a general decrease in electrode pore size distribution. In addition, the pressure pulsations due to the ‘logjam’ effect can also be observed in the potentiostatic measurements as a regular pulsation in the output current, as shown in Fig. 4. The peaks in current, which are roughly 10% above the norm for each potential, likely coincide with the maximum level of deposition corresponding to maximum ESA and minimum pore size.

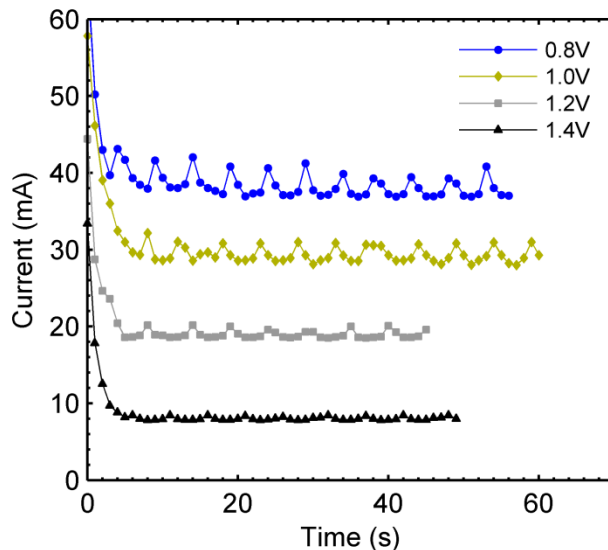


Fig. 4. Potentiostatic measurements showing regular oscillation in current for dynamic *in operando* flowing deposition at $200\ \mu\text{L}\cdot\text{min}^{-1}$.

3.3 Cell Performance

Regardless of the pulsation, the average current produced at each potential is significantly higher than that produced by the previous flowing deposition method. Moreover, the equilibrium established by the *in operando* method maintains this deposition over time, as opposed to the previous pretreatment method which tends to wash out over time. The polarization curves in Fig. 5 demonstrate the effect of both deposition methods on the overall next generation cell performance at both low and high flow rates. It should be noted that in all cases the ohmic resistance of the cell is verified by EIS to correspond to the optimized $8\ \Omega$ of the next generation design. As such, the differences in polarization behaviour in Fig. 5 are strictly attributable to mass transport and kinetic differences. As previously demonstrated, the deposition of CNTs leads to a substantial increase in ESA of the electrodes with an associated improvement in the low current kinetic region of the polarization curve. According to the kinetic model described in the ESI, the very strong enhancements in the measured reaction kinetics of this cell (Fig. 5) suggest that the *in operando* treatment increased the ESA by two orders of magnitude. In addition the deposition also favors mass transport by depositing the material directly in the flow path of the reactants and reducing the average pore size of the electrode and thereby increasing the convective flow velocity through these pores. This is substantiated by the increase in limiting current of the cell at low flow rates (Fig. 5a), where the dynamically deposited CNTs extend the current limit from 11.6 to 14.1

mA, equivalent to over 90% reactant conversion at $10 \mu\text{L}\cdot\text{min}^{-1}$. Moreover, at a high voltage efficiency operating point of 1.4 V, the cell with dynamically deposited CNTs converts over three times more reactants than the bare next generation cell.

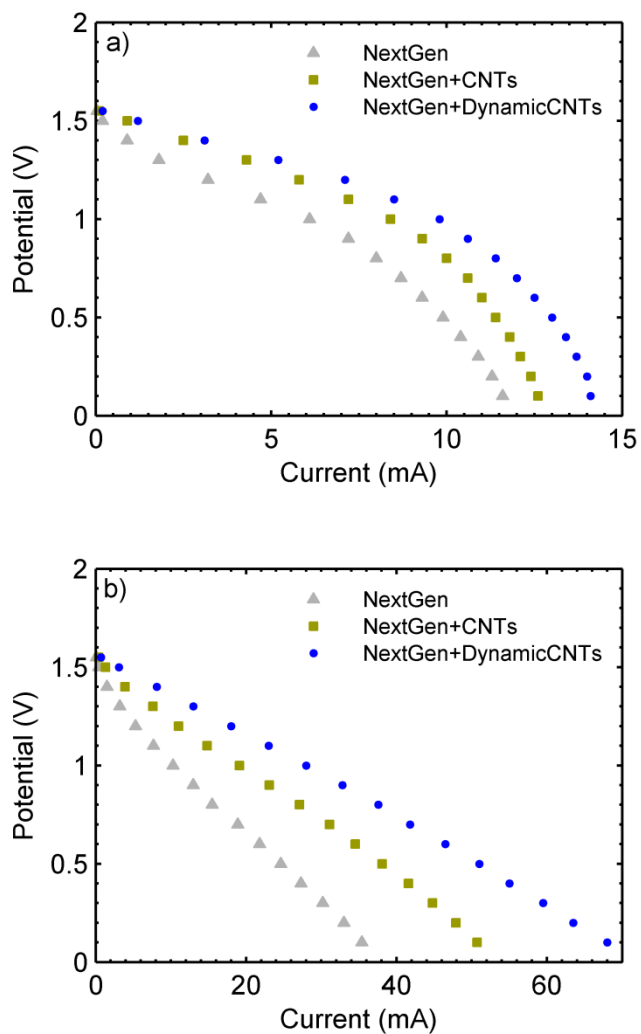


Fig. 5. Polarization curves for the next generation flow cell with and without flowing deposition of CNTs at a) $10 \mu\text{L}\cdot\text{min}^{-1}$ and b) $200 \mu\text{L}\cdot\text{min}^{-1}$.

With an identical ohmic resistance, the change in slope of the high flow rate polarization curves in Fig. 5b also indicates an improvement in both reaction kinetics and mass transport due to flowing deposition of CNTs. The favorable increase in polarization slope directly translates into a similar increase in voltage and energy efficiency for the discharge process. As an example relevant to low current density high efficiency operation, at a voltage efficiency of 90%, the bare next generation cell produces only 100 mAcm^{-2} whereas the cell used in conjunction with *in operando* deposition produces roughly 500 mAcm^{-2} , which is considerably higher than other cells published in the literature. To produce the same current, the bare next generation cell only operates at 70% voltage efficiency. This remarkable efficiency gain is a direct result of high surface area treatments and particularly important for secondary battery operation.

The effects of these improvements on the maximum power density of the cell are summarized in Table 1. The improvement in ohmic resistance of the next generation design over the baseline cell leads to a 59% increase in total power at higher flow rates of 200 $\mu\text{L}\cdot\text{min}^{-1}$. In addition, the smaller on-chip projected area of the electrodes and channel is reduced by half, leading to an even greater power density increase, approaching 6 Wcm^{-3} , as predicted by the model in Fig. S3-1 and experimentally verified in Table 1. As detailed above, this optimized next generation design synergistically amplifies the relative enhancement produced by either deposition method. Flowing deposition of CNTs through the kinetically limited anode of the baseline cell had previously yielded a 23% increase in maximum power output of the cell [18]. As seen in Table 1, the same flowing deposition process on both electrodes now increases the power output of the next generation cell from 13 to 22 mW, a 65% increase which also

compensates for the reduced reactant concentration and electrode size of the next generation design. Dynamic CNT deposition further increases this output to 30 mW, a total improvement of 127%. With the combined enhancements of the next generation design, this results in a 263% increase in power output over the baseline cell. When the redesigned dimensions of the electrochemical cell are also taken into account, the dynamically enhanced cell has nearly 7x the volumetric power density of the baseline cell. From the perspective of cross-sectional power density, at 2.01 Wcm^{-2} , the proposed device surpasses the current leading CLFC recently published by Lu et al. at 1.3 Wcm^{-2} by a considerable margin [27]. Similarly, the dynamically enhanced next generation cell also significantly outperforms all known aqueous membrane based electrochemical flow cells [28–31] without the use of catalysts or elevated temperatures. Although this particular cell is limited in scale and application, the performance observed in this work suggests that using highly conductive liquid electrolytes rather than ionomer membranes, as in the early alkaline fuel cells developed by NASA [32,33], is a concept worth revisiting, particularly for single pass discharge of reactants [34]. In addition, the exceptional results achieved with the dynamic flowing deposition method further demonstrate the synergy possible when optimized device architecture is combined with ideal electrode materials.

Table 1 Maximum cell performance at 200 $\mu\text{L}\cdot\text{min}^{-1}$.

Cell	Power (mW)	Cross sectional power density (Wcm^{-2})	Volumetric power density (Wcm^{-3})
Baseline	8.31	0.573	1.91
NextGen	13.2	0.882	5.88
NextGen+CNTs	21.8	1.45	9.68
NextGen+Dynamic CNTs	30.1	2.01	13.4

3.4 Discussion

Although other examples of dynamic electrode formation for achieving high electrochemical surface area have recently emerged, these have primarily been focused on capacitive energy storage in slurry electrodes [35–39]. Based on percolating networks of conductive particles dissolved in electrolytes, these slurry electrodes tend to suffer from high viscosity and high electrical resistance. Even with additional faradaic reactions taking place between slurry electrodes only modest performance has been demonstrated [40]. In the present case, the minute quantities of CNTs suspended in the electrolyte do not measurably affect its viscosity, making pumping losses related only to the pore size and flow velocity. Moreover, the quantities under consideration negligibly affect the overall cost of the electrolytes. Lastly, the presence of a reasonably conductive porous scaffold electrode ensures a constant resistance which is considerably lower than for slurry electrodes. The CNTs which adhere physically and aggregate on this scaffold become part of this permanent electrical pathway. For these reasons, the dynamic flowing deposition method presented here enables highly conductive electrodes with very

high surface area and beneficial pore sizes. Although several other studies have attempted deposition of carbon nanomaterials onto paper or felt, these have used additional *ex situ* fabrication steps involving solvents or expensive processes such as chemical vapor deposition, and have not explicitly targeted the reactant flow pathways [41–43].

For electrochemical cells based on co-laminar flow of reactants, the example described in this study serves as an ideal low cost starting point for scale up and stacking of cells, thereby moving the technology one step closer to implementation. The on-chip fabrication style and high volumetric power density make this compact device design particularly suitable for combined power and cooling of microprocessors [13]. More generally, with no additional chemicals or processes, the dynamic *in operando* flowing deposition method provides a simple, inexpensive and ‘green’ strategy for effectively enhancing the surface area and mass transport properties of flow-through porous electrodes. As such, this method is especially relevant to and likely to have considerable impact on flow battery research [19].

4. Conclusions

This work demonstrates that exceptionally high power densities can be achieved with room-temperature electrochemical flow cells by simultaneously addressing kinetic, ohmic and mass transport losses. An electrochemical cell based on co-laminar flow of vanadium redox reactants was first optimized to produce nearly $0.9 \text{ W} \cdot \text{cm}^{-2}$. The reduced footprint design relied upon current collectors and moderately concentrated reactants in liquid electrolyte to achieve a minimum ohmic resistance. The adverse effects of smaller

electrode dimensions and lower reactant concentration were compensated for by a novel deposition method [19]. Dynamic *in operando* flowing deposition of carbon nanotubes was shown to enhance both the electrochemical surface area and mass transport properties of the porous carbon paper electrodes in flow-through configuration. This inexpensive enhancement raised the maximum power density of the cell to $2.01 \text{ W}\cdot\text{cm}^{-2}$ or $13.4 \text{ W}\cdot\text{cm}^{-3}$, setting a new state-of-the-art performance benchmark for aqueous electrochemical flow cells. The obtained performance level is believed to be close to the practically attainable limit of voltage loss reductions with aqueous liquid reactants at room temperature. The methods and design strategies reported here could be readily adapted to a wide range of electrochemical flow cells in order to achieve similar gains in power density and conversion efficiency.

Acknowledgments

Funding for this research provided by the Natural Sciences and Engineering Research Council of Canada, Western Economic Diversification Canada, Canada Foundation for Innovation, and British Columbia Knowledge Development Fund is highly appreciated.

References

- [1] D. Larcher, J.-M. Tarascon, Towards greener and more sustainable batteries for electrical energy storage., *Nat. Chem.* 7 (2015) 19–29.
- [2] G.L. Soloveichik, Flow Batteries: Current Status and Trends, *Chem. Rev.* 115 (2015) 11533–11558.
- [3] R. Ferrigno, A.D. Stroock, T.D. Clark, M. Mayer, G.M. Whitesides, Membraneless Vanadium Redox Fuel Cell Using Laminar Flow, *J. Am. Chem. Soc.* 124 (2002) 12930–12931.

- [4] E.R. Choban, L.J. Markoski, A. Wieckowski, P.J.A. Kenis, Microfluidic fuel cell based on laminar flow, *J. Power Sources*. 128 (2004) 54–60.
- [5] W.A. Braff, M.Z. Bazant, C.R. Buie, Membrane-less hydrogen bromine flow battery., *Nat. Commun.* 4 (2013) 2346.
- [6] J.W. Lee, M.-A. Goulet, E. Kjeang, Microfluidic Redox Battery, *Lab Chip*. 13 (2013) 2504–2507.
- [7] J.L. Cohen, D.J. Volpe, D.A. Westly, A. Pechenik, H.D. Abruña, A dual electrolyte H₂/O₂ planar membraneless microchannel fuel cell system with open circuit potentials in excess of 1.4 V., *Langmuir*. 21 (2005) 3544–3550.
- [8] R.S. Jayashree, L. Gancs, E.R. Choban, A. Primak, D. Natarajan, L.J. Markoski, et al., Air-breathing laminar flow-based microfluidic fuel cell., *J. Am. Chem. Soc.* 127 (2005) 16758–16759.
- [9] S. Hasegawa, K. Shimotani, K. Kishi, H. Watanabe, Electricity Generation from Decomposition of Hydrogen Peroxide, *Electrochem. Solid-State Lett.* 8 (2005) A119–A121.
- [10] F.R. Brushett, R.S. Jayashree, W.-P. Zhou, P.J.A. Kenis, Investigation of fuel and media flexible laminar flow-based fuel cells, *Electrochim. Acta*. 54 (2009) 7099–7105.
- [11] E. Kjeang, *Microfluidic Fuel Cells and Batteries*, Springer, 2014.
- [12] M.-A. Goulet, E. Kjeang, Co-laminar flow cells for electrochemical energy conversion, *J. Power Sources*. 260 (2014) 186–196.
- [13] P. Ruch, T. Brunschweiler, W. Escher, S. Paredes, B. Michel, Toward five-dimensional scaling: How density improves efficiency in future computers, *IBM J. Res. Dev.* 55 (2011) 15:1–15:13.
- [14] A. Zebda, L. Renaud, M. Cretin, C. Innocent, F. Pichot, R. Ferrigno, et al., Electrochemical performance of a glucose/oxygen microfluidic biofuel cell, *J. Power Sources*. 193 (2009) 602–606.
- [15] M.J. González-Guerrero, J.P. Esquivel, D. Sánchez-Molas, P. Godignon, F.X. Muñoz, F.J. Del Campo, et al., Membraneless glucose/O₂ microfluidic enzymatic biofuel cell using pyrolyzed photoresist film electrodes., *Lab Chip*. (2013) 2972–2979.
- [16] A. Dector, R.A. Escalona-Villalpando, D. Dector, V. Vallejo-Becerra, A.U. Chávez-Ramírez, L.G. Arriaga, et al., Perspective use of direct human blood as an energy source in air-breathing hybrid microfluidic fuel cells, *J. Power Sources*. 288 (2015) 70–75.
- [17] J.P. Esquivel, F.J. Del Campo, J.L. Gómez de la Fuente, S. Rojas, N. Sabaté, Microfluidic fuel cells on paper: meeting the power needs of next generation lateral flow devices, *Energy Environ. Sci.* 7 (2014) 1744.
- [18] M.-A. Goulet, A. Habisch, E. Kjeang, In Situ Enhancement of Flow-through Porous Electrodes with Carbon Nanotubes via Flowing Deposition, *Electrochim. Acta*. 206 (2016) 36–44.

- [19] M.-A. Goulet, E. Kjeang, Process of increasing energy conversion and electrochemical efficiency of a scaffold using a deposition material, (2015) US Patent Application 14/842,812.
- [20] M.-A. Goulet, E. Kjeang, Reactant recirculation in electrochemical co-laminar flow cells, *Electrochim. Acta.* 140 (2014) 217–224.
- [21] E. Kjeang, R. Michel, D.A. Harrington, N. Djilali, D. Sinton, A microfluidic fuel cell with flow-through porous electrodes., *J. Am. Chem. Soc.* 130 (2008) 4000–4006.
- [22] M.-A. Goulet, M. Eikerling, E. Kjeang, Direct measurement of electrochemical reaction kinetics in flow-through porous electrodes, *Electrochem. Commun.* 57 (2015) 14–17.
- [23] J.W. Lee, E. Kjeang, Chip-embedded thin film current collector for microfluidic fuel cells, *Int. J. Hydrogen Energy.* 37 (2012) 9359–9367.
- [24] R.M. Darling, K.G. Gallagher, J.A. Kowalski, S. Ha, F.R. Brushett, Pathways to low-cost electrochemical energy storage: a comparison of aqueous and nonaqueous flow batteries, *Energy Environ. Sci.* 7 (2014) 3459–3477.
- [25] D.R. Lide, *CRC Handbook of Chemistry and Physics*, 90th ed., CRC Press, Boca Raton: FL, 2010.
- [26] E.J. Hickin, Vegetation and river channel dynamics, *Can. Geogr.* 28 (1984) 111–126.
- [27] X. Lu, J. Xuan, D.Y.C. Leung, H. Zou, J. Li, H. Wang, et al., A switchable pH-differential unitized regenerative fuel cell with high performance, *J. Power Sources.* 314 (2016) 76–84.
- [28] S. Zhao, H. Yin, L. Du, G. Yin, Z. Tang, S. Liu, Three dimensional N-doped graphene/PtRu nanoparticle hybrids as high performance anode for direct methanol fuel cells, *J. Mater. Chem. A.* 2 (2014) 3719.
- [29] Y. Zhu, S.Y. Ha, R.I. Masel, High power density direct formic acid fuel cells, *J. Power Sources.* 130 (2004) 8–14.
- [30] K.T. Cho, P. Ridgway, A.Z. Weber, S. Haussener, V. Battaglia, V. Srinivasan, High Performance Hydrogen/Bromine Redox Flow Battery for Grid-Scale Energy Storage, *J. Electrochem. Soc.* 159 (2012) A1806–A1815.
- [31] M.L. Perry, R.M. Darling, R. Zaffou, High Power Density Redox Flow Battery Cells, *ECS Trans.* 53 (2013) 7–16.
- [32] K. Kordesch, V. Hacker, J. Gsellmann, M. Cifrain, G. Faleschini, P. Enzinger, et al., Alkaline fuel cells applications, *J. Power Sources.* 86 (2000) 162–165.
- [33] M.L. Perry, T.F. Fuller, A Historical Perspective of Fuel Cell Technology in the 20th Century, *J. Electrochem. Soc.* 149 (2002) S59.
- [34] S.M.H. Hashemi, M.A. Modestino, D. Psaltis, A membrane-less electrolyzer for hydrogen production across the pH scale., *Energy Environ. Sci.* 8 (2015) 2003–2009.
- [35] J.W. Campos, M. Beidaghi, K.B. Hatzell, C.R. Dennison, B. Musci, V. Presser, et

- al., Investigation of carbon materials for use as a flowable electrode in electrochemical flow capacitors, *Electrochim. Acta*. 98 (2013) 123–130.
- [36] C.R. Dennison, M. Beidaghi, K.B. Hatzell, J.W. Campos, Y. Gogotsi, E.C. Kumbur, Effects of flow cell design on charge percolation and storage in the carbon slurry electrodes of electrochemical flow capacitors, *J. Power Sources*. 247 (2014) 489–496.
- [37] N.C. Hoyt, R.F. Savinell, J.S. Wainright, Modeling of flowable slurry electrodes with combined faradaic and nonfaradaic currents, *Chem. Eng. Sci.* 144 (2016) 288–297.
- [38] K.B. Hatzell, M. Beidaghi, J.W. Campos, C.R. Dennison, E.C. Kumbur, Y. Gogotsi, A high performance pseudocapacitive suspension electrode for the electrochemical flow capacitor, *Electrochim. Acta*. 111 (2013) 888–897.
- [39] V. Presser, C.R. Dennison, J. Campos, K.W. Knehr, E.C. Kumbur, Y. Gogotsi, The electrochemical flow capacitor: A new concept for rapid energy storage and recovery, *Adv. Energy Mater.* 2 (2012) 895–902.
- [40] T.J. Petek, N.C. Hoyt, R.F. Savinell, J.S. Wainright, Slurry electrodes for iron plating in an all-iron flow battery, *J. Power Sources*. 294 (2015) 620–626.
- [41] P. Han, Y. Yue, Z. Liu, W. Xu, L. Zhang, H. Xu, et al., Graphene oxide nanosheets/multi-walled carbon nanotubes hybrid as an excellent electrocatalytic material towards $\text{VO}_2^+/\text{VO}_2^{2+}$ redox couples for vanadium redox flow batteries, *Energy Environ. Sci.* 4 (2011) 4710.
- [42] G. Wei, C. Jia, J. Liu, C. Yan, Carbon felt supported carbon nanotubes catalysts composite electrode for vanadium redox flow battery application, *J. Power Sources*. 220 (2012) 185–192.
- [43] S. Wang, X. Zhao, T. Cochell, A. Manthiram, Nitrogen-doped carbon nanotube/graphite felt as advanced electrode materials for vanadium redox flow batteries, *J. Phys. Chem. Lett.* 3 (2012) 2164–2167.

Electronic supplementary information

Maximizing the power density of aqueous electrochemical flow cells

Marc-Antoni Goulet, Omar A. Ibrahim, Will H. J. Kim & Erik Kjeang*

School of Mechatronic Systems Engineering, Simon Fraser University, 250-13450 102 Avenue,

Surrey, BC, V3T 0A3, Canada

S1 Ohmic resistance analysis

The ionic conductivity of the $\text{VO}^{2+}/\text{VO}_2^+$ electrolyte at 50% SOC is determined by varying the distance between 1 mm wide Toray carbon paper electrodes in a customized cell with 170 μm channel height filled with electrolyte and measuring the high frequency impedance corresponding to the total ohmic resistance. In this configuration, the ionic conductivity can be extracted from the slope of the graph in Fig. S1-1.

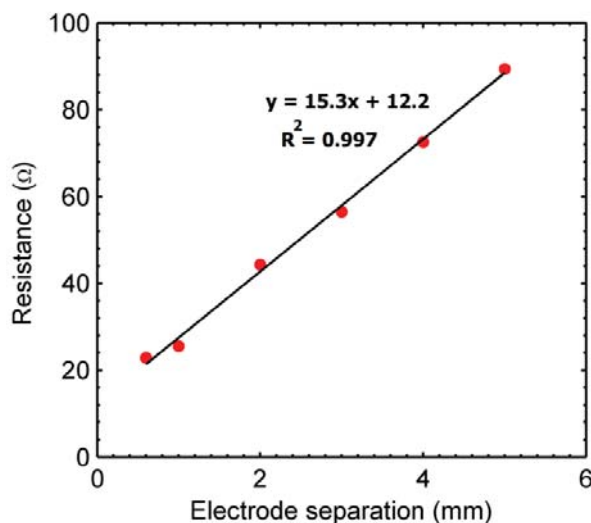


Fig. S1-1 Ohmic resistance as a function of distance between electrodes.

The same electrolyte is then injected into a baseline flow cell in order to deduce the combined contribution of the electrode and contact resistances, totalling roughly 9 Ω . Using the known in-plane conductivity of the carbon paper ($11\,000\text{ Sm}^{-1}$),¹ a contact resistance of roughly 2-3 Ω can be determined which is considerably less than previously assumed.² With the value of the electronic resistance known, the same cell is filled with other electrolytes to back-calculate their ionic conductivities. The data in Table S1-1 details the total ohmic resistance of the baseline cell filled with different electrolytes and their deduced corresponding conductivities.

Table S1-1 Electrolyte conductivity and total ohmic resistance of the baseline cell.

Electrolyte	Cell resistance (Ω)	Electrolyte conductivity (Sm^{-1})
50% $\text{VO}^{2+}/\text{VO}_2^+$	26.5	38
90% $\text{VO}^{2+}/\text{VO}_2^+$	22.5	49
50% $\text{V}^{2+}/\text{V}^{3+}$	32.6	28
90% $\text{V}^{2+}/\text{V}^{3+}$	32.6	28
4M H_2SO_4	20.3	59

As expected from the electrochemical reduction reactions in Eq. 1-3, the conductivity of the $\text{V}^{2+}/\text{V}^{3+}$ electrolyte is lower than that of the $\text{VO}^{2+}/\text{VO}_2^+$ electrolyte in general due to the consumption of hydrogen ions during the reduction of VO^{2+} and VO_2^+ . Reduction of V^{3+} to V^{2+} has no effect on hydrogen ion concentration.



The conductivity of a ‘blank’ 4 M H_2SO_4 electrolyte is also measured to provide an ideal design limit. At 59 Sm^{-1} , the conductivity of the 4 M H_2SO_4 agrees well with literature^{3,4} and is nearly 6x higher than the commercial target for ionomer fuel cell membranes.⁵ By reducing the concentration of vanadium ions, less hydrogen ions would be consumed during reduction reactions, thereby reducing the loss of electrolyte conductivity at different states of charge, with the end goal of moving all values toward the conductivity of the 90% $\text{VO}^{2+}/\text{VO}_2^+$ electrolyte seen in Table S1. This strategy is implemented in the final design of the next generation cell to minimize the channel resistance as much as possible.

S2 Parametric study

In an effort to optimize the baseline co-laminar flow cell design used for vanadium redox conversion a parametric study is conducted to quantify the effects of feature dimensions. From the above analysis on cell resistance it is clear that reducing the channel width would have an appreciable effect on the overall cell resistance and performance. Similarly, increasing the width or decreasing the length (changing the aspect ratio) of the flow-through porous electrodes has been shown by Thorson et al. to improve the cross-sectional power density of co-laminar cells.⁶ These approaches are investigated experimentally to assess their effect on the different metrics of power density.

The baseline cell design features 1 mm wide and 10 mm long electrodes separated by 1 mm wide centre channel as in the original studies.^{7,8} To study the effect of electrode length a cell featuring 15 mm long electrodes is tested. Similarly, a cell with 2 mm wide electrodes is also tested to study the effect of electrode width. Lastly, a cell featuring a ‘thin channel’ is also tested wherein the baseline channel width is reduced in half (0.5 mm). The data in Fig. S2-1 presents the polarization behaviour for the four different cell designs based on the volumetric current density normalized by the combined volume of both electrodes and the center channel.

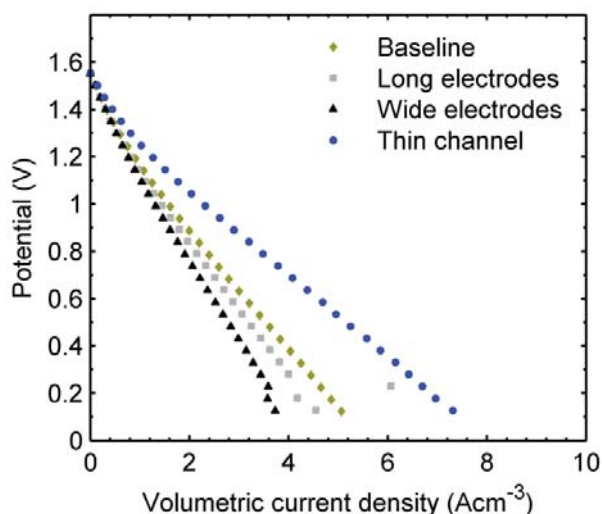


Fig. S2-1 Experimentally measured polarization of different cell architectures operated with 90% SOC vanadium redox reactants at $100 \mu\text{L} \cdot \text{min}^{-1}$.

As shown in Table S2-1, when the above polarization data is converted to power output, it becomes clear that the only strategy which improves the overall cell performance in all cases is a reduction in channel width. This is because a thinner channel helps reduce both the ionic resistance and total cell footprint simultaneously, while larger electrodes reduce the total resistance at the cost of an increased device footprint. It can therefore be deduced from these trends that shorter electrodes would result in increased power densities at the cost of lower absolute power output, as previously observed.⁹ This is not considered a practical strategy due to the already low power output of single cells. The overall goal for this study is to increase all power densities in addition to the absolute power output of the device.

Table S2-1 Experimentally measured cell performance.

	Power (mW)	Projected power density (Wcm ⁻²)	Cross-sectional power density (Wcm ⁻²)	Volumetric power density (Wcm ⁻³)
Baseline	8.31	0.083	0.573	1.91
Long electrodes	11.3	0.075	0.519	1.73
Wide electrodes	11.0	0.055	0.761	1.52
Thin channel	10.2	0.102	0.704	2.82

The above experimental data is meant to guide next generation cell design and to provide validation for a computational model for further optimization. The model for these cells is largely based on the previous work by Krishnamurthy et al.² which simulated the original microfluidic fuel cell with flow-through porous electrodes developed by Kjeang et al.⁷ The present work preserves the core physics of the model but adds the following constraints and refinements:

- 1) In addition to the model by Krishnamurthy et al., many models in the vanadium redox battery literature assumed elevated proton concentrations as high as 8 M which does not correspond to the true degree of dissociation of 4 M sulfuric acid. Also, many of these studies^{2,10,11} used a proton diffusivity as high as $9.3 \times 10^{-9} \text{ m}^2\text{s}^{-1}$ even though large concentrations of dissolved solutes have been shown to considerably reduce the diffusivity or mobility of hydrogen ions in aqueous solutions.^{12,13} Both of these issues lead to an excessively high ionic conductivity for the centre channel which exceeds the measured conductivities displayed in section S1. Instead of assuming the hydrogen ion concentration and diffusivity of hydrogen, these are constrained within each electrolyte stream in the current model to produce the experimentally determined ionic conductivities in Table S1-1.
- 2) The polarization data is IR-corrected with an additional 3Ω to account for the contact resistance described in section S1.
- 3) The model by Krishnamurthy et al. is updated with new kinetic parameter values for vanadium redox reactions on carbon paper. These values were more directly measured with a novel analytical technique for flow-through porous electrodes developed by our group.^{14,15} In the case of the $\text{VO}^{2+}/\text{VO}_2^+$ redox couple, a lower estimate for the heterogeneous rate constant based on these previous experiments is used, and found to fit the data more accurately. More specifically, the current model uses the following kinetic parameters:
 - Specific area of carbon paper: $a = 1.8 \times 10^6 \text{ m}^{-1}$
 - $\text{VO}^{2+}/\text{VO}_2^+$ heterogeneous rate constant: $k_{pos} = 1 \times 10^{-7} \text{ ms}^{-1}$
 - $\text{VO}^{2+}/\text{VO}_2^+$ charge transfer coefficient: $\alpha_{pos} = 0.15$
 - $\text{V}^{2+}/\text{V}^{3+}$ heterogeneous rate constant: $k_{neg} = 5 \times 10^{-9} \text{ ms}^{-1}$
 - $\text{V}^{2+}/\text{V}^{3+}$ charge transfer coefficient: $\alpha_{neg} = 0.5$

Beyond these three modifications, all other parameters and boundary conditions remain the same. For more details on these the reader is referred to that study.² Using this modified model, the polarization behaviour of the four parametric study cells is simulated using the COMSOL Multiphysics software (COMSOL 4.4) with results shown in Fig. S2-2 whereas the deduced power density is summarized in Table S2-2.

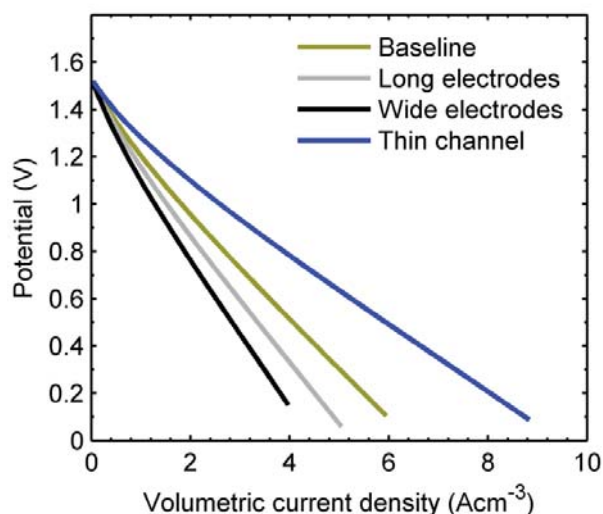


Fig. S2-2 Simulated polarization of different cell architectures operated with 90% SOC vanadium redox reactants at $100 \mu\text{L} \cdot \text{min}^{-1}$.

Table S2-2 Computationally simulated cell performance.

	Power (mW)	Projected power density (Wcm^{-2})	Cross-sectional power density (Wcm^{-2})	Volumetric power density (Wcm^{-3})
Baseline	9.50	0.095	0.655	2.18
Long electrodes	11.9	0.079	0.545	1.82
Wide electrodes	11.1	0.056	0.768	1.54
Thin channel	11.5	0.115	0.794	3.17

Overall, the model predicts the cell power densities to within 15% of the experimental values in all cases, where the largest discrepancies are due to the model overestimating the performance. This could be explained by fabrication inconsistencies in the cells, where it is common for residual space to remain around the electrode boundaries leading to partial flow bypass. In addition, it is also possible that the dimensions of the manually cut specific cell electrodes may differ slightly from their exactly modeled counterparts. In general, the relatively good agreement between the simulated and measured results validates the capacity of the model to simulate design changes on cell performance.

S3 Next generation cell design

By combining the lessons learned from the above characterization and parametric study, the cell architecture can be optimized to achieve a maximum power density. With the help of the following strategies the ohmic resistance of the cell is reduced from $30\ \Omega$ to approximately $8\ \Omega$ while the volume is reduced by half as explained in the primary article:

- 1) Center channel width reduced from 1.0 to 0.5 mm.
- 2) Reduction of vanadium concentration from 1.7 to 1.0 M to increase electrolyte conductivity.
- 3) Use of current collectors.
- 4) Reduction of electrode width from 1.0 to 0.5 mm.

With the same electrode material, the mass transfer and kinetic parameters of the cell should remain unchanged. By implementing the changes above in the computational model, the performance of the next generation cell is simulated. Accordingly, the next generation design is expected to achieve a power output of 13.4 mW. When the smaller device footprint is taken into account, this equates to a maximum volumetric power density of $5.98\ \text{Wcm}^{-3}$ as shown in Fig. S3-1.

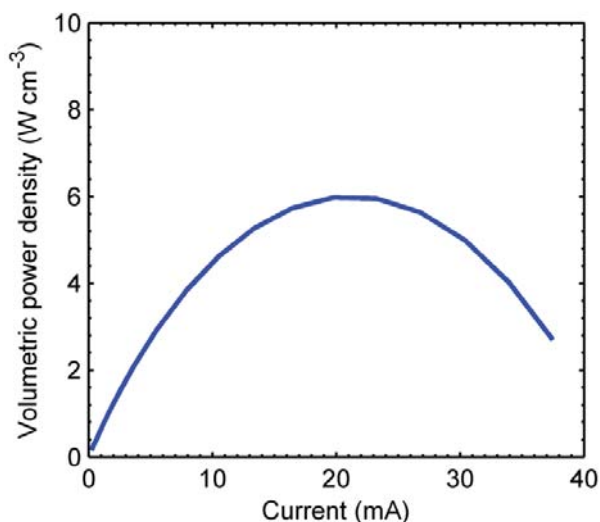


Fig. S3-1 Predicted volumetric power density of next generation cell operating on 90% SOC 1.0 M vanadium redox reactants at $200\ \mu\text{L}\cdot\text{min}^{-1}$.

The predicted power density of the next generation cell is in good agreement with the measured $5.88\ \text{Wcm}^{-3}$ found in Table 1 of the main article, which demonstrates a threefold increase in volumetric power density over the baseline design. Using this optimized cell as a starting point, it is expected that dynamic flowing deposition of carbon nanotubes will considerably improve the total power output by offsetting the poor kinetics produced by the lower concentration and smaller electrode dimensions.

References

- 1 D. Schmal, J. Van Erkel and P. J. Van Duin, *J. Appl. Electrochem.*, 1986, **16**, 422–430.
- 2 D. Krishnamurthy, E. O. Johansson, J. W. Lee and E. Kjeang, *J. Power Sources*, 2011, **196**, 10019–10031.
- 3 S. Corcuera and M. Skyllas-Kazacos, *Eur. Chem. Bull.*, 2012, **1**, 511–519.
- 4 F. Rahman and M. Skyllas-Kazacos, *J. Power Sources*, 2009, **189**, 1212–1219.
- 5 C. Houchins, G. Kleen, J. Spendelow, J. Kopasz, D. Peterson, N. Garland, D. Ho, J. Marcinkoski, K. Martin, R. Tyler and D. Papageorgopoulos, *Membranes (Basel)*, 2012, **2**, 855–878.
- 6 M. R. Thorson, F. R. Brushett, C. J. Timberg and P. J. A. Kenis, *J. Power Sources*, 2012, **218**, 28–33.
- 7 E. Kjeang, R. Michel, D. A. Harrington, N. Djilali and D. Sinton, *J. Am. Chem. Soc.*, 2008, **130**, 4000–4006.
- 8 M.-A. Goulet and E. Kjeang, *Electrochim. Acta*, 2014, **140**, 217–224.
- 9 O. A. Ibrahim, M.-A. Goulet and E. Kjeang, *Electrochim. Acta*, 2015, **187**, 277–285.
- 10 D. You, H. Zhang and J. Chen, *Electrochim. Acta*, 2009, **54**, 6827–6836.
- 11 Y. A. Gandomi, D. S. Aaron, T. A. Zawodzinski and M. M. Mench, *J. Electrochem. Soc.*, 2016, **163**, A5188–A5201.
- 12 M. Bonn, H. J. Bakker, G. Rago, F. Pouzy, J. R. Siekierzycka, A. M. Brouwer and D. Bonn, *J. Am. Chem. Soc.*, 2009, **131**, 17070–17071.
- 13 M. L. Soudijn, 2012, 85.
- 14 M.-A. Goulet, M. Eikerling and E. Kjeang, *Electrochem. commun.*, 2015, **57**, 14–17.
- 15 M.-A. Goulet, M. Skyllas-Kazacos and E. Kjeang, *Carbon N. Y.*, 2016, **101**, 390–398.